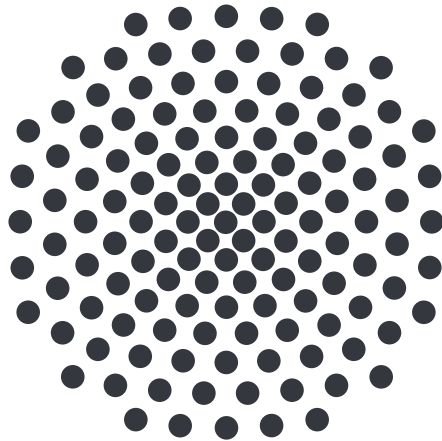


Microwave investigations on SrTiO₃-based materials at mK temperatures

Wissenschaftliche Arbeit zum Erlangen des akademischen
Grades Master of Science in Physik verfasst von

Mario Zinßer



University of Stuttgart
1. Physikalisches Institut

Hauptberichter: **Prof. Dr. Martin Dressel**

Mitberichter: **Prof. Dr. Peter Michler**

Betreuer: **Dr. Marc Scheffler, Markus Thiemann**

28. September 2018

Contents

Selbstständigkeitserklärung	5
List of Abbreviations	6
List of Figures	7
List of Tables	9
Deutsche Kurzfassung	10
1 Introduction and Motivation	12
2 Theoretical Basics	14
2.1 Basic Theory of Light and Matter	14
2.2 Crystallographic orientations and Miller indices	16
2.3 Electrons in Solids	17
2.3.1 Electronic Band structure	17
2.3.2 Effective Electron Mass	19
2.3.3 Charge Transport in the Drude Model	20
2.4 Electrons in Magnetic Field	21
2.4.1 Landau Levels	21
2.4.2 Cyclotron Resonance	23
2.5 Nb doped STO	30
2.5.1 Nb doped STO as a Material	30
2.5.2 Nb doped STO Samples	33
3 Experimental Basics	34
3.1 Setups	34
3.1.1 Bath Cryostat	34
3.1.2 Dilution Refrigerator	36
3.1.3 DC setup	36
3.2 Microwave Waveguides	36
3.3 Fitting Process	39
3.4 Cavity Perturbation Theory	40
3.5 Lists of used samples and equipment	42
3.5.1 Samples	42
3.5.2 Commercially bought Control Units	43
3.5.3 Microwave Waveguides	43
4 Experiments and Analysis	45
4.1 Preparation Experiments	45
4.1.1 Nb doped STO	46
4.1.2 Copper	47
4.2 Broadband Cyclotron Resonance Experiments	51

4.2.1	Copper, Nb doped STO and UPd_2Al_3	51
4.2.2	Parasitic Dips	54
4.3	Resonant Cyclotron Resonance Experiments	56
4.3.1	Copper	56
4.3.2	Parasitic Dips	57
4.3.3	Nb doped STO	59
4.4	Experiments on Superconducting Nb-STO	63
4.4.1	Process of Measuring	63
4.4.2	Complex Conductivity and Interpretation of Kinks	64
4.4.3	Temperature-dependent Critical Fields and Effective Electron Masses	70
4.4.4	Comparison of Length Scales	72
4.4.5	Superfluid Density and Homes' Law	73
4.4.6	Dispersion Relation	75
4.4.7	Summary and Conclusions	76
5	Summary and Outlook	78
A	Operation Manual for VTI	80
A.1	Sample mounting and cooling	80
A.2	Warming and sample removing	81
	References	82
	Acknowledgements	90

Selbstständigkeitserklärung

Hiermit versichere ich, dass die vorliegende Masterarbeit komplett selbstständig und nur unter Verwendung der angegebenen Literatur angefertigt wurde.

Direkt oder indirekt übernommene externe Zitate anderer Quellen wurden als solche kenntlich gemacht. Diese Arbeit wurde nicht in gleicher oder ähnlicher Weise bereits veröffentlicht.

Der Inhalt und exakte Wortlaut des gedruckten Exemplares stimmt mit dem des elektronischen überein.

Ort, Datum

Unterschrift Mario Zinßer

List of Abbreviations

2DEG	two dimensional electron gas
ARPES	angle-resolved photoemission spectroscopy
BCS theory	Bardeen-Cooper-Schrieffer theory
GPIB	General Purpose Interface Bus / IEC-625-Bus
Cu	copper
EPR	electron paramagnetic resonance
FWHM	full width at half maximum
LAO	lanthanum aluminate
Nb	niobium
Nb-STO	niobium doped strontium titanate
PES	photoemission spectroscopy
RRR	residual resistance ratio
Pb	lead
STO	strontium titanate
VNA	Vector Network Analyzer
VTI	Variable Temperature Inset

List of Figures

Figure 2.1	Miller indices	16
Figure 2.2	Bandstructure of copper	18
Figure 2.3	Brillouin zone and Fermi surface of copper	19
Figure 2.4	Landau cylinders	21
Figure 2.5	Landau levels	22
Figure 2.6	Cyclotron resonance setup	24
Figure 2.7	Cyclotron orbits of copper	25
Figure 2.8	Azbel'-Kaner cyclotron resonance	27
Figure 2.9	Cyclotron resonance absorption peak of a non-conducting sample	29
Figure 2.10	Atomic schematic and dispersion relation of STO	31
Figure 2.11	Effective masses and the two superconducting domes in Nb-STO	32
Figure 2.12	Field-dependent kinks in thermal conductivity	33
Figure 3.1	Schematic of bath cryostat	35
Figure 3.2	Coplanar and stripline waveguides	36
Figure 3.3	Electric and magnetic fields of coplanar and stripline waveguides	37
Figure 3.4	Microwave waveguide inside the microwave box	38
Figure 3.5	First three modes in a resonator	39
Figure 3.6	Fitting procedure	40
Figure 4.1	DC resistivity and scattering rate of Rdc-NbSTO 0.05%	46
Figure 4.2	Comparison of DC resistivity	47
Figure 4.3	DC resistivity and scattering rate of all Cu strips	48
Figure 4.4	Microscopic pictures of raw and annealed Cu	49
Figure 4.5	Laue diffractions and orientation of the Cu sample	51
Figure 4.6	Broadband cyclotron resonance measurements on Nb-STO	52
Figure 4.7	Broadband cyclotron resonance measurements on copper	53
Figure 4.8	Broadband cyclotron resonance measurements on UPd ₂ Al ₃	53
Figure 4.9	Broadband transmission coefficients without samples	54
Figure 4.10	Resonant cyclotron resonance measurements on copper	57
Figure 4.11	EPR investigation on empty coplanar YBCO resonator	58
Figure 4.12	Sample and positioner	59
Figure 4.13	Mode suppressing due to decreasing distance between sample and waveguide	60
Figure 4.14	Resonant cyclotron resonance measurements on Nb-STO 0.05%	61
Figure 4.15	Temperature dependent measurement of resonance frequency and bandwidth	64
Figure 4.16	Kinks within the field dependent bandwidth	65
Figure 4.17	Field-dependent imaginary part of the optical conductivity	66
Figure 4.18	Field-dependent real part of the optical conductivity	67
Figure 4.19	Fits for field-dependent imaginary part of the optical conductivity	68
Figure 4.20	Frequency-dependent filling of both bands at 70mK	68
Figure 4.21	Coherence lengths and Abrikosov structure of Nb-STO	69
Figure 4.22	Critical fields and effective mass ratio as a function of temperature	71
Figure 4.23	Comparison of different length scales	72
Figure 4.24	Superfluid density as a function of magnetic field and temperature	74
Figure 4.25	Homes' Law for several superconductors including Nb-STO	75

Figure 4.26	Disperion relation for two bands	76
-------------	--	----

List of Tables

Table 2.1	Nb-STO samples	33
Table 3.1	Used samples	42
Table 3.2	Used control units	43
Table 3.3	Used chips	44
Table 4.1	Summary of quantites for Nb-STO 0.35%	77

Deutsche Kurzfassung

Strontiumtitanat (STO) ist ein Halbleiter, der unter einer bestimmten n -Dotierung bei Milli Kelvin-Temperaturen (mK) einen Phasenübergang in den supraleitenden Zustand aufweist. Es war damit einer der ersten "*supraleitenden Halbleiter*" und zugleich der erste *Oxid-Supraleiter*, der unter anderem die mit dem Nobel-Preis 1987 ausgezeichnete Entdeckung von *Hochtemperatur-Supraleitern* vorantrieb. Darüber hinaus wurde zum ersten Mal ein sogenanntes *dome*-förmiges Verhalten als Funktion der Dotierung festgestellt, welches durch eine Reduktion an Sauerstoffatomen oder eine Ersetzung von Titanatomen durch Niobatome (Nb-STO) erzielt wird. Die hierfür benötigten *Ladungsträgerdichten* und die damit verbundenen Energieskalen sind verhältnismäßig klein und schränken damit die Anzahl an möglichen Kopplungsmechanismen der *Cooperpaare* erheblich ein. Dies ist nicht in Einklang mit der *BCS-Theorie* zu bringen und bis zum heutigen Tag nicht vollständig verstanden, weshalb STO ein aktuelles Forschungsthema darstellt.

An der Grenzschicht zu *Lanthan Aluminiumoxid* (LAO) weist STO ein *zweidimensionales Elektronengas* extrem mobiler, freier Ladungsträger auf, das ebenfalls einen supraleitenden Übergang bei mK-Temperaturen zeigt. Wie auch in STO selbst ist die Supraleitung dort *dome*-förmig und entstammt mehreren *elektronischen Bändern*. Diese Arbeit soll unter anderem auch zum Verständnis der Supraleitung an der LAO-STO-Grenzschicht beitragen.

Hierfür sollen die *elektronischen Bandeigenschaften* und mit besonderem Schwerpunkt die *effektiven Massen* der bei mK-Temperaturen zur Supraleitung beitragenden Elektronen untersucht werden. Zur direkten Messung dieser bietet sich die Methode der *Zyklotronresonanz* an, bei der durch ein extern angelegtes Magnetfeld Leitungselektronen in definierte *Landau-Niveaus* gequantelt werden und deren Übergang mit entsprechenden Energien im μeV -Bereich angeregt wird. Eine der Hauptherausforderungen dieser Messmethode liegt in der Notwendigkeit einer höheren Messfrequenz als die Streurate, was nur für sehr reine Metalle im genannten Energiebereich erreicht werden kann. Die hierzu nötige *Mikrowellenstrahlung* wird mittels *koplanarer* und *streifenleitenden Wellenleitern* übertragen und deren Transmissionssignal analysiert.

Um ein entsprechendes, der Zyklotronresonanz zuzuschreibendes Messsignal vorzufinden, wurden mehrere Experimente durchgeführt. Eines von diesen beinhaltet Anzeichen eines Zyklotron-Messsignals. Obwohl dieses Ergebnis nicht reproduziert werden konnte und damit dessen Verlässlichkeit in Frage zu stellen ist, gingen Messwerte aus dieser hervor, die effektive Massen zwischen 3 und 4 Elektronenmassen und Streuraten zwischen 9 und 10 GHz ergaben, was mit publizierter Literatur in Einklang steht.

Außerdem wurden Messungen der komplexen, optischen Leitfähigkeit innerhalb des supraleitenden domes von Nb-STO durchgeführt. Mit diesen ist es möglich, zwei zur effektive Masse korrelierte *Kohärenzlängen* zu bestimmen und dadurch das Verhältnis beider Massen der zur Supraleitung beitragenden Elektronen zu bestimmen.

Darüber hinaus wurden diese Daten noch genutzt, um einige andere charakteristische Eigenschaften wie die *mittlere, freie Weglänge*, die *Fermigeschwindigkeit* von beiden supraleitenden Bändern und die *suprafluide Dichte* zu bestimmen. Letztere wurde zur Berechnung der *London'schen Eindringtiefe* und des *Ginzburg-Landau-Parameters* genutzt, die die Zugehörigkeit zur Klasse der Typ-II-Supraleiter von Nb-STO bestätigen. Des Weiteren legt der Vergleich der Kohärenzlänge mit der mittleren freien

Weglänge und die Einordnung von Nb-STO in das *Home'sche Gesetz* ein *dirty limit*-Verhalten für Supraleiter nahe. All diese Eigenschaften sind starke Anzeichen für ein *Mehrband-Supraleiter* mit lediglich einer Energielücke in Nb-STO.

Introduction and Motivation

Strontium titanate (STO) is an electrical semiconductor that undergoes a *superconducting transition* [Schooley *et al.*, 1964] for a certain amount of *n*-doping at a comparably low critical temperature, commonly given in the order of several hundreds of milli Kelvin (mK). In addition to be one of the first discovered "*superconducting semiconductors*", it was the earliest discovered *oxide superconductors* and eventually was the starting point for the discovery of *high temperature superconductors* [Bednorz and Müller, 1986], which was awarded with the Nobel prize in physics in 1987.

In fact, STO possesses a *superconducting dome* as a function of doping, which is achieved by either reducing oxygen (SrTiO_{3-x}) [Koonce *et al.*, 1967] or replacing titanium with niobium ($\text{SrTi}_{1-x}\text{Nb}_x\text{O}_3$) [Pfeiffer and Schooley, 1969]. This was the first discovery of such a dome-shaped critical temperature. [Schooley *et al.*, 1965] The mentioned dome exists at a remarkably low *charge carrier concentration* of conducting electrons, which is not in accordance with the common *virtual phonon coupling* in the *weak-coupling limit* within the *BCS theory* [Bardeen *et al.*, 1957]. Consequently, the comparable low energy scales in the *micro electron volt* (μeV) range restrict the variety of possible *Cooper pairing mechanisms* that could cause superconductivity in STO, and several unconventional scenarios have been proposed, such as *soft optical phonons* in the *tetragonal phase* [Appel, 1969], *plasmons* and *polar optic phonons* [Takada, 1980] or *long-range dipolar interactions* near to the *ferroelectric quantum critical point* [Rowley *et al.*, 2014]. *S-wave superconductivity* has been reported recently [Lin *et al.*, 2015b], but a final and exhaustive explanation for the dome-shaped behavior is still missing down to the present day, rendering STO a cutting-edge research topic.

Bringing pure STO in contact with *lanthanum aluminate* (LAO) reveals interesting features as well. Not only does a *two-dimensional electron gas* (2DEG) of rather high *charge carrier mobility* emerge [Ohtomo and Hwang, 2004], but it also becomes superconductive in the range of several hundred mK [Reyren *et al.*, 2007]. Just like doped STO itself, the LAO-STO interface has a superconducting dome as a function of charge carrier density, which can be varied by *electrostatic tuning* via a *gate voltage* [Caviglia *et al.*, 2008]. As recently published, multiple bands contribute to superconductivity in this interface, like in doped STO. [Singh *et al.*, 2018] This work might also contribute towards the understanding of superconductivity in the LAO-STO interface.

In earlier studies of bulk niobium-doped STO (Nb-STO), *multi-gap superconductivity* has been reported [Binnig *et al.*, 1980; Lin *et al.*, 2014b], whereas in recent *microwave measurements* only one

gap was observed [Thiemann *et al.*, 2018; Swartz *et al.*, 2018]. The clarification of this controversy will also be topic of this thesis.

Furthermore, the electronic structure of Nb-STO is of fundamental importance, which is why this thesis focuses on the determination of the *effective electron masses* of the electrons which contribute to superconductivity at mK-temperatures. Regarding this topic, *Shubnikov–de Haas oscillations* have previously been measured, yielding several masses as a function of doping for the three superconducting bands. [Lin *et al.*, 2014a] Within this work another measurement technique will be applied, viz. *cyclotron resonance*, where a magnetic field creates discrete energetic electron states, i.e. *Landau levels*, in which electrons are stimulated by optical excitations. Hence, a main goal of this thesis will be to check the feasibility of cyclotron resonance measurements on Nb-STO, since this measurement technique is usually only applied on simple metals and semiconductors, but recently also to unconventional materials, such as heavy fermions [Tonegawa *et al.*, 2012, 2013]. Besides Nb-STO, a copper single crystal will be subject of this thesis for test purposes of the measurement technique, as well.

Due to the characteristic energy scales of STO in the μeV range and relevant magnetic fields in the Tesla range, optical spectroscopy in the microwave regime will be used. Experimentally accessible ranges in this work are temperatures down to several tens of mK, magnetic fields up to 8 T and frequencies from 1 to 50 GHz. As a probing measurement device, in-house-prepared of *coplanar* and *stripline microwave waveguides* will be used, providing resonator *quality factors* up to several ten thousands [Ebensperger *et al.*, 2016].

This thesis is structured in four large sections besides this introduction. After the explanation of the fundamental theoretical basics in the first section, the subsequent section will deal with the experimental setups and measurement methods. The following main analysis part deals with the preparation and characterization of the samples, then continues with broadband and resonant cyclotron resonance attempts and ends with microwave conductivity measurements as well as their implications and interpretations. To conclude this thesis, a summary and an outlook will be given.

Theoretical Basics

This section deals with the fundamental theoretical principles, which are needed to understand this thesis. It starts with the derivation of several necessary physical sizes as the *skin depth* δ_{skin} and the *wave impedance* Z . Afterwards a short introduction in *Miller indices* and electron transport in metals is given, ending with the concept of *effective mass*. Subsequently the main theory part about electrons in the magnetic field including *cyclotron resonance* follows. In the end, the material of interest *niobium doped strontium titanate* and the samples itself are discussed.

2.1 Basic Theory of Light and Matter

The general description of the interaction between light and matter is given by the *Maxwell equations* [Maxwell, 1861]. In a material the macroscopic equations in SI-units are given by

$$\nabla \vec{D} = \rho \quad (2.1a)$$

$$\nabla \vec{B} = 0 \quad (2.1b)$$

$$\nabla \times \vec{E} = -\frac{\partial \vec{B}}{\partial t} \quad (2.1c)$$

$$\nabla \times \vec{H} = \frac{\partial \vec{D}}{\partial t} + \vec{j}. \quad (2.1d)$$

Here \vec{E} , \vec{D} , \vec{H} and \vec{B} are the *electric field*, *electric displacement field*, *magnetic field* and *magnetic flux density*, respectively. Moreover ρ is the *charge density* and \vec{j} the *displacement current*.

In a material the charge carriers form a *polarization* \vec{P} and *magnetization* \vec{M} , which needs to be taken into account for the electric and magnetic fields.

$$\vec{D} = \varepsilon_0 \varepsilon_1 \vec{E} + \vec{P} \quad (2.2a)$$

$$\vec{H} = \frac{1}{\mu_0 \mu_1} \vec{B} - \vec{M} \quad (2.2b)$$

Here ε_0 and μ_0 are the *vacuum permittivity* and *vacuum permeability* and ε_1 and μ_1 are the real parts of the dimensionless *permittivity* and *permeability* functions.

However, the *current density* \vec{j} can be connected with the *electric conductivity* σ and the electric field via *Ohm's law* [Ohm, 1827].

$$\vec{j} = \sigma \vec{E} \quad (2.3)$$

To get the *dispersion relation*, we need to solve the Maxwell equations. Therefore we apply rotation on (2.1c) and (2.1d), where $\nabla \times \nabla \times \vec{A} = \nabla \cdot (\nabla \vec{A}) - \Delta \vec{A}$ and plug in (2.1a), (2.1b), (2.2a), (2.2b) and (2.3). Furthermore we use that $\nabla \vec{E}$ vanishes, since we are only interested in light having a much larger wavelength than the atomic distance, which blurs out the atoms as sources of the electrical field. This yields the wave differential equations for the electric and magnetic field.

$$\Delta \vec{E} = \mu_0 \mu_1 \varepsilon_0 \varepsilon_1 \ddot{\vec{E}} + \mu_0 \mu_1 \sigma \dot{\vec{E}} \quad (2.4a)$$

$$\Delta \vec{H} = \mu_0 \mu_1 \varepsilon_0 \varepsilon_1 \ddot{\vec{H}} + \mu_0 \mu_1 \sigma \dot{\vec{H}} \quad (2.4b)$$

With the ansatz

$$\vec{E} = \vec{E}_0 e^{iqx - i\omega t} \quad (2.5a)$$

$$\vec{B} = \vec{B}_0 e^{iqx - i\omega t + i\varphi} \quad (2.5b)$$

for the electric and magnetic field and the relation

$$c^2 = \frac{1}{\mu_0 \mu_1 \varepsilon_0 \varepsilon_1} \quad (2.6)$$

with the speed of light in matter c we finally get the dispersion relation for the *wave vector* q and the *oscillation frequency* ω .

$$q = \frac{\omega}{c} \sqrt{1 + i \frac{\sigma}{\varepsilon_0 \varepsilon_1 \omega}} \quad (2.7)$$

$$\stackrel{\omega \ll \omega_P}{\approx} (1 + i) \sqrt{\frac{\sigma \omega}{2 \varepsilon_0 \varepsilon_1 c^2}}$$

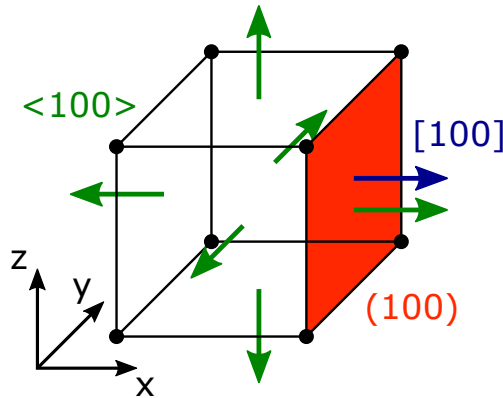
The last step is only possible if $\frac{\sigma}{\varepsilon_0 \varepsilon_1 \omega} \gg 1$, which is the case for frequencies much smaller than the *plasma frequency* ω_P for metals. After replacing this *wave vector* back in the ansatz, we obtain the time- and location-dependent fields.

$$\vec{E} = \vec{E}_0 e^{-\sqrt{\frac{\sigma \omega}{2 \varepsilon_0 \varepsilon_1 c^2}} x} e^{i \left(\sqrt{\frac{\sigma \omega}{2 \varepsilon_0 \varepsilon_1 c^2}} x - \omega t \right)} \quad (2.8a)$$

$$\vec{B} = \vec{B}_0 e^{-\sqrt{\frac{\sigma \omega}{2 \varepsilon_0 \varepsilon_1 c^2}} x} e^{i \left(\sqrt{\frac{\sigma \omega}{2 \varepsilon_0 \varepsilon_1 c^2}} x - \omega t + \varphi \right)} \quad (2.8b)$$

The first exponential term is a decaying function, giving the wave only a certain length to penetrate into the material. This length is called the *skin depth* δ_{skin} .

$$\delta_{\text{skin}} = \sqrt{\frac{2 \varepsilon_0 \varepsilon_1 c^2}{\sigma \omega}} \stackrel{(2.6)}{=} \sqrt{\frac{2}{\mu_0 \mu_1 \sigma \omega}} \quad (2.9)$$



■ Figure 2.1: Miller indices for planes and directions.

Another important dimension is the complex *wave impedance* Z , which is given by the ratio of the electric and magnetic field.

$$Z := \frac{|\vec{E}|}{|\vec{B}|} \stackrel{(2.1c),(2.5a),(2.5b),(2.6),(2.7)}{=} \sqrt{\frac{\mu_0 \mu_1 \omega}{\varepsilon_0 \varepsilon_1 \omega + i\sigma}} \quad (2.10)$$

For non-conducting materials, such as good insulators, Z yields

$$Z = \sqrt{\frac{\mu_0 \mu_1}{\varepsilon_0 \varepsilon_1}}, \quad (2.11)$$

whereas in vacuum it is given via

$$Z \stackrel{\mu_1=\varepsilon_1=1}{=} \sqrt{\frac{\mu_0}{\varepsilon_0}} \approx 377 \Omega. \quad (2.12)$$

For good conducting materials Z yields

$$Z = (1 - i) \sqrt{\frac{\omega \mu_0 \mu_1}{2\sigma}}. \quad (2.13)$$

The concept of wave impedance can also be transferred to the *surface impedance* Z_S . [Dressel and Grüner, 2002]

2.2 Crystallographic orientations and Miller indices

One way to describe the inner lattice orientations of a crystal are the *Miller indices* named after their inventor William Hallowes Miller. [Miller, 1839] In the following the three most used notations are explained.

Directions - square brackets

A direction is simply given by a vector with all vector entries written next to each other in square brackets. For example the [100] direction is along the vector $\begin{pmatrix} 1 \\ 0 \\ 0 \end{pmatrix}$, as the blue arrow in [Figure 2.1](#) shows.

Negative numbers are notated by a bar over the integer instead of a minus in front, such as $[\bar{1}00]$.

Bundle of equivalent directions - angle brackets

Since a crystal always has a certain symmetry some directions are completely equivalent to each other. They are all bundled under the angle brackets notation. In a face centered cubic crystal for instance to the $\langle 100 \rangle$ belong all vectors along the cube edge: [100], $[\bar{1}00]$, [010], $[0\bar{1}0]$, [001] and $[00\bar{1}]$, as shown in [Figure 2.1](#) by the green arrows.

Planes - round brackets

A plane, noted by the same numbers as a direction, is perpendicular to this direction meaning that the latter is its normal vector. This can be seen in [Figure 2.1](#) by the orange (100) plane.

2.3 Electrons in Solids

Since electrons in solids behave not exactly as a free electron gas, this section outlines the electronic properties of electron states in a crystal structure. First it is discussed how *energy bands* form and afterwards their impact on the transport properties.

2.3.1 Electronic Band structure

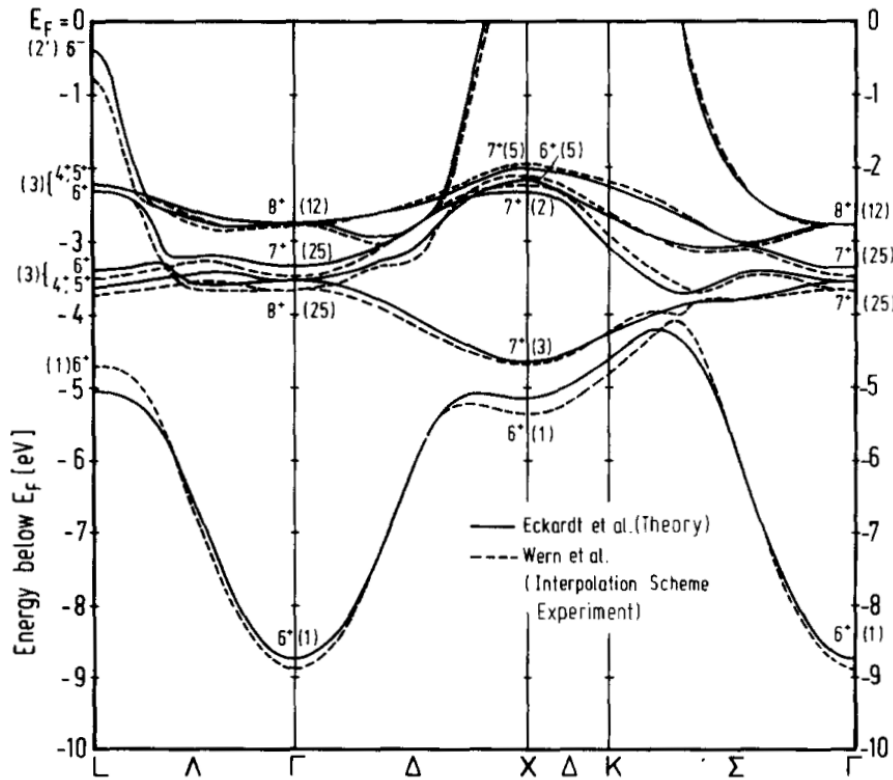
The *band structure* describes how electrons behave quantum mechanically in an infinitely large, perfect single crystal.

In a single atom, an electron has an exact defined discrete *atomic orbital* with a dedicated discrete energy. If, however, two atoms are brought next to each other, the atomic orbitals form a superposition due to electron-electron interaction. Hence, the *energy states* are split into two different *Eigenvalues* of the *Schrödinger equation*, one being higher, one being lower. For a macroscopic *single crystal*, a rather large amount of atoms are brought together. This creates an enormous amount of energy states, which can be considered as a continuous *energy spectrum* rather than several single states. This quasi stepless spectrum is called an *energy band*.

If the energy is now plotted over the wave vector $\vec{k} = \frac{\vec{p}}{\hbar}$, where \vec{p} is the *momentum* and \hbar the *reduced Planck constant*, rather than over the *spacial coordinate*, the energy band becomes an *electronic band structure* as illustrated in [Figure 2.2](#) for copper. Therefore, band structures are dispersion relations for electrons in solids. For a free electron gas it would be a parabolic dependence on \vec{k} according to the energy

$$E = \frac{\hbar^2 k^2}{2m^*} \quad (2.14)$$

with the effective mass m^* , which still can be seen at the Γ point ($\vec{k} = 0$). The periodicity of the crystal structure allows to show only the first *Brillouin zone*, which has the effect that for higher



■ Figure 2.2: Theoretical (solid) and measured (dashed) band structure of copper. [Courths and Hüfner, 1984]

energies the electronic bands become more dense in the first Brillouin zone. The wave vector on the x-axis here is changed on a path as it can be seen in the Brillouin schematic of a face-centered cubic crystal in Figure 2.3 a. Here the first Brillouin zone is marked in red and the arrows represent the crystal orientations. In Figure 2.3 b the Fermi surface of copper is drawn in a color plot, which is the surface of the highest occupied state in the k -space. Hence, all electrons on this surface have the same energy.

The most common methods to calculate electronic band structures are the *tight binding model* and the *$k \cdot p$ perturbation theory*.

To measure the density of states and hence the energy bands, one can use *photoemission spectroscopy* (PES). To also get the band structure plotted over the wave vector, *angle-resolved photoemission spectroscopy* (ARPES) can be used.

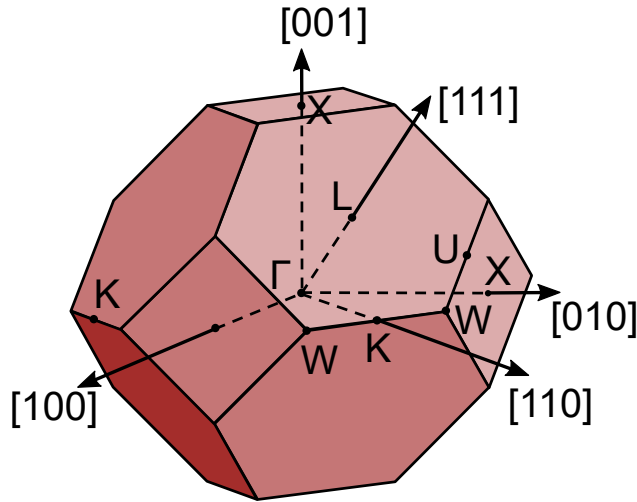


Figure 2.3a: First Brillouin zone of a face-centered cubic crystal with symmetry points and crystal orientations.

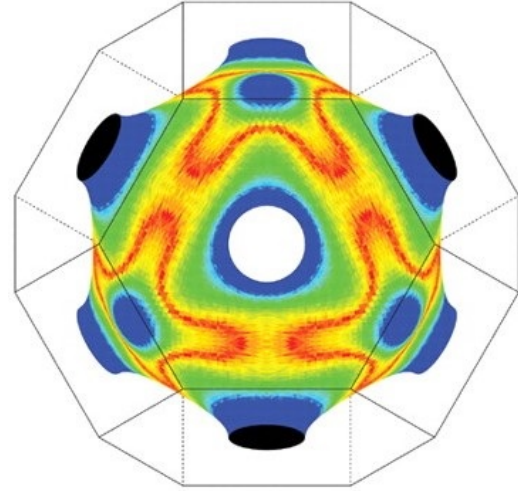


Figure 2.3b: Fermi surface of copper perpendicular to [111]. [Weismann *et al.*, 2009] The surrounding gray lines constitute the first Brillouin zone, while color indicates the Fermi velocity.

■ Figure 2.3: Brillouin zone and Fermi surface of copper.

2.3.2 Effective Electron Mass

The *effective mass* of an electron is a *semi classical concept* in solid state physics, as localized electrons in a solid can be considered as a *Bloch wave*. Electrons in a crystal are affected by the lattice itself, which can be understood as an additional term of inertia for the electron. In analogy to *Newton's second law* of mechanics [Newton, 1687] this inertia can effectively be understood as a modified mass of the electron, although the actual mass m does not change at all. It is then considered as the effective electron mass m^* .

For every *matter wave* the quasi force F_i is defined via the quasi momentum $p_i = \hbar k_i$ [Demtröder, 2005] as follows:

$$F_i = \dot{p}_i = \hbar \dot{k}_i = \hbar \frac{\partial k_i}{\partial t} \quad (2.15)$$

The moving electron as a Bloch wave can then be considered as a *wave packet* moving through the crystal with the *group velocity* $v_g(k)$. [Demtröder, 2005]

$$v_g(k) = \frac{\partial \omega}{\partial k_j} \quad (2.16)$$

$$\stackrel{E=\hbar\omega}{=} \frac{1}{\hbar} \frac{\partial E}{\partial k_j}$$

Here E is the energy of the electron in the corresponding electronic band structure
The derivative can then simply be received as

$$\begin{aligned}
 \dot{v}_g(k) &\stackrel{(2.16)}{=} \frac{\partial}{\partial t} \left(\frac{1}{\hbar} \frac{\partial E}{\partial k_j} \right) \\
 &= \frac{\partial k_i}{\partial t} \frac{\partial}{\partial k_i} \left(\frac{1}{\hbar} \frac{\partial E}{\partial k_j} \right) \\
 &\stackrel{(2.15)}{=} \frac{1}{\hbar^2} \underbrace{\frac{\partial^2 E}{\partial k_i \partial k_j}}_{\frac{1}{m^*_{ij}}} F_i.
 \end{aligned} \tag{2.17}$$

Since equation (2.17) is in perfect analogy to Newton's second law of classical mechanics the term $\hbar^2 \left(\frac{\partial^2 E}{\partial k_i \partial k_j} \right)^{-1}$ is called the *effective mass tensor* m^*_{ij} .

For an isotropic material the definition becomes a scalar and is equal in all directions.

$$m^* = \hbar^2 \left(\frac{\partial^2 E}{\partial k^2} \right)^{-1} \tag{2.18}$$

Therefore, the curvature of the energy bands within the band structure is enough to describe the undisturbed dynamics of the electron in a crystal structure of a solid.

The concept also holds for a free particle with the energy $E_{\text{free}} = \frac{\hbar^2 k^2}{2m_{\text{free}}}$ since the effective mass $m^*_{\text{free}} = \hbar^2 \left(\frac{\partial^2 E_{\text{free}}}{\partial k^2} \right)^{-1} = m_{\text{free}}$ then perfectly equals the usual mass m_{free} .

2.3.3 Charge Transport in the Drude Model

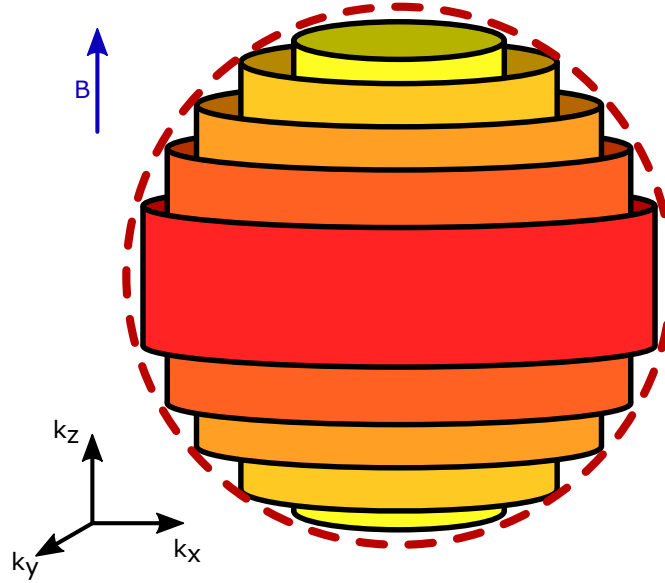
The transport characteristics of electrons in metals can be nicely described by the *Drude model*. [Drude, 1900] The equation of motion in this model is

$$m^* \cdot \dot{\vec{v}} = -e \left(\vec{E} + \vec{v} \times \vec{B} \right) - \frac{m^*}{\tau} \vec{v}_D, \tag{2.19}$$

where e is the *elementary charge*, $\tau = \frac{1}{\Gamma}$ the *mean free time* with the *scattering rate* Γ and v_D the *drift velocity* of the electrons. For a vanishing magnetic field and by using Ohm's law from (2.3) and the ansatz $\vec{v} \sim \vec{E} \sim e^{-i\omega t}$ the complex, frequency-dependent conductivity can be written as

$$\sigma(\omega) = \underbrace{\frac{ne^2\tau}{m^*}}_{\sigma_0} \frac{1}{1 - i\omega\tau}. \tag{2.20}$$

Here n is the *charge density* and σ_0 the *DC conductivity*.



■ **Figure 2.4: Landau cylinders in k-space.** In zero field all states are isotropic in all directions within the Fermi surface (red dashed), whereas with an increasing magnetic field the allowed states are only located on the colored cylinders meaning that they are free to propagate in k_z direction, but quantized on circles in the plane perpendicular to the external applied magnetic field B .

2.4 Electrons in Magnetic Field

In this section, the dynamics of electrons under an external applied magnetic field are theoretically outlined. Especially the *cyclotron resonance* as an experimental approach of investigating effective electron masses and *Fermi surfaces* is described in detail.

2.4.1 Landau Levels

For free electrons in zero field, the filled energy states are spread continuously under the *Fermi distribution* [Fermi, 1926]

$$f(E) = \frac{1}{e^{\frac{E}{k_B T}} + 1}, \quad (2.21)$$

where E is the energy of the electron, k_B the *Boltzmann constant* and T the temperature. In k-space this is a sphere around $\vec{k} = 0$, so called *Fermi sphere*.

That behavior changes drastically for a rising magnetic field. In the plane perpendicular to the external static applied magnetic field B the energy states are now quantized, whereas the field doesn't have any influences on the parallel propagation (here the z direction) of the electrons. [Landau, 1930] This results from the Schrödinger equation with the *Hamiltonian* $H = \frac{1}{2m^*} (\vec{p} - q\vec{A})^2$ with the momentum \vec{p} and the vector potential \vec{A} defined via

$$\vec{B} = \nabla \times \vec{A}. \quad (2.22)$$

The energy of a single electron is then given by

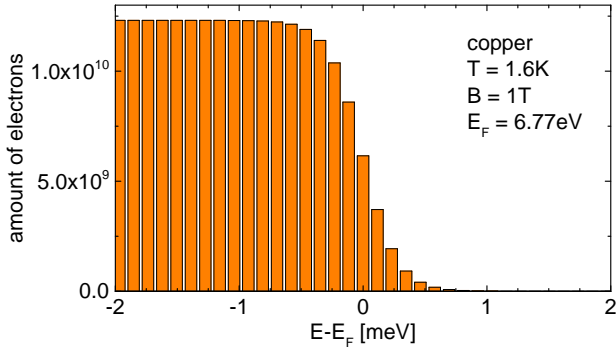


Figure 2.5 a: Landau levels of copper at $T = 1.6$ K for $B = 1$ T.

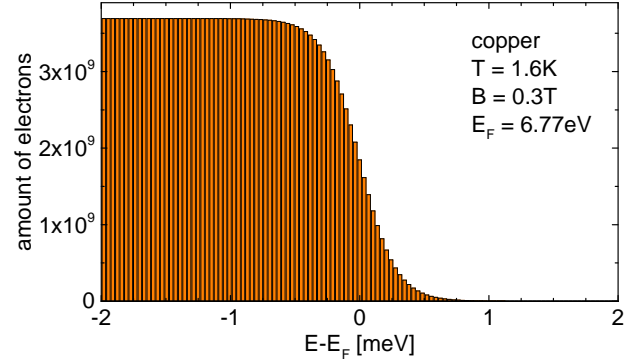


Figure 2.5 b: Landau levels of copper at $T = 1.6$ K for $B = 0.3$ T.

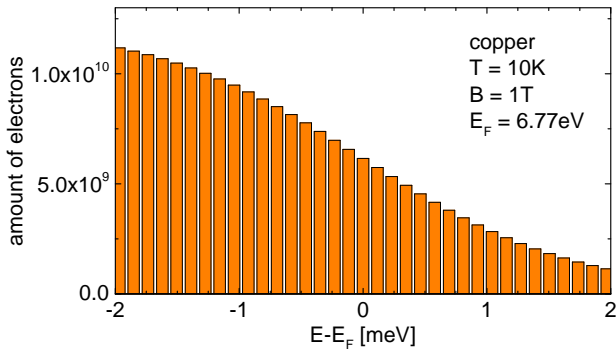


Figure 2.5 c: Landau levels of copper at $T = 10$ K for $B = 1$ T.

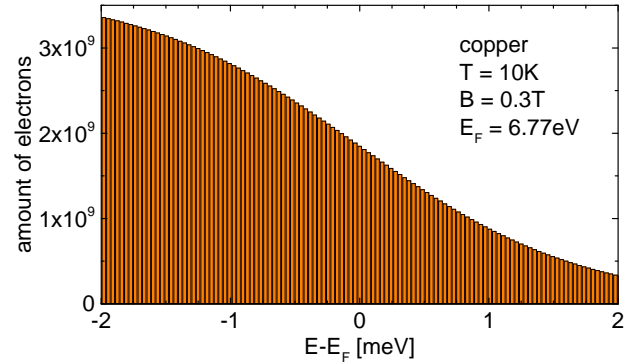


Figure 2.5 d: Landau levels of copper at $T = 10$ K for $B = 0.3$ T.

■ **Figure 2.5: Landau levels of copper for different applied magnetic fields at different temperatures.** The effective mass was simply assumed as $1m_e$, the charge carrier density as $8 \cdot 10^{22} \frac{1}{\text{cm}}$ and the affected volume of the sample as $1 \text{ cm} \times 15 \text{ nm} \times 60 \mu\text{m}$. In all cases the Fermi energy is 6.77 eV .

$$E(n, p_z) = \underbrace{\hbar \frac{eB}{m^*}}_{\omega_c} \left(n + \frac{1}{2} \right) + \frac{p_z^2}{2m^*}. \quad (2.23)$$

Here m^* is the effective mass of the electron in the solid, p_z its momentum in z direction and n is a the quantum number of the n -th *Landau level* and hence an integer value $\in \mathbb{N}$. The expression

$$\omega_c = \frac{eB}{m^*} \quad (2.24)$$

is called the *cyclotron frequency*^[2.1], as it will be explained in section 2.4.2. For a free electron gas this cyclotron frequency lies in the microwave regime for reasonable magnetic fields in the range of several Tesla.

In a three dimensional schematic in k -space the states are distributed on stacked cylinders called *Landau cylinders*, but still constricted within the Fermi surface, as it is drawn in red dashed in [Figure 2.4](#).

^[2.1]This formula only holds for non-relativistic electrons. For velocities near the speed of light the effective mass gets the prefactor $\gamma = \frac{1}{\sqrt{1 - \frac{v^2}{c^2}}}$ [Einstein, 1905], yielding to a resonance frequency of $\omega_c = \frac{eB}{\gamma m^*}$.

This process of going from a continuous distribution in the Fermi sphere to discrete Landau cylinders is called *condensation*.

From equation (2.23) one can see, that for an increasing magnetic field, the distance between two Landau levels gets larger. The same holds for the Landau cylinders. As a consequence, the single levels get more degenerated since more electrons condensate to a single Landau level.

The trajectory of dynamic electrons within a certain magnetic field describes a helix since the orthogonal component describes circles, whereas the parallel momentum is free and in the general case not necessarily zero. The radius of these spirals can be calculated for electrons near the Fermi surface via

$$r_c = \frac{v_D}{\omega_c} \stackrel{(2.24)}{=} \frac{v_D m^*}{eB}. \quad (2.25)$$

Another way to simply illustrate Landau levels is to plot the amount of electrons in one level as a function of the energy relative to the Fermi energy, as it was done exemplary for copper in Figure 2.5 for a few temperatures and magnetic fields. For an increasing magnetic field, as it is the case from Figure 2.5 b to Figure 2.5 a, the amount of Landau level decreases due to equation (2.23) while the amount of electrons within one level increases. These two effects compensate each other since the total amount of the electrons is constant. Hence, the integral over the density of states integrated over the energy stays the same.

If, however, the temperature is increased, according to equation (2.21) more electrons are in the energy regime above the Fermi level E_F and wash out the hard *Fermi edge* at $T = 0$ K. This is illustrated for example from Figure 2.5 a to Figure 2.5 c.

2.4.2 Cyclotron Resonance

Cyclotron resonance of electrons in solids is a powerful experiment to determine the effective mass and the Fermi surface of a crystal and was often applied to several simple metals [Fawcett, 1956; Kip *et al.*, 1961; Koch *et al.*, 1964; Häussler and Welles, 1966; Häussler, 1970; Langenberg and Marcus, 1964; Preppernau *et al.*, 1974], *semiconductors* [Dresselhaus *et al.*, 1955] or even more extraordinary materials such as *heavy fermions* [Tonegawa *et al.*, 2012, 2013] and *graphene* [Ozerin, 2014; Orlita *et al.*, 2008]. As shown in Figure 2.6 a, an external static magnetic field B_{static} is applied in z direction parallel to the sample surface forcing the electrons to move on helices twisted around the field direction. The exact energy is then given by equation (2.23) implying a free propagation along the field in z direction, but a quantized trajectory in the plane perpendicular to B_{static} with the *cyclotron radius* r_c given in (2.25).

If the measurement frequency ω of the orthogonally to the sample surface and hence orthogonally to B_{static} applied electric microwave field E_{rf} is equal to the cyclotron frequency $\omega_c = \frac{eB}{m^*}$, the electrons will absorb a remarkable part of the microwave field. In a frequency sweep this will look like an absorption maximum, since the electrons do not absorb much energy from the field in the off-resonance case.

From a technical point of view, it is challenging to sweep the measurement frequency, especially if the measurement method is resonant. But due to the field dependence of the cyclotron resonance frequency one can also sweep the magnetic field and obtains resonance and off-resonance frequencies. From the resonance condition it is possible to receive the effective electron mass by knowing the charge of an electron, the applied magnetic field and frequency.

The impact of a certain external magnetic field \vec{B} on an electron in a solid with the group velocity \vec{v}_g

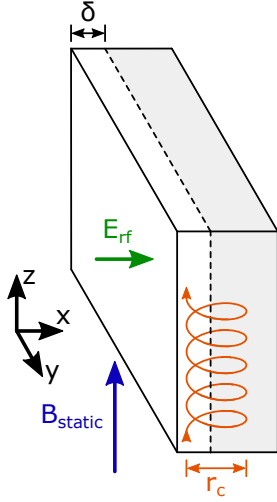


Figure 2.6 a: For a perfectly parallel aligned magnetic field B_{static} to the sample surface, multiple resonance dips are expected if the cyclotron radius r_c is larger than the skin depth δ .

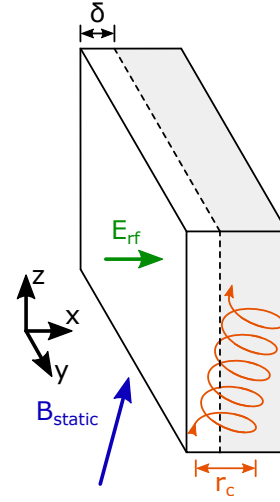


Figure 2.6 b: For a tilted magnetic field the electron spirals out of the skin depth and it gets impossible to have a distinct resonance since the electron is not affected by E_{rf} any more.

■ **Figure 2.6: Cyclotron resonance on a bulk sample with the skin depth δ .** A static magnetic field B_{static} is applied parallel to the surface which forces the electrons to move on spirals parallel to the magnetic field with the cyclotron frequency ω_c . An alternating electric field is then applied perpendicular to B_{static} to get into resonance with the spinning electron.

is given by the *Lorentz force* \vec{F}_L [Heaviside, 1889].

$$\vec{F}_L = -e (\vec{v}_g \times \vec{B}) \quad (2.26)$$

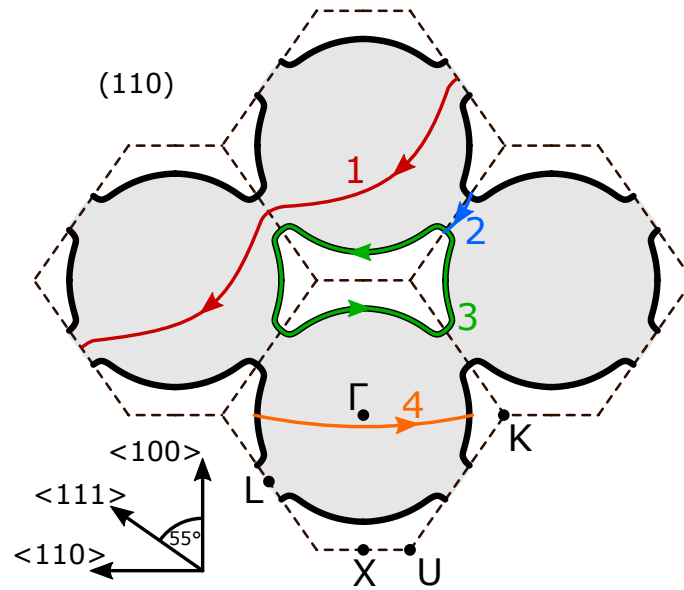
Rewriting force as derivative of momentum $\vec{F} = \dot{\vec{p}} = \hbar \dot{\vec{k}}$ and inserting equation (2.16) yields

$$\frac{d\vec{k}}{dt} \stackrel{(2.16)}{=} -\frac{e}{\hbar^2} (\nabla_k E(\vec{k}) \times \vec{B}), \quad (2.27)$$

where $\nabla_k E(\vec{k})$ is the energy gradient in k space. Hence, we know from the vector product that $d\vec{k}$ is always perpendicular to $\nabla_k E(\vec{k})$ forcing the electron to stay on areas of the same energy level, in particular on the Fermi surface. If there are closed trajectories, it is possible to probe the Fermi surface via cyclotron resonance.

Since an electron needs a free state if it absorbs energy, only electrons at the Fermi surface are able to absorb the microwave signal. Moreover, only electrons with a small change of the resonance frequency ω_c under a small k deviation contribute to the cyclotron signal, which is only the case for *extremal trajectories*. This is due to the fact that in the near surrounding of a non-extremal trajectory, a large variety of frequencies are observed, which does not lead to resolvable peaks in the observed spectrum. Therefore, the encircled area within the Fermi surface needs to be a local maximum or minimum. The remaining electrons on non-extremal orbits account for the background signal, but don't affect the signal itself.

In **Figure 2.7** the cross section of the (110) plane of the Fermi surface of copper is shown in an extended zone scheme. [Kip *et al.*, 1961; Hunklinger, 2011] For an external magnetic field in $\langle 100 \rangle$ direction



■ **Figure 2.7:** Two dimensional extended zone scheme of the Fermi surface of copper in the (110) plane. [Kip *et al.*, 1961] The colored trajectories are cyclotron orbits for different magnetic field directions. [Hunklinger, 2011] Orbit 2 and 4 are trajectories with a minimal and maximal circulated area respectively, whereas orbit 3 is a hole trajectory since there are no occupied states within the circulated area. Orbit 1 is an open trajectory, which cannot come into resonance. It should be noted that the orbits 1, 2 and 4 are not within in (110) plane.

exemplary the orange orbit 4 is an extremal trajectory, in this case a maximal one, which is why it is called *belly orbit*. The blue orbit 2 is a minimal one for the $\langle 111 \rangle$ direction and is called *neck orbit*. Orbit 3 is called *dog's bone*, since the revolved area of the electrons on the Fermi surface contains only non-occupied states at 0K, which his why it is a so called *hole orbit*. Finally, the red trajectory 1 is a path, which is not closed. Hence, electrons do not form closed orbits, have no chance to form a periodic movement and therefore do not contribute to any cyclotron signal.

Scattering rate

To observe cyclotron resonance at all, the involved electrons need to be able to fulfill several complete circulations of the spirals in [Figure 2.6 a](#) without scattering with the *scattering rate* Γ , because the process would drive the electron away from its original path and suppresses its contribution to the resonance signal. For the electrons it is possible to scatter in several ways: electron-electron scattering, phonon scattering, impurities, crystal defects, etc. Since most of the described processes decrease with a decreasing temperature it is necessary to perform all cyclotron resonance measurements at *liquid helium temperatures*. At this temperatures only the temperature-independent impurity- and crystal defect-scattering remain. While impurity scattering can be overcome by using a pure sample, crystal defects can be avoided with a single crystal without a lot of dislocations.

A good benchmark is the value of $\omega\tau$ with the probing angular frequency ω and the reciprocal value of the scattering rate $\tau = \frac{1}{\Gamma}$. In principle this value gives the ratio of measurement frequency to the scattering frequency and hence the amount of completed cycles within two scattering processes in the *thermodynamic average*.

The larger this value is, the more pronounced cyclotron resonance signal will be since electrons stay

for a longer time in resonance and do not get detracted from the spiral trajectory. This effect is also taken into account in a mathematical approach by Azbel' and Kaner [Azbel' and Kaner, 1957] later on in this section.

Skin Depth

In conducting materials electromagnetic waves only penetrate down to the skin depth δ from equation (2.9) into the sample. Therefore, electrons that are deeper than that length scale in the material, do not get affected by the probing microwaves. For pure copper the skin depth is given by several tens of nm, whereas the cyclotron radius r_c from equation (2.25) is larger by around three orders of magnitude for a comparable magnetic field.

This circumstance is schematically shown in Figure 2.6 a, where r_c penetrates deeper into the sample than E_{rf} does. Thus, electrons at the surface get accelerated or decelerated near the surface depending on their phase to the microwave. Since an absorption signal is visible if the electron is always accelerated, it needs to be in phase with the electromagnetic wave. This is possible if the microwave angular frequency ω is equal to the cyclotron angular frequency ω_c , but also for an integer multiple $n \cdot \omega_c$ for $n \in \mathbb{N}$ meaning that during one cyclotron cycle of the electron the polarity of the microwave field can switch for an integer amount of times.

The absorption signal then has multiple equidistant peaks as a function of the probing frequency for a fixed B . Plotting the absorption as a function of the magnetic field B , however, gives rise to peaks at integer fractions of the resonant field $\frac{B_c}{n}$.

These so called subharmonic resonances are considered in the equations by Azbel' and Kaner [Azbel' and Kaner, 1957] in the next paragraph as well. For non-conducting materials the skin depth is large compared to the cyclotron radius. This gives rise to only one single peak in absorption, which will be discussed after the Azbel'-Kaner cyclotron resonance.

Azbel' Kaner Cyclotron Resonance

For a mathematical treatment of cyclotron resonance in conductors Azbel' and Kaner derived a formula for the complex *surface impedance* Z_S of the sample. [Azbel' and Kaner, 1957]

$$Z_S(B) = Z_0 \sqrt[3]{1 - \exp\left(-\frac{2\pi i \omega}{\omega_c} - \frac{2\pi}{\tau \omega_c}\right)} \quad (2.28)$$

Here Z_0 is the complex surface impedance in zero field, which is given in equation (2.13) with the conductivity σ from equation (2.20) for a Drude-like behavior. Furthermore $\omega_c = \frac{eB}{m^*}$ is the cyclotron frequency from equation (2.24), ω the probing frequency and $\tau = \frac{1}{\Gamma}$ the reciprocal scattering rate.

Within this paragraph only the surface impedance will be discussed, whereas in the previous parts absorption was the key feature. The conjunction between those two quantities is the *conductivity* σ , whose real part σ_1 stands for the absorption and can be expressed in terms of the real and imaginary part of the surface impedance. [Dressel and Grüner, 2002]

For a better understanding the surface impedance is plotted in several ways in Figure 2.8. In Figure 2.8 a the real part, the imaginary part, and the absolute value are plotted over the normalized magnetic field for a rather large $\omega\tau$ of 100. Sweeping the magnetic field changes the cyclotron resonance frequency, which is responsible for the $\frac{1}{B}$ oscillation since the probing frequency is constant in this plot.

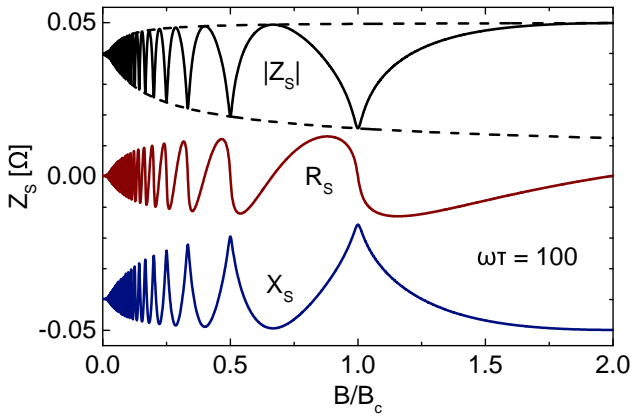


Figure 2.8a: Complex surface impedance with two enveloping functions and quite distinct resonance dips.

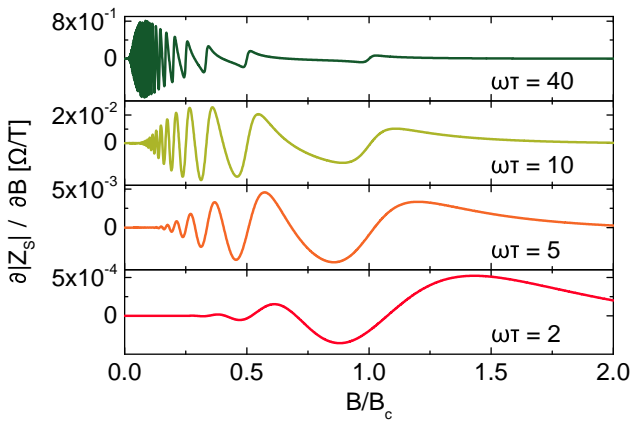


Figure 2.8b: Derivative of the absolute value of the surface impedance with cyclotron resonance dips for different values for $\omega\tau$.

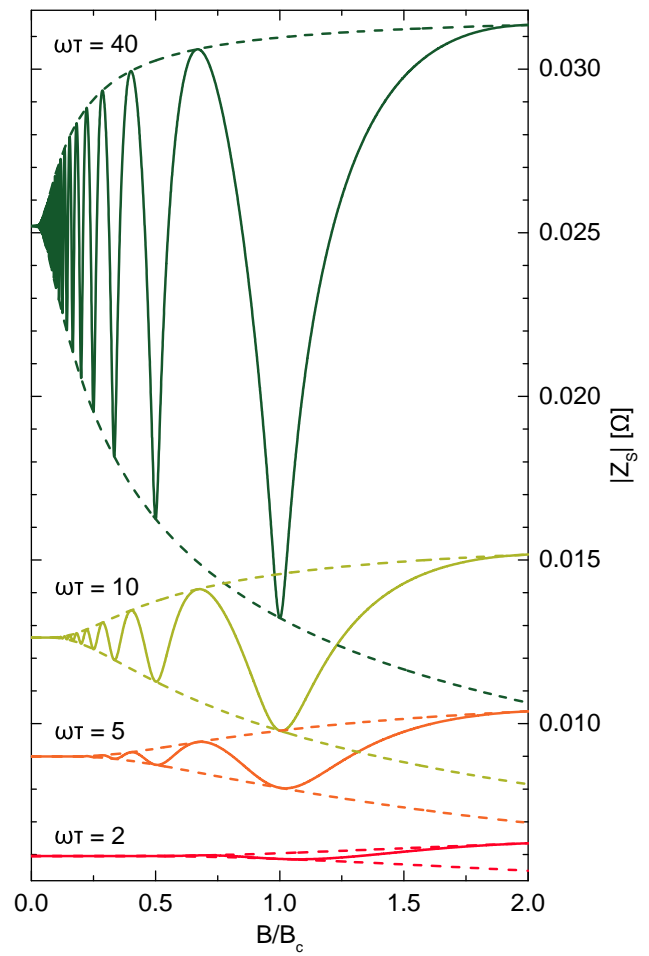


Figure 2.8c: Absolute value of the surface impedance and its enveloping functions, which opens at higher fields for larger $\omega\tau$ with a fixed value of ω .

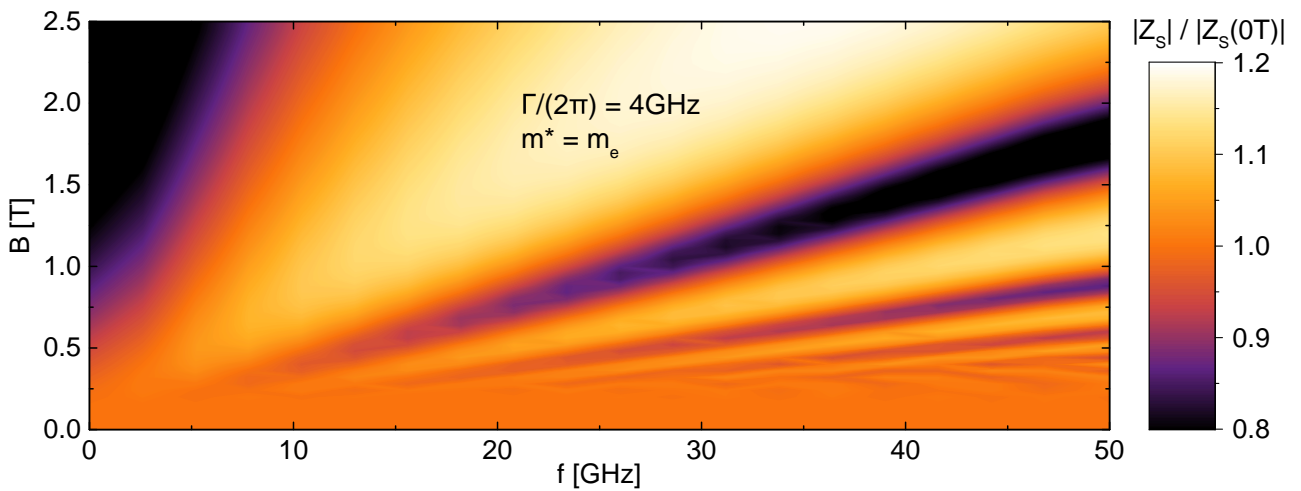


Figure 2.8d: Field- and measurement frequency-dependent surface impedance normalized to zero field with cyclotron resonance lines.

■ Figure 2.8: Several plots of the Azbel'-Kaner-cyclotron resonance according to equation (2.28).

Actually R_S and X_S do not even match in zero field since the probing frequency is comparable high in comparison with the scattering rate. Hence, this calculation is not in the *Hagens-Rubens regime* anymore.

Clearly visible is a dip in $|Z_S|$ at the resonance field B_c , which is reasoned in the absorption of the microwaves by the electrons on their spiral trajectories.

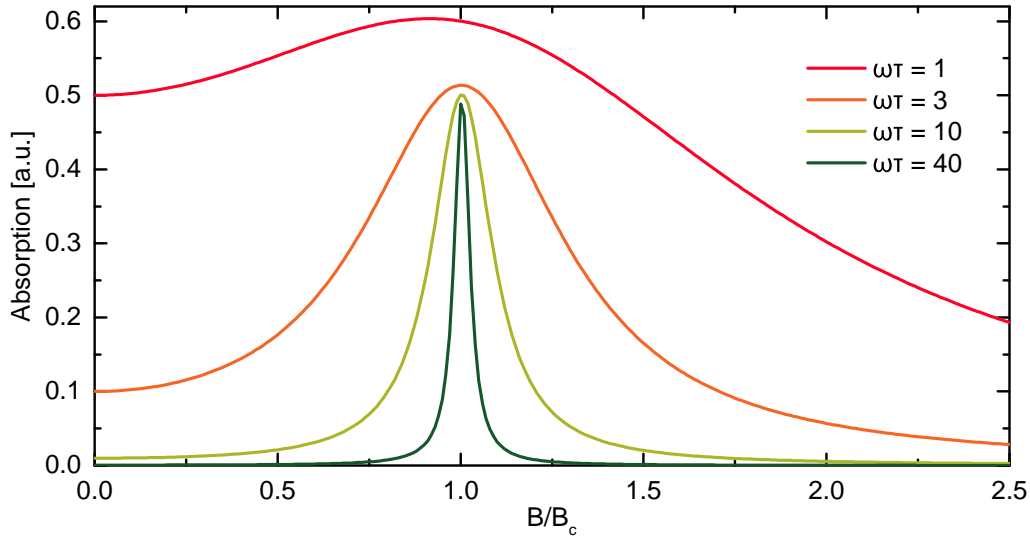
That there are also dips at every integer fraction $\frac{B_c}{n}$ of the resonance field is due to effect of skin depth, which is in this case shorter than the cyclotron radius as explained in the paragraph above. For $|Z_S|$ a top and bottom enveloping function is plotted in dashed lines, where the surface impedance is oscillating in between. Above B_c they behave pretty flat, whereas from zero field up to half the cyclotron field they split from one another with a rather large slope. The field, at which this splitting occurs, is well below B_c for $\omega\tau = 100$, which is why many *subharmonics* are visible.

Figure 2.8 c shows the same absolute values of the surface impedance $|Z_S|$ plotted over the normalized magnetic field, but for several values for $\omega\tau$. One should be aware of two key features in this plot. First, with an increasing $\omega\tau$ the two dashed enveloping functions span up a larger absolute range in impedance, making the signal more pronounced and easier measurable. Secondly, the point at which the two enveloping functions split decreases for higher $\omega\tau$, which is why for low $\omega\tau$ only a few subharmonics are visible, whereas for high $\omega\tau$ quite a huge amount are resolvable.

This last point is also the main message in Figure 2.8 b, where the derivative $\frac{\partial|Z_S|}{\partial B}$ is plotted over the normalized field. This derivative of the surface impedance is actually the way, how cyclotron resonance is plotted usually in literature, to get rid of the offset in surface impedance. Subharmonic features are visible for all $\omega\tau$, but rather more distinct for higher $\omega\tau$. In the derivative the enveloping functions do not only open at certain magnetic field, but also converge again. This taper is due to the $\frac{1}{B}$ oscillation of the surface impedance in Figure 2.8 c. Hence, there is always one (sub-)harmonic resonance dip being the most pronounced, which is from top to bottom in Figure 2.8 c the 11th, the 3rd, the 2nd and the 1st, starting counting from the left. In fact, the derivative is oscillating even at lower fields for all $\omega\tau$, but its simply not resolvable for low values. Another important point is the signal strength, which is in this case larger by more than three orders of magnitude from the highest to the lowest value for $\omega\tau$, which is only a factor of 20.

Finally in Figure 2.8 d the zero field normalized surface impedance is plotted as a color map against the absolute magnetic field and the absolute frequency. The assumed parameters for this calculation are close to the ones for copper with an effective electron mass of $1m_e$, a *charge carrier density* of $8.5 \cdot 10^{22} \frac{1}{\text{cm}^3}$ [Ibach and Lüth, 2009] and a DC resistivity of $2 \text{ n}\Omega\text{cm}$ (imposing an *residual resistance ratio* (RRR) of around 2000), yielding a scattering rate of $\frac{\Gamma}{2\pi} = 4 \text{ GHz}$ for a Drude-like behavior. Since the probing frequency $f = \frac{\omega}{2\pi}$ is constantly changing on the x axis, the value for $\omega\tau$ is only constant for a vertical line in the graph. For frequencies below $f = 4 \text{ GHz}$ no resonance dips are visible, since this is exactly at $\omega\tau$, meaning that an electron scatters once within one cyclotron cycle in the thermodynamic average. The more one follows the graph to the right, the larger $\omega\tau$ becomes and hence, the oscillating dips become pronounced more clearly and more subharmonics are resolvable.

From these graphs it becomes clear that for gaining a good identifiable cyclotron signal it is necessary to have a much higher probing frequency relative to the resonance frequency to observe cyclotron resonance since with an increasing $\omega\tau$ the signal becomes larger in absolute values and due to a smaller splitting field of the enveloping functions, more subharmonics are resolvable. Moreover, especially



■ **Figure 2.9: Cyclotron resonance absorption peak of a non-conducting sample.** Four different peaks for various values for $\omega\tau$ are plotted over the magnetic field B . With an increasing $\omega\tau$ for a fixed ω the peak gets sharper making it easier to verify it experimentally.

Figure 2.8 d shows that multiple subharmonics can be seen both in a frequency sweep with constant magnetic field as well as vice versa.

Cyclotron Resonance for Insulating and Weakly Conducting Materials

The argument of exceeding the skin depth of the electron does not hold for materials with lower conductivity since the skin depth is not small enough to undercut the cyclotron radius. Hence, for instance in semiconductors there is typically only one peak in each spectrum. Starting from the *equation of motion* of an electron within an electric and magnetic field [Dresselhaus *et al.*, 1955] the real part of the conductivity σ_1 can be derived.

$$\sigma_1(B) = \sigma_0 \frac{1 + \left(\frac{\omega}{\Gamma}\right)^2 + \left(\frac{\omega_c(B)}{\Gamma}\right)^2}{\left(1 - \left(\frac{\omega}{\Gamma}\right)^2 + \left(\frac{\omega_c(B)}{\Gamma}\right)^2\right)^2 + 4\left(\frac{\omega}{\Gamma}\right)^2} \quad (2.29)$$

Here σ_0 is the DC conductivity as given in equation (2.20), $\omega = 2\pi f$ the probing frequency, $\omega_c = \frac{eB}{m^*}$ the cyclotron frequency from equation (2.24) and Γ the scattering rate. Since σ_1 is proportional to ε_2 , it basically describes the absorption of the sample which itself, however, is proportional to the *bandwidth* f_B of a resonant cavity, as it will be described later on in sections 3.3 and 3.4.

In Figure 2.9 the absorption signal is plotted over the normalized magnetic field for different values of $\omega\tau$. In materials with a large skin depth compared to the cyclotron radius, subharmonic oscillations as in Azbel'-Kaner cyclotron resonance are completely suppressed. Hence, just a single peak is visible at $B = B_c$.

From top to bottom the signal strength is rising since the scattering rate decreases. As well as for conducting materials, the argument for a better detectable signal with an increasing $\omega\tau$ also holds for non-conducting materials.

Alignment with external static magnetic field

For metallic samples the skin depth also has another impact on the presence of a measurement signal. This is due to the adjustment of the external magnetic field relative to the sample surface. In particular the field should be right in the plane of the sample surface. In [Figure 2.6 b](#) it is shown how the trajectories look like if the external field is tilted. The electrons are still on helices but no longer parallel to the surface, which is not a problem for the resonance condition in the first place.

By considering the skin depth it turns out to be fatal if the angle is too large. The trajectory spirals out from the reachable volume for the electric microwave field underneath the skin depth and is no longer affected by E_{rf} , which is why this electron will not contribute to any resonance signal anymore.

To overcome this fade out of the electron the magnetic field has to be perfectly aligned with the sample surface to keep the trajectory within the skin depth as in [Figure 2.6 a](#). Furthermore, the sample should be polished for a rather flat surface without any curvature. Otherwise the field can be aligned to one part of the sample, whereas it is tilted on the other side.

Relation to Electron Paramagnetic Resonance

Regarding the type of measurement, cyclotron resonance is rather similar to *electron paramagnetic resonance* (EPR) [Zavoisky, 1945] with only one conceptual difference. For EPR an alternating parallel magnetic field excites the electrons from the lower to the higher *Zeeman state* [Zeeman, 1896], whereas in case of cyclotron resonance an alternating perpendicular electric field accelerates the electrons to a higher Landau level.

Solving equation (2.24) for the frequency yields

$$f_c = \frac{1}{m^*} \frac{eB}{2\pi}, \quad (2.30)$$

whereas in EPR the resonance condition is given by

$$f_{\text{EPR}} = \frac{g}{2m_e} \frac{eB}{2\pi}. \quad (2.31)$$

Obviously they both depend linearly on B , making it hard to distinguish between both signals if the bandwidth is in the same order for both signals. For a free electron gas with $g = 2$ and $\frac{m^*}{m_e} = 1$ the resonance peaks in absorption are even at the same field for equal frequencies.

2.5 Nb doped STO

2.5.1 Nb doped STO as a Material

Roomtemperature Behavior

Strontium titanate SrTiO_3 (STO) is a *indirect wide-bandgap semiconductor* having a gap of 3.2 eV between 2p levels of oxygen and 3d levels of titanium [Cardona, 1965] within a *perovskite structure* (see [Figure 2.10 a](#)). Upon cooling the *dielectric function* raises from around 300 at room temperature to several ten thousands at cryogenic temperatures below 4 K, but still remaining a *paraelectric material* [Müller and Burkard, 1979]. At this temperatures also the degeneracy of the t_{2g} electronic orbitals

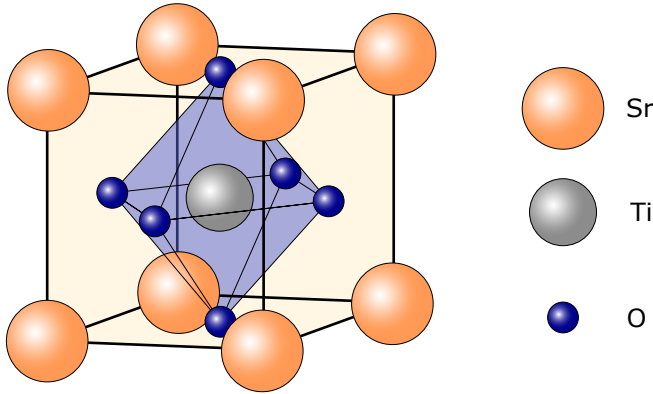


Figure 2.10a: Atomic schematic of STO showing a typical perovskite pattern with titanium in the middle, strontium forming a surrounding cube and oxygen on the intersection of the face diagonals.

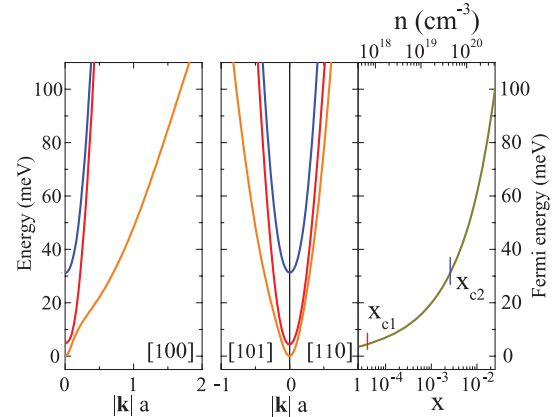


Figure 2.10b: The dispersion relation calculated via a tight-binding model for the 3d orbitals of titanium. The right plot shows the Fermi energy as a function of doping with two critical levels, where new bands are filled.

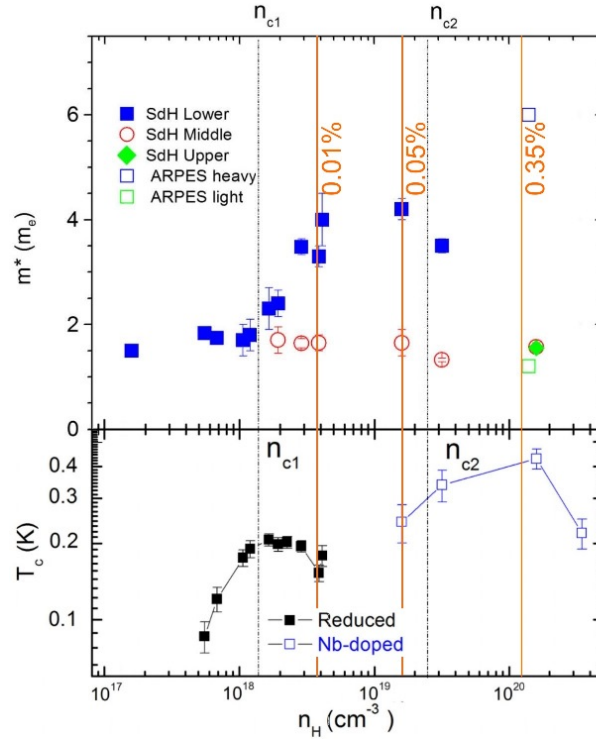
■ **Figure 2.10: Atomic schematic and dispersion relation of STO.** [van der Marel *et al.*, 2011]

of the titanium atoms is completely abolished due to *spin-orbit coupling* and *tetragonal distortion*. Hence, three different bands arise around the Γ point within the Brillouin zone [van der Marel *et al.*, 2011] as it can be seen in [Figure 2.10b](#) for three different crystal orientations. Each of this t_{2g} bands belongs to an ellipsoidal shaped area on the Fermi surface along the main crystal axis [Aiura *et al.*, 2002] and has been successfully proved by ARPES measurements [Chang *et al.*, 2010]. These bands can be filled successively with electrons in different ways, turning STO to a nice model system for multi band superconductors. Either oxygen is slightly removed to gain SrTiO_{3-x} or the inner Ti^{4+} atoms are partly replaced by Nb^{5+} atoms ending up in $\text{SrTi}_{1-x}\text{Nb}_x\text{O}_3$, both giving rise to free *conduction electrons* within the crystal. Upon these kinds of doping the three degenerated bands are filled giving rise to a grow of the Fermi energy as illustrated in the right plot of [Figure 2.10b](#). Therefore, the ellipsoidal shaped Fermi surface increases successively. [Plumb and Radovic, 2017; Lin *et al.*, 2013, 2014a; Takizawa *et al.*, 2009]

Superconductive Behavior

Both in oxygen reduced [Koonce *et al.*, 1967] and Nb doped [Pfeiffer and Schooley, 1969] STO *domes of superconductivity* as a function of doping have been published and are shown in the bottom subplot of [Figure 2.11](#) [Lin *et al.*, 2014a]. One remarkable feature is the rather low *charge carrier concentration* n and hence, a rather low Fermi level E_F , which is even lower than the corresponding *Debye temperature* T_D , which is not consistent with common weak-coupling limit in BCS theory. [Lin *et al.*, 2013] As a consequence, several unconventional superconducting coupling mechanisms have been suggested, such as *long-range dipolar interactions* near to the *ferroelectric quantum critical point* [Rowley *et al.*, 2014], *plasmons* and *polar optic phonons* [Takada, 1980] or *soft optical phonons* in the *tetragonal phase* [Appel, 1969].

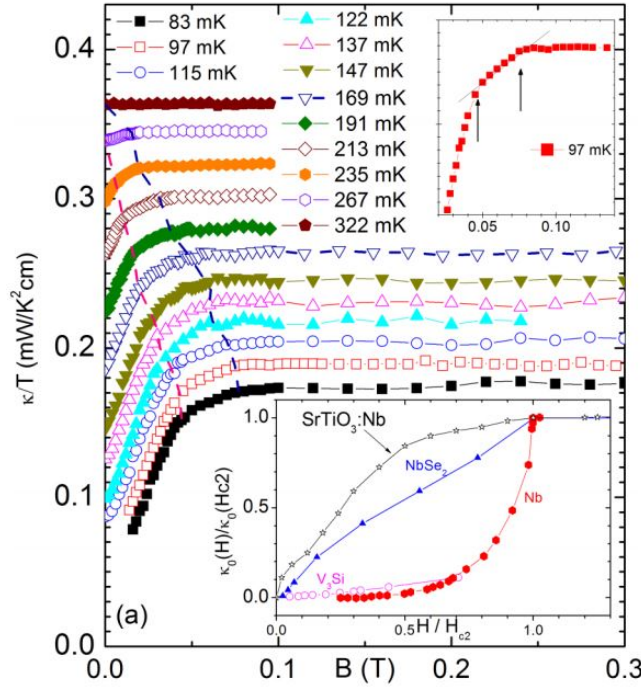
The origin of these superconducting domes is still under debate. For doping levels below the superconducting dome, the charge carrier concentration is not high enough to maintain superconductivity, whereas for doping levels above the dome, decreasing *quantum fluctuations* between the two minima



■ **Figure 2.11: Effective masses and the two superconducting domes in Nb-STO.** [Lin *et al.*, 2014a] The orange lines represent the doping of the three samples within this work. The effective electron masses in the top plot are measured via Shubnikov–de Haas quantum oscillations. For the doping levels of our samples (see [Table 2.1](#)) the lower mass gets as low as $1.3 m_e$, while the heavier one is around $4.0 m_e$. The bottom plot shows the two superconducting domes of Nb-STO as a function of doping. These domes extend over three orders in magnitude of doping.

within the ferroelectric *double well potential* might suppress superconductivity, as it was recently suggested [Edge *et al.*, 2016].

As measured with *tunneling measurements* [Binnig *et al.*, 1980] and *thermal conductivity measurements* [Lin *et al.*, 2014b] (shown in [Figure 2.12](#)), several bands contribute to this *s-wave superconductivity* [Lin *et al.*, 2015b] giving rise to several effective electron masses as shown in the upper plot of [Figure 2.11](#). However, in spectroscopic measurements there is only one *superconducting gap* visible [Thiemann *et al.*, 2018; Swartz *et al.*, 2018], revealing the question why several bands should by chance have the same gap. This can be explained by *Andersons Theorem* [Anderson, 1959] as explained in detail in [Mitrovic, 2008] along the *two-band superconductor* MgB_2 . It goes along with a more generalized *time-reversal* pairing of *one-electron states* instead of the $|k, \uparrow\rangle - |-k, \downarrow\rangle$ pairing from *BCS theory* [Bardeen *et al.*, 1957]. In this case scattering *s-wave superconductivity* is not completely destroyed in the first place, but all superconducting gaps are averaged over the whole Fermi surface since an electron cannot be assigned to a certain band anymore due to scattering.



■ **Figure 2.12: Field-dependent kinks in thermal conductivity.** The main plot shows two kinks in the shape of the field-dependent thermal conductivity marked with a blue and a red line. [Lin *et al.*, 2014b] These kinks have been interpreted as evidence for a two-gap superconductivity.

Nb-Doping	$n_{\text{Hall}}(2\text{K})$	$\frac{\Gamma}{2\pi}(2\text{K}, m^*=4m_e)$	T_c	Δ	$\rho_{\text{DC}}(2\text{K})$
0.01%	$3.7 \cdot 10^{24} \frac{1}{\text{m}^3}$	6.14 GHz	-	-	$1.5 \mu\Omega\text{m}$
0.05%	$1.4 \cdot 10^{25} \frac{1}{\text{m}^3}$	9.46 GHz	-	-	$0.66 \mu\Omega\text{m}$
0.35%	$1.1 \cdot 10^{26} \frac{1}{\text{m}^3}$	64.07 GHz	346 mK	50.5 meV	$0.52 \mu\Omega\text{m}$

■ **Table 2.1: All used Nb doped STO samples within this work.** The DC resistivity ρ_{DC} and the charge carrier density n was measured with Hall measurements in a magnetotransport setup at magnetic fields up to 4 T. [Thiemann *et al.*, 2018] For the two lowest doped samples there was no superconductivity discovered down to 20 mK.

2.5.2 Nb doped STO Samples

In [Table 2.1](#) all Nb doped STO samples within thesis are listed. Cyclotron resonance measurements were done on the two lowest doped samples, while superconducting experiments have been performed on the highest doped.

For all samples the *Hall coefficient* R_{H} and the DC resistivity ρ_{DC} was probed with *magnetotransport measurements* in a *van der Pauw* setup at 2 K, as outlined in the supplemental material of [Thiemann *et al.*, 2018]. Using these values, the charge carrier density n_{Hall} can be derived.

Experimental Basics

For having a short introduction in the experimental principles this section gives a brief overview starting with all used setups. Afterwards the measurement devices itself - in fact *microwave waveguides* - and the underlying *cavity perturbation theory* are sketched followed by the procedure of analyzing the microwave data. In the end a short summary of the used samples and materials within this thesis is listed.

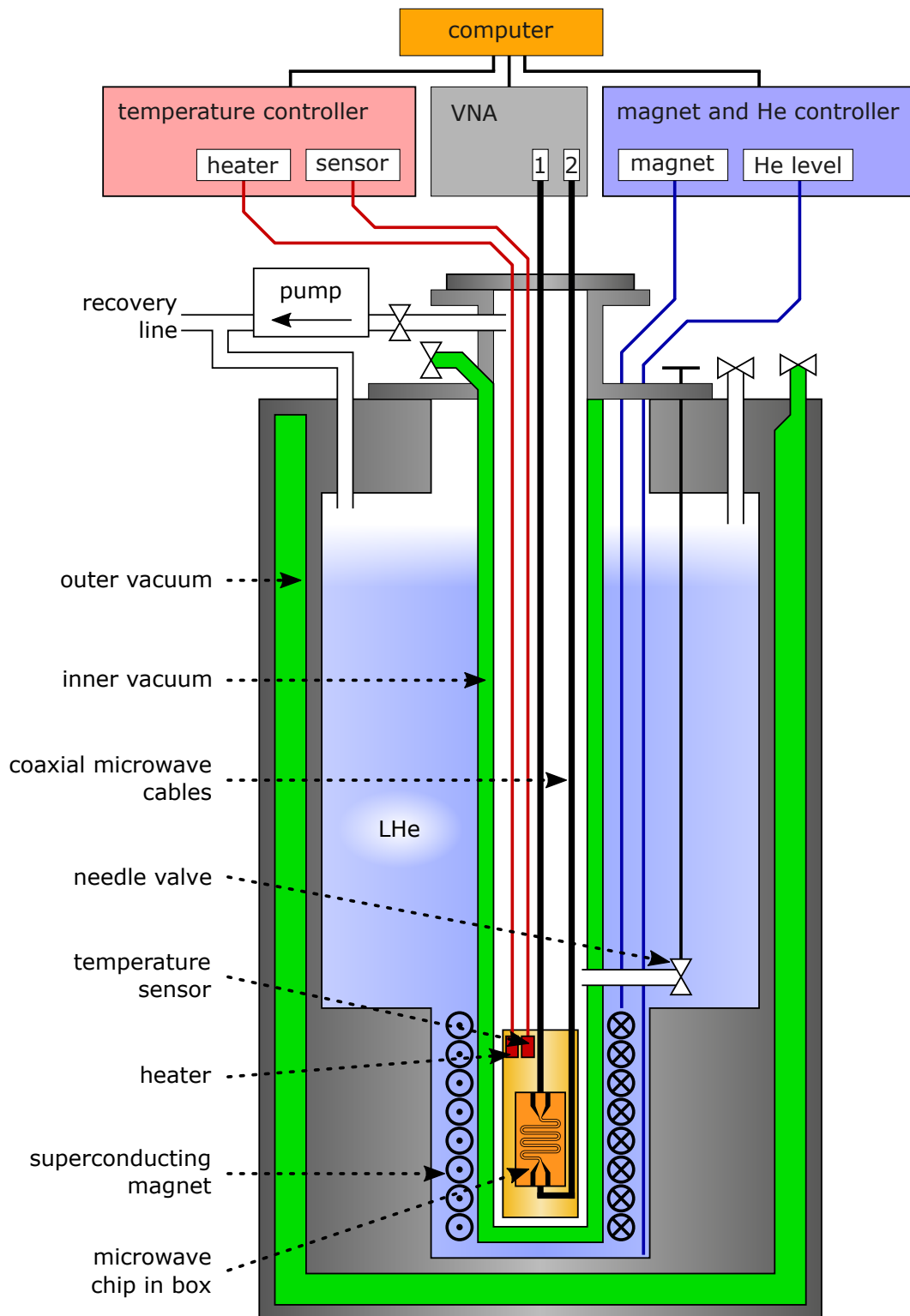
3.1 Setups

Within this thesis mainly three different setups were used. The first two are microwave setups up to 50 GHz where the lowest reached temperatures lay in the range of 1.5 K and 20 mK, respectively. The third and last one is a DC setup to obtain characteristic resistivities.

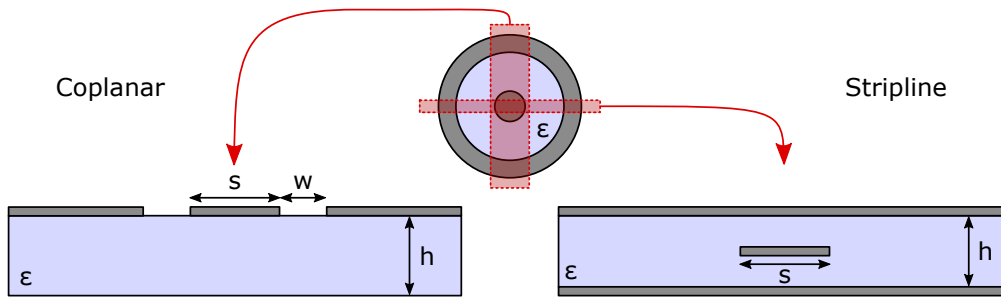
3.1.1 Bath Cryostat

For almost all cyclotron measurements a liquid helium *bath cryostat* was used. A schematic sketch can be seen in [Figure 3.1](#). Inside an insulating vacuum is the liquid helium bath with a superconducting magnet on the bottom reaching fields from 0 to 8 T. The sample chamber is placed in an inner *variable temperature inset* (VTI) including all the measurement and control cables. To reach temperatures below the boiling point of liquid helium a pump can lower the pressure inside the *sample chamber* while the helium bath is uncoupled by the impedance of the *needle valve*, which enables temperatures down to 1.5 K.

A manual for this setup can be found in section A of this thesis.



■ **Figure 3.1: Schematic of the bath cryostat.** This includes the variable temperature inset (VTI), the microwave box and measurement and control devices.



■ **Figure 3.2: Coplanar and stripline waveguides.** Both waveguides can be imagined as a cut through a coaxial cable with ongoing inner and outer conductors and a substrate in between.

3.1.2 Dilution Refrigerator

All *sub-Kelvin* measurements are performed in a *dilution refrigerator*. The cooling method was first proposed by [London *et al.*, 1962] and finally realized in 1964 [Das *et al.*, 1964]. In principle a *helium mixture* of two isotopes forms two separate phases below 0.86 K, where one is rich of helium-3 and the other one poor. This equilibrium can be destroyed by pumping even more He^3 atoms from the poor in the enriched phase. If the concentration drops below 6.5% the helium-3 atoms get back from the concentrated phase via a phase transition, which needs a certain amount of energy in the form of heat from the surrounding. Limited by heat entry from the environment one can reach temperatures down to several tens of milli Kelvin.

3.1.3 DC setup

The DC measurement setup basically is a *glass cryostat* cooled with liquid nitrogen and helium separated by several layers of vacuum. By decreasing the pressure of the helium bath one is able to reach temperatures down to 1.4 K. The *sample holder* consists of two slots for *four point DC resistance measurements*. Current is applied by a *source measure unit* of Keithley and the subsequent voltage is measured by a *nanovoltmeter* (see [Table 3.2](#)).

3.2 Microwave Waveguides

To bring the sample in contact with the AC magnetic and electric fields in the GHz range, a *microwave waveguide* is used, as it illustrated in [Figure 3.2](#). Here, two possible designs are shown, so called *coplanar* [Clauss *et al.*, 2013; Wiemann *et al.*, 2015] and *stripline* [Scheffler *et al.*, 2012]. Both waveguides can be imagined as a deformed *coaxial cable*, where *TEM modes* are guided through the substrate. In an ideal setup the impedance of the waveguide is perfectly aligned with the impedance of the connected coaxial cable.

The sample always lays on top of the waveguide, where both the electric and magnetic fields shine on the sample as shown in [Figure 3.3](#). A remarkable feature of the electric field lines for a conducting sample are their perpendicularity towards the sample surface in both the coplanar and the stripline design, whereas the magnetic lines are strictly parallel in both cases. Another remark shall be said about the static magnetic field, which is not part of this figure. For both designs it straightly comes out of the *plane of projection*, achieving an orthogonal system of static magnetic field along the sample

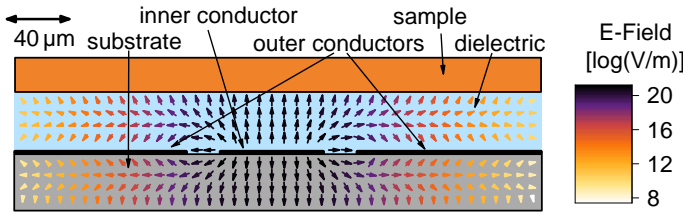


Figure 3.3 a: Electric field of a coplanar chip.

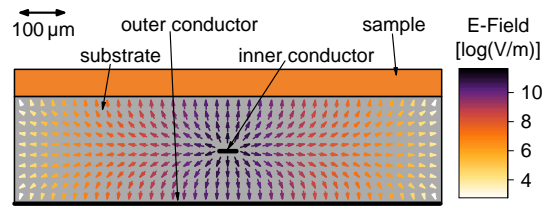


Figure 3.3 b: Electric field of a stripline chip.

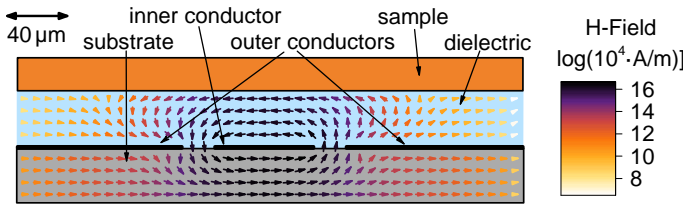


Figure 3.3 c: Magnetic field of a coplanar chip.

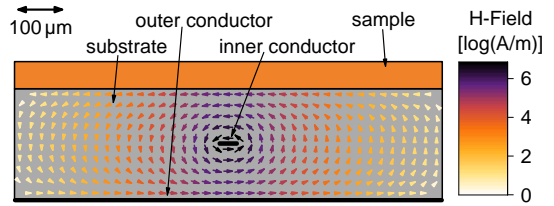


Figure 3.3 d: Magnetic field of a stripline chip.

■ **Figure 3.3:** Numerical simulations of the electric and magnetic fields within a coplanar and a stripline chip. Both electric fields are perfectly perpendicular towards the sample surface for a conductive sample, whereas the magnetic is parallel.

surface and the microwave electric field as it is requested in section 2.4.2.

The microwave chip is implemented inside a box out of brass. (see Figure 3.4) Inside the box itself a substrate is placed, where the conducting waveguide is evaporated on to. The actual sample is placed on top of the chip and its influence on the propagating electromagnetic waves gives rise to the measurement signal. As shown in Figure 3.4 b this kind of waveguides exists in both *broadband* and *resonant* types. While a simple *transmission line* offers measurements on the complete frequency range, a gap on the other hand makes the waveguide resonant to a certain *resonance frequency* f_0 given by the dielectric constant of the substrate and the distance of the waveguide between the two gaps. The latter goes along with a hard restriction of the measurements frequencies to only the resonance and its higher harmonic modes. However, due to the back and forth propagation of the photons within the two gaps the resonant waveguide becomes much more sensitive to the influence of the sample than a broadband one. The size of the gap can be varied. A large gap decreases the *coupling strength* of the resonator, but also lowers the *full width at half maximum* (FWHM) $2f_B$ and hence increases the *quality factor* $Q = \frac{f_0}{f_B}$ of the resonance.

At the end of the chip the inner conductor is connected with *conductive silver* to the center conductor of a connector, whereas the two outer conductors are coupled through the brass box itself. The whole measurement box can be easily connected via coaxial cables to the *network analyzer*.

Finally in Figure 3.5 the electric fields of the first three modes are plotted over a resonant coplanar waveguide. As the gap is an open end for the electric field, the number of knots n matches the n -th mode.

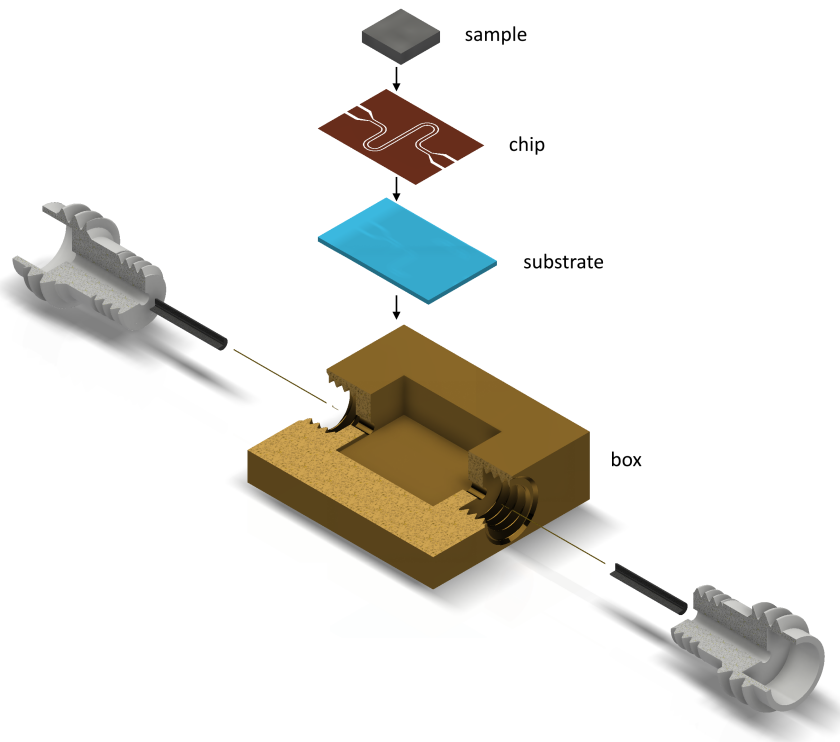


Figure 3.4 a: In this explosion sketch a microwave box is shown. Inside the box of brass a substrate is placed with the waveguide evaporated on top for a coplanar waveguide. The sample is placed on top. For a conducting sample something insulating has to be put in between to prevent an electrical short of inner and outer conductor. At the back and front sides of the box two microwave connectors are placed, where coaxial cables can be mounted to. The inner conductor is connected via a small plug and conductive silver to the center conductor of the waveguide.

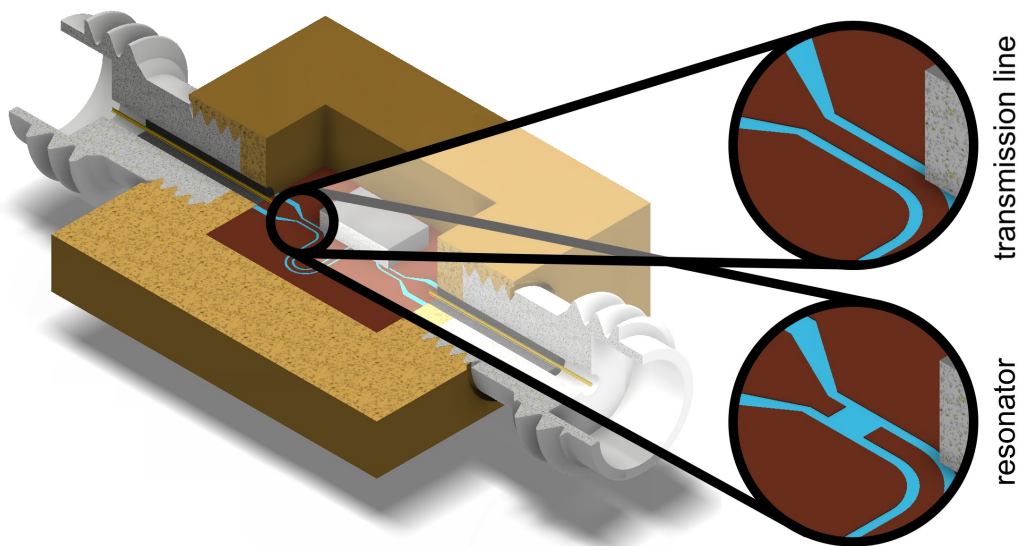
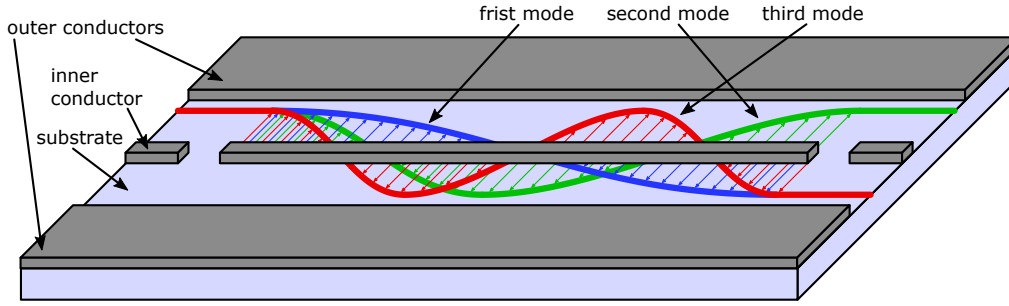


Figure 3.4 b: In this sketch the microwave box can be seen with all its components and the sample itself. The two insets show the difference between a broadband and a resonant waveguide.

■ **Figure 3.4:** Microwave waveguide inside the microwave box.



■ **Figure 3.5: Amplitude of the electric fields of the first three modes in a coplanar resonator.** Inside a resonant measurement device only probing frequencies that are a multiple of the resonance frequency f_0 can be accessed. Since for a $\frac{\lambda}{2}$ -resonator both edges are open ends for the electric field the fundamental frequency has one node in the middle of the resonator. The second and third mode have one and two additional nodes, respectively.

3.3 Fitting Process

In microwave experiments typical dimensions of the used measuring equipment are quite often in the same length scale as the wavelength in the GHz-regime, which causes unwanted wave reflections within the cables. This in fact evokes *standing waves* interfering with the actual measurement signal. To overcome these influences of the standing waves one in principle can go two different ways.

Unless the standing wave features are not caused by a non-linear reason [Zinßer, 2016; Zinßer *et al.*, 2018], they can be calibrated, as it is performed for reflection measurements within a *Corbino geometry* [Corbino, 1911] by using three different *standard samples* [Scheffler and Dressel, 2005] for each frequency and temperature. This is successfully performed by several groups [Booth *et al.*, 1994; Scheffler and Dressel, 2005; Kitano *et al.*, 2008; Mondal *et al.*, 2013; Liu *et al.*, 2014].

Secondly for non-broadband spectroscopy methods it can be used, that the bandwidth of a resonant mode within a microwave resonator is much sharper than the period of the standing waves. Thus it possible to treat this background with a linear approximation in the near surrounding of the resonance. [Oates *et al.*, 1990; Petersan and Anlage, 1998; Klein *et al.*, 1993; Ebensperger *et al.*, 2016] Within a resonant measurement device, the line shape of the absolute value of the \hat{S}_{21} parameter in transmission is given by a *Lorentzian distribution* [Dressel and Grüner, 2002]

$$L(f) = A \frac{f_B}{4(f - f_0)^2 + f_B^2} \quad (3.1)$$

with the resonance frequency f_0 , the FWHM $2f_B$ and the maximum height $\frac{A}{f_B}$. Nevertheless, due to the above mentioned superpositions of the resonance with the standing wave pattern it is rather useful to fit the response function in a complex way, as it can be seen in [Figure 3.6 a](#). For this purpose the complex *analytic continuation* of the Lorentzian is used, where $f_0 + if_B$ becomes \hat{c}_3 .

$$\hat{L}(f) = e^{-2\pi i \hat{c}_1 f} \left(\frac{\hat{c}_2}{f - \hat{c}_3} + \hat{c}_4 + \hat{c}_5 (f - \text{Re}(\hat{c}_3)) \right) \quad (3.2)$$

Here the first summand is the Lorentzian itself, whereas the second and third represent a first order *Taylor polynomial* around the resonance frequency f_0 . The exponential term represents the frequency dependent *phase shift*. From the two functions the resonance frequency and FWHM are given via $f_0 = \text{Re}(\hat{c}_3)$ and $\text{FWHM} = 2f_B = 2 \text{Im}(\hat{c}_3)$. Using this complex approach the phase information can

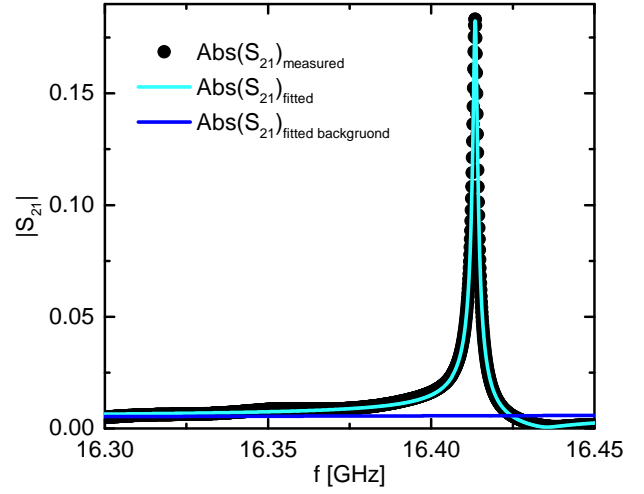
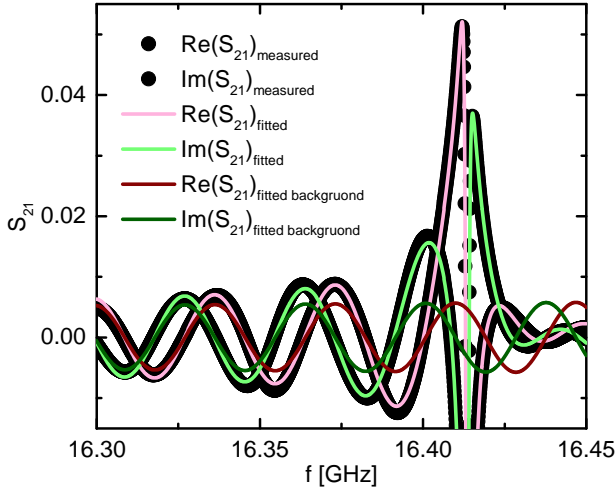


Figure 3.6a: Measured real and imaginary part and both the complete and the background fit.

Figure 3.6b: Measured absolute value and both the complete and the background fit.

■ **Figure 3.6: Complex fitting procedure for the tenth mode of a superconducting lead stripline resonator.** Real and imaginary part of \hat{S}_{21} are fitted with a Lorentzian resonance in addition to a standing wave background according to equation (3.2). For visualization only the background fit without the resonance is plotted additionally. It matches perfectly the measurements points for frequencies remote from the resonance. The absolute value is then calculated afterwards from the complex fit.

be used for the fit as well. The absolute value can be derived afterwards from the complex function and is not included in the fitting procedure itself.

3.4 Cavity Perturbation Theory

For calculating the complex surface impedance Z_S of a sample inside a resonator *cavity perturbation theory* [Klein *et al.*, 1993] is applied in this thesis. It is a powerful tool since the exact field distributions inside the disturbed cavity is not needed to be known, but only works for small perturbations coming from the sample since the disturbed fields E_1 and H_1 are approximated with the undisturbed fields E_0 and H_0 .

When inserting a sample with the permittivity ε_1 and permeability μ_1 the relative shift in resonance frequency towards the undisturbed cavity with the permittivity ε_0 and permeability μ_0 is given by [Pozar, 1998]

$$\frac{f_0 - f_1}{f_0} = \frac{\int_V \left((\varepsilon_1 - \varepsilon_0) E_1 \cdot E_0^* + (\mu_1 - \mu_0) H_1 \cdot H_0^* \right) dV}{\int_V \left(\varepsilon_0 E_1 \cdot E_0^* + \mu_0 H_1 \cdot H_0^* \right) dV} \quad (3.3)$$

where all indices 0 belong to the original cavity and indices 1 to the slightly disturbed cavity. As the complex surface impedance is given by the ratio of the electric and magnetic field it can be derived [Broun, 2000] as

$$Z_S = R_S + iX_S = \gamma \left(f_B - 2i\Delta f_0 \right) \quad (3.4)$$

as R_S and X_S are the *surface resistance* and *reactance* respectively, γ a *geometry factor* of the cavity itself and Δf_B and Δf_0 the shifts in bandwidth and resonance frequency of the corresponding resonant mode.

In the case of a superconductor as a probing material, to gain absolute numbers for Z_S and σ , a so called R_S - X_S -matching is performed in the metallic state inside the Hagen-Rubens regime. Here the probing frequency ω is much smaller than the scattering rate Γ .

In particular equation (2.13) yields

$$\sigma_2 = \frac{\omega\mu_0\mu_1 (X_S^2 - R_S^2)}{R_S^4 + 2R_S^2X_S^2 + X_S^4} \quad (3.5)$$

for the imaginary part of the conductivity, which is vanishing for low frequencies ($\sigma_2(\omega \ll \Gamma) \rightarrow 0$). To fulfill this condition, R_S has to equal X_S in equation (3.5). This leads via equation (3.4) to the identification of $f_B = 2\Delta f_0$, making it possible to calculate the offset in the resonance frequencies.

Afterwards equation (2.13) can be solved for σ and numbers for R_S and X_S can be plugged in. By knowing σ_{DC} the geometry factor γ can be calculated via $\sigma_1(\omega \rightarrow 0) = \sigma_{DC}$ to obtain absolute numbers for the complex conductivity.

3.5 Lists of used samples and equipment

In this section several lists are given to get necessary details for the reproducibility of all experiments.

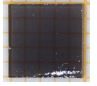
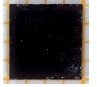
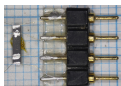


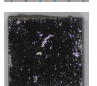
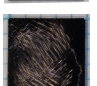



3.5.1 Samples

The used samples for this thesis can be found in [Table 3.1](#).

All Nb-STO samples were kindly provided by the group of Prof. Dr. Jochen Mannhart of the Max Planck Institute of Solid State Research in Stuttgart, Germany.

The copper single crystal was commercially bought at MaTecK in Jülich, Germany.

The UPd_2Al_3 thin film sample was grown on a LAO substrate in (111) direction by Martin Jourdan at the Johannes Gutenberg-Universität in Mainz, Germany by *molecular beam epitaxy*. [Jourdan *et al.*, 1999; Huth *et al.*, 1993]

Foto	Name in this work	dimensions	First used in this work
	Nb-STO 0.01%	5 x 5 x 1 mm	29.11.17
	Nb-STO 0.05%	5 x 5 x 1 mm later cut to 4 x 4 x 1 mm	08.12.17
	Nb-STO 0.05% (Strip-1)	5 x 1 x 1 mm	09.04.18
	Nb-STO 0.05% (Strip-2)	4 x 1 x 1 mm	22.08.18
	Nb-STO 0.35%	5 x 5 x 1 mm	17.07.18
	UPd_2Al_3	3 x 3 x 0.9 mm	25.01.18
	Cu(100)	5 x 5 x 0.59 mm later cut to 4 x 4 x 0.59 mm	20.04.18
	Cu (Strip1)	5 x 1 x 0.59 mm	21.06.18
	Cu (Strip2)	4 x 0.29 x 0.2 mm	23.07.18
	Cu (Strip3)	4 x 0.16 x 0.16 mm	01.08.18

■ **Table 3.1: Used samples within this thesis.** All Nb-STO 0.05% samples and all copper samples are cut from the same single crystal, respectively. The UPd_2Al_3 sample is called "sample 2" in [Scheffler *et al.*, 2010]

3.5.2 Commercially bought Control Units

A variety of electronic control units was used during the thesis and is listed in [Table 3.2](#).

Type of device	Used in setup	Name	Manufacturer
Source Measure Unit	R_{DC} setup	2612B SourceMeter	Keithley
Nanovoltmeter	R_{DC} setup	2182A Nanovoltmeter	Keithley
Temperature Controller	R_{DC} setup	Model 340	LakeShore
Vector network analyzer	various	ENA Series E5071C	Agilent Technologies
Vector network analyzer	various	PNA Series E8364C	Agilent Technologies
Power Meter	various	EPM Series N1913A	Agilent Technologies
Analog Signal Generator	various	PSG Series E8257D	Agilent Technologies
Magnet Power Supply	VTI	MercuryiPS	Oxford Instruments
Temperature Controller	VTI	ITC503	Oxford Instruments
Temperature Controller	dilution refrig.	Model 370 AC	LakeShore
Level Meter	dilution refrig.	ILM200	Oxford Instruments
Magnet Power Supply	dilution refrig.	IPS120-10	Oxford Instruments
Gas Handling System	dilution refrig.	Kelvinox IGH	Oxford Instruments

■ [Table 3.2](#): Used control units during this thesis.

3.5.3 Microwave Waveguides

Within the work of this thesis several microwave chips were used for measuring all different samples and are listed in [Table 3.3](#).

Name in this work	Name on Chip	First used in this work	Conductor material	gap [μm]	s [μm]	w [μm]
CoP-01	MR 10 30	29.11.17	copper	30	200	84
CoP-02	MR 3 20	30.11.17	copper	20	60	25
CoP-03	MR Straight 4	05.12.17	gold			
CoP-04	R01-1.475	-	YBCO	80	60	25
CoP-05	R01-1.475	-	YBCO	60	40	16.67
CoP-06	R01-1.0	-	YBCO	70	40	16.67
CoP-07	7.5GHz	26.03.18	gold on chromium	30	20	08
CoP-08	4,080	27.03.18	copper			
CoP-09	10GHz	-	gold on chromium	30	20	08
CoP-10	R01-1.475	27.04.18	YBCO	85	60	25
CoP-11	RES 4	14.08.18	YBCO	60	60	25
Strip-01	-	17.07.18	Pb	80	60	-
CoP-Trans-01	-	05.12.17	copper	-		
CoP-Trans-02	TL3 S60 W25	07.12.17	copper	-	60	25
CoP-Trans-03	TL1 S100 W42	08.12.17	copper	-	100	42
CoP-Trans-04	TL1 S60 W25	-	copper	-	60	25
CoP-Trans-05	-	26.03.18	copper	-		
Strip-Trans-01	Cu H04 1450nm	20.12.17	copper	-		
Strip-Trans-02	Cu H04 1450nm	-	copper	-		
Strip-Trans-03	Cu H03 1450nm	14.03.18	copper	-		
Strip-Trans-04	Au H03 330nm	04.04.18	gold	-		

■ **Table 3.3: Used chips in this thesis.** CoP stands for coplanar resonator, whereas Strip means stripline. Trans implies a transmissionline instead of a resonator. The s and w values stand for the width of the center conductor and the distance from the inner to the outer conductor as explained in [Figure 3.2](#).

Experiments and Analysis

In this section the experimental work of this thesis is outlined, whereas all theoretical arrangements including simulations of the microwave waveguides and calculations of the theoretical predictions and complications of cyclotron resonance are presented in section 2.

Foremost, measurements of both the Nb-STO samples and the Cu sample are shown, which give an idea of the sample qualities and the orientation.

Afterwards, some broadband and resonant attempts to detect a cyclotron resonance signal are pointed out, which allow a direct determination of the effective electron masses within the band structure.

In the end, spectroscopic measurements are performed on Nb-STO, yielding not only a ratio of both effective electron masses, but also give rise to an explanation of two different *critical fields* and a variety of other interesting quantities, such as the *coherence lengths*, the *Fermi velocities* and the *superfluid density*. Finally it is possible to get a dispersion relation by calculating the *Fermi energy* and the *Fermi wave vector*.

4.1 Preparation Experiments

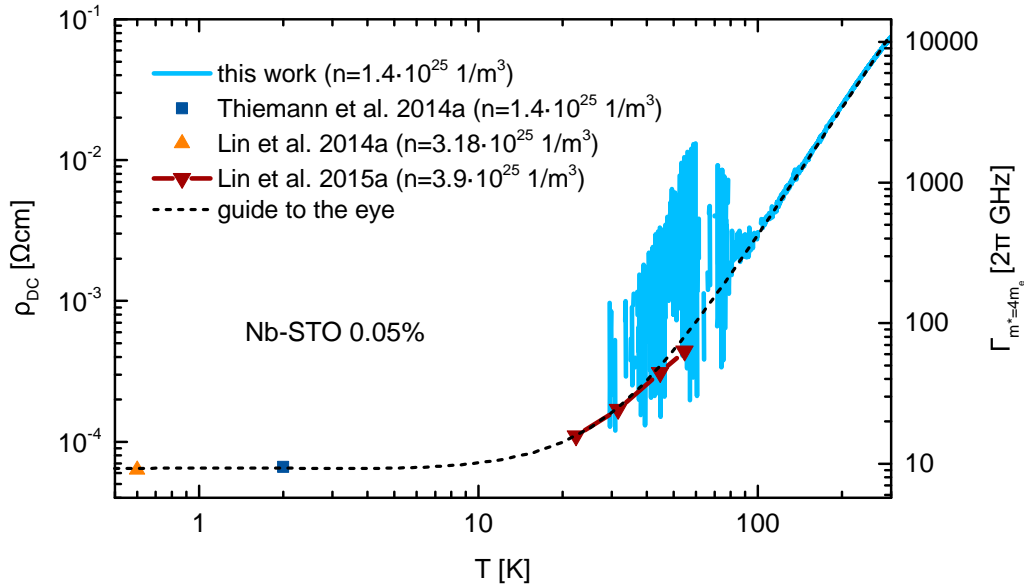
The theory part of cyclotron resonance 2.4.2 - especially [Figure 2.8](#) and [Figure 2.9](#) - give an idea of the utmost importance for the scattering rate $\Gamma = \frac{1}{\tau}$ within cyclotron resonance measurements of any kind. However, this quantity is experimentally difficult to access directly. [Dressel and Scheffler, 2006] Hence, the method of this thesis was to measure the DC resistivity σ_{DC} with a *four-terminal sensing measurement* and by applying the basic theory of *free electron gas* [Drude, 1900] it is possible to gain access to the scattering rate by using

$$\sigma_{\text{DC}} = \frac{ne^2\tau}{m^*} \quad (4.1)$$

with the *charge carrier density* n and the effective electron mass m^* .

However, this method also has weak points: the charge carrier density has to be known for the calculation and also the effective mass needs to be estimated, although this is the quantity of interest, which is measured at the end via cyclotron resonance.

However, and mostly because of already heaving a rough estimate of the effective masses of all samples, this was the measurement of choice to determine the scattering rate.

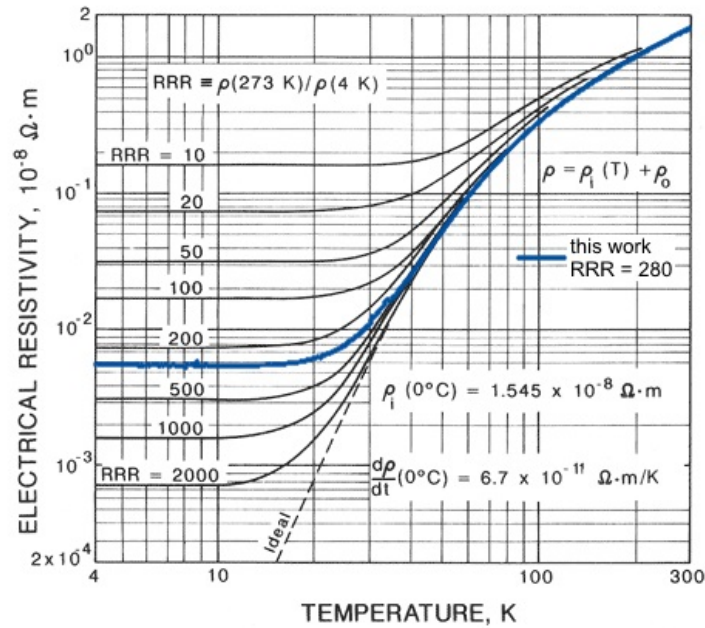


■ **Figure 4.1: DC resistivity and scattering rate of Nb-STO 0.05%.** The data of this work was obtained by a four-terminal sensing DC measurement, as well as the data from [Lin *et al.*, 2014a] and [Lin *et al.*, 2015a], whereas the data of [Thiemann *et al.*, 2018] was probed by transport measurements. Below 90 K the resistance of the contacts increases by several order in magnitude making it impossible to get reliable data by only using conductive silver as contacts.
[Nb-STO 0.05% (Strip-1); 17.04.2018]

4.1.1 Nb doped STO

To obtain the scattering rate of the Nb-STO, Figure 4.1 shows the trend of the DC resistivity of the 0.05% doped STO sample in light blue. The charge carrier density has been taken from [Thiemann *et al.*, 2018] and the effective electron mass from [Lin *et al.*, 2014a]. Unfortunately at around 90 K the contacts of both the current and the voltage connections get a rather high resistance of several ten thousands Ohms. It is assumed that this might be due to a *Schottky barrier* as it is known for metal-semiconductor interfaces, since the cables are made of gold and STO itself is a semiconductor. A junction of this kind is produced at both sides of the sample, giving it a diode effect in both directions and hence a high resistance. This border makes it impossible to determine any reliable resistivity with *conductive silver* as contacts below this temperature, as seen in the huge deviations. Nevertheless, the calculated and extrapolated scattering rate is in rather good alignment with other measurements, both with DC measurements [Lin *et al.*, 2014a, 2015b] and with transport measurements [Thiemann *et al.*, 2018] for comparable doping levels.

In the latter, the scattering rate is discussed in detail and hence, their values of 6.14 GHz and 9.46 GHz are assumed for cryogenic temperatures for the 0.01% and 0.05% doped samples, respectively. These are frequencies that can be exceeded with a 50 GHz network analyzer, but do not offer a really high value for $\omega\tau$.



■ **Figure 4.2: Comparison of DC resistivity.** The plot with its data is taken from the Copper Development Association. [Thompson *et al.*, 1990] The DC data of this work is inserted in blue and fits in its cryogenic resistivity and the course of the curve to a RRR of 280. [Cu (Strip2); 23.07.2018]

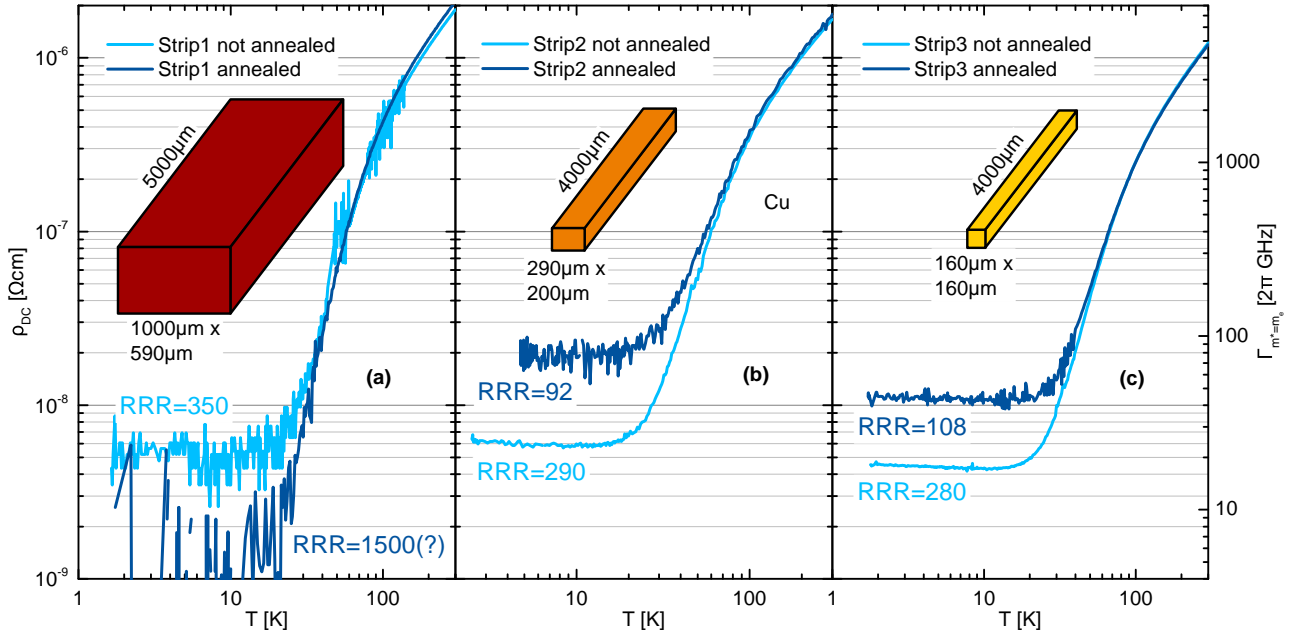
4.1.2 Copper

To gain more experience about cyclotron resonance, copper is used as a test material, since there are many publications on simple metals, especially on copper. The same type of experiment has been performed on all of the three copper strip samples. For this sample several other experimental challenges come into existence due to the low absolute resistance of a pure metal. For receiving a resolvable voltage - even with a nanovoltmeter - comparable high currents need to be applied. Otherwise the noise level of the measurement device, which lies in the order of 30 nV, is larger than the actual signal. This effect has to be in a perfect tradeoff with the minimization of the probing current to heat up the sample as little as possible. The gap in between those two effects goes to the limits of the used devices in [Table 3.2](#). For cryogenic temperatures two effects combine, making this gap even closer. Firstly, the heat effect caused by the measurement signal becomes relatively more important for low temperatures and secondly, the decreasing resistance requires even higher currents.

Furthermore, the effect of *thermo charging*, also known as *Seebeck effect*, shall be mentioned at this point. Going to low temperatures, a thermo electric charge arises, probably at the contacts of the Cu sample itself. This leads to an offset in the voltage measurement, but was taken into account by a calibration at zero current for every measured temperature.

Hence, all DC measurements on copper should be treated with caution and not being assumed as perfectly reliable, at least for the low temperature data.

Nevertheless, if one considers [Figure 4.2](#), a remarkable accordance with data from the *Copper Development Association* [Thompson *et al.*, 1990] can be observed. At around 25 K the shape of the curve



■ **Figure 4.3: DC resistivity and scattering rate of of all Cu strips.** For this calculation a charge carrier density n of $8.5 \cdot 10^{28} \frac{1}{\text{m}^3}$ and an effective mass m^* of $1 m_e$ has been used to calculate the scattering rate Γ . While all raw samples seem to scatter with a rate of around 20 GHz, the process annealing is probably not helpful to lower the latter.

[Cu (Strip1), Cu (Strip2) and Cu (Strip2); 21.06.2018, 11.07.2018, 23.07.2018, 26.07.2018, 01.08.2018 and 08.08.2018]

changes to constant line, leaving the resistivity for lower temperatures at a constant value, which is only caused by crystal defects and impurity scattering. The *residual resistance ratio* (RRR) is given by the resistivity at room temperature ρ_{RT} divided by this constant resistivity at cryogenic temperatures ρ_{cryo} .

$$\text{RRR} = \frac{\rho_{RT}}{\rho_{\text{cryo}}} \quad (4.2)$$

Whereas the ideal resistivity for a perfect, infinite single crystal is plotted as a dashed line, the probed sample has a RRR value of 280, which makes it comparable to other copper samples, as shown by the solid lines.

To get deeper insights from this measurement, the scattering rate has been calculated and is simultaneously plotted in light blue over the temperature in [Figure 4.3](#) for three different strip-shaped Cu samples. In fact, all resistivities equal each other in their courses, but diverge by a constant factor, which is justified by the not exact measurement of the dimensions of the samples. Moreover, Strip1 shows a much more noisy signal, which is founded in the larger cross sectional area, requiring an even larger probing current to compensate the larger absolute resistance of this sample. As an attempt to avoid this problem Strip2 and Strip3 are made as thin as possible.

By looking at the values of the scattering rate, it can be pinned down to around 20 GHz, which is even higher by more than a factor of 2 than the scattering rates of the Nb-STO samples and hence, leading to a value for $\omega\tau$ of 2.5 for $\omega = 50$ GHz.



Figure 4.4a: Not annealed.

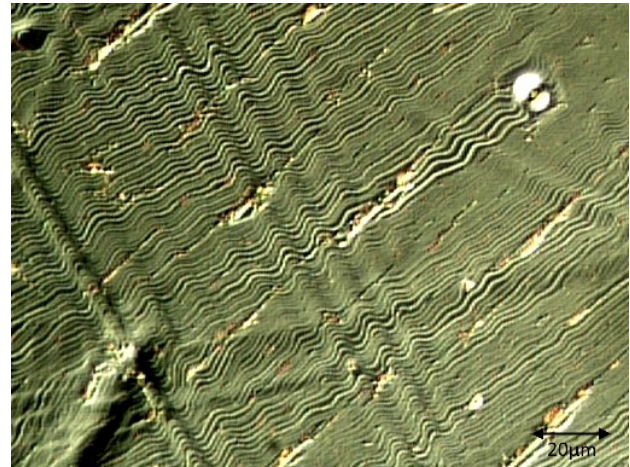


Figure 4.4b: Annealed.

■ **Figure 4.4: Microscopic pictures of raw and annealed Cu.** These pictures each show a ca. $150 \times 120 \mu\text{m}$ large picture of Strip2. On the not annealed sample a lot of grain boundaries can be detected, whereas on the annealed sample they nearly vanish, but multiple kinds of other features arise. In the top right corner of the annealed sample a crater-shaped immersion can be seen, which is due to a foreign object during the process of polishing.

[Cu (Strip2); 22.07.2018 and 25.07.2018]

An attempt to lower the scattering rate was made by annealing the sample slightly below the melting point for a certain amount of time. For all three samples 950°C was chosen as a temperature. While the middle one was four hours at this temperature, the outer ones stayed only for two hours. Ramping the temperatures up and down took again around three hours, respectively. Microscopic pictures of Strip2 can be seen in Figure 4.4 both of the raw and the annealed sample. While alleged *grain boundaries* seem to vanish during the process of annealing, other effects, such as wave patterns and wells appear. Many other features, such as the round immersion in the annealed sample in the top right corner are present all over the sample. The latter can be identified as a preparation error during polishing. [Kappler *et al.*, 1971] These crater-shaped dips form because of a foreign object on the crystal surface.

After annealing, the DC resistivity was measured again for all three samples and is shown in Figure 4.3 in dark blue. First of all, a higher noise level can be noted. Moreover, the DC resistivities at room temperature did not change, which is in accordance with the prediction of dominant scattering due to electron-phonon interactions at high temperatures.

Another striking feature is an increased resistivity for Strip2 and Strip3. This indicates an unsuccessful treatment of the copper samples since the scattering rates are even higher after annealing and the values for RRR are in the order of 100. Previous studies reported of RRR values of their samples in the order from 5000 to 20000 [Koch *et al.*, 1964; Kip *et al.*, 1961; Johnson and Rayne, 1979] and values for $\omega\tau$ of 20 to 100 [Fawcett, 1956; Häussler, 1970] for frequencies of 24 to 67 GHz. However, in Strip1 the resistivity seems to be lower after annealing, but the large cross section of this sample gives rise to a huge error bar, that can be estimated by the fluctuations of this curve.

For detecting cyclotron resonance, the signal strength needs to be large enough. The latter is approximately exponentially dependent on the value for $\omega\tau$. [Kip *et al.*, 1961] Increasing $\omega\tau$ from 2 to 10 rises the relative signal size by a factor of 26, whereas increasing to the mentioned $\omega\tau = 100$ yields even a strengthening of more than three order in magnitude.

Furthermore, a short paragraph should be said about the sensitivity of copper single crystals. According to [Kappler *et al.*, 1971] even tiny interactions, such like touching the crystal with a brush out of badger hair, cause dislocations and heavy tension. It is needless to say that such crystal defects also arise in case of *turning*, *milling*, *drilling* or *grinding*. Even *acid-string cutting* and *electro polishing* is not recommended to do, but are the most common handling methods for copper samples. [Kip *et al.*, 1961; Koch *et al.*, 1964; Häussler and Welles, 1966]

Another big issue is the fixing of the sample on the sample holder. It is recommended to not use any kind of glue, but some sort of grease instead, since a copper single crystal gets only weak defects by this method. In this work, only *vacuum grease* was used to fix the sample.

The untreated copper sample and the copper Strip1 are used for cyclotron resonance measurements, as it will be outlined in the next chapters, despite their rather low values for RRR of approximately 280 and $\omega\tau$ of around 2.

Crystal Orientation

A variety of other experimental challenges need to be taken into account for measuring cyclotron resonance. Examples therefor are an alignment of the sample surface with the external magnetic field or the roughness of the surface.

One key aspect is also the orientation of the crystal with respect to the external field, since closed electron paths are needed to gain a resonance condition.

Thus, *Laue diffraction measurements* by using X-rays have been performed in collaboration with the Max-Planck-Institut für Festkörperforschung in Stuttgart, Germany. Using this results and the Laue reflection pattern from [Figure 4.5 a](#), the sample can be orientated, which is shown in [Figure 4.5 b](#). A black point on top of the polished sample marks the edge of the (100) face towards the (110) direction.

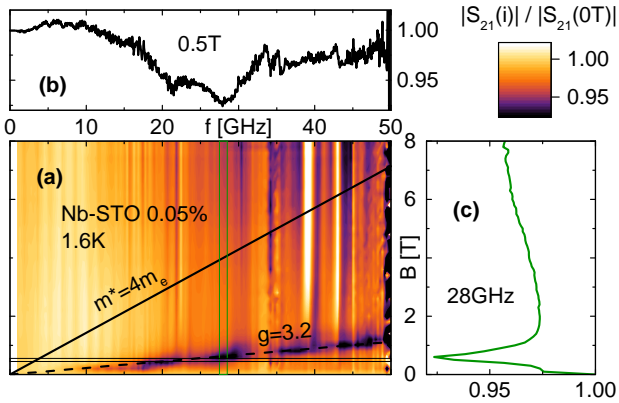


Figure 4.6 a: Spectra at 1.6K.

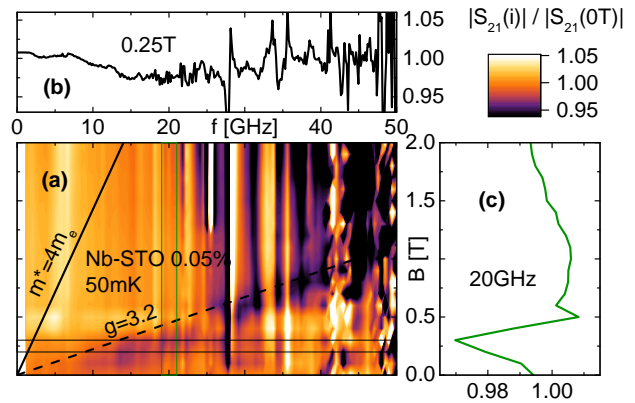


Figure 4.6 b: Spectra at 50mK.

■ **Figure 4.6: Broadband cyclotron resonance measurements on Nb-STO at different temperatures.** At both temperatures no dips are visible, where the cyclotron resonance frequency is supposed to be. However, another linear increasing dip is visible in both plots. Considering this as an EPR dip, it would have an g factor of 3.2. This line is visible on both coplanar and stripline resonators and even in both microwave setups, the bath cryostat and the dilution refrigerator. The profile plots (b) and (c) are cross sections for the horizontal, black and vertical, green lines. [Nb-STO 0.05%; Strip-Trans-03 and CoP-Trans-03; 15.03.2018 and 23.02.2018]

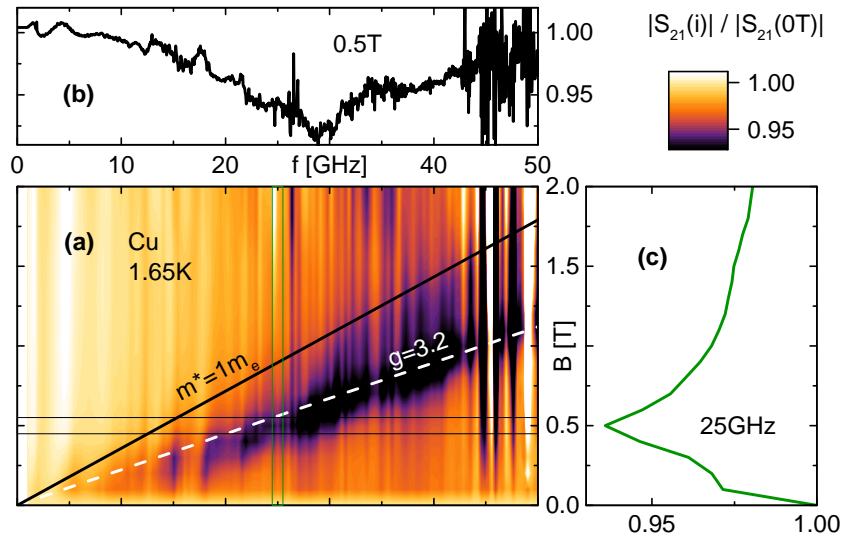
not presented here.

However, one remarkable feature is present at lower fields than the expected cyclotron signal. It is probably best seen in (c) of Figure 4.6 a. The position of the dip indicates a linear relation between its frequency and magnetic field, as it is the case for cyclotron resonance and electron paramagnetic resonance. Considering this signal as a cyclotron resonance feature it would yield an effective mass of around $0.6 m_e$, whereas EPR would reveal a g factor of 3.2. It is remarkable that this dip shaped line can be seen in both setups, the bath cryostat and the dilution refrigerator and in both coplanar and stripline waveguide designs.

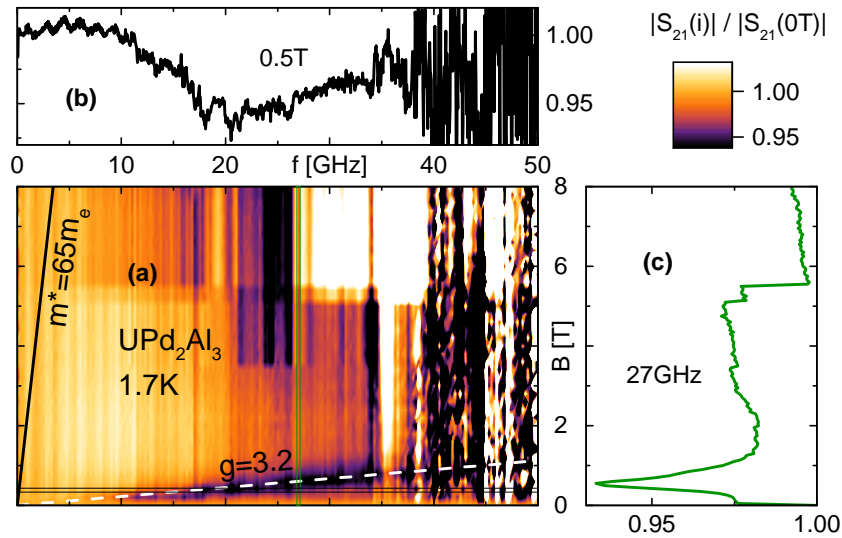
Another interesting feature is the orientation of the *meander lines* within the microwave waveguide, which can be seen in Figure 3.4. For the data obtained in Figure 4.6 a, they are perpendicular to the external magnetic field, whereas in Figure 4.6 b the orientation was parallel. Parallel meanders create a microwave magnetic field, which is perpendicular to the external static field. This arrangement is needed to excite an EPR signal, which is given with the meander line orientation at 50 mK, but in fact not with the one at 1.6 K. Despite the orthogonal meanders, the transmission line in Figure 4.6 a has an parallel part, which is at least 7 mm large, viz. the length of the inside of the box. Summarized, both designs are EPR active and a signal due to EPR cannot be excluded as reason for the additional line.

The same measurement procedure was applied to copper. Figure 4.7 shows a measurement on the raw $5 \times 5 \times 0.59$ mm large and 99.9999% pure copper single crystal as delivered ex factory, on a coplanar broadband chip. The polishing was accurate down to $0.01 \mu\text{m}$ in depth and 2° in angle according to the supplier MaTecK in Jülich, Germany. Once more, any kind of cyclotron resonance dips at the predicted resonance line for copper fail to be observed, both in the color plot as well as in the two profile plots.

However, the extra line (here marked in dashed white) is also present by using copper as a sample.



■ **Figure 4.7: Broadband cyclotron resonance measurements on copper.** The position of cyclotron resonance with an effective mass of $1 m_e$ is marked with the solid, black line. In fact, there is no feature recognizable, whereas dips for a g value of 3.2 come again into existence. [Cu(100); CoP-Trans-03; 24.04.2018]



■ **Figure 4.8: Broadband cyclotron resonance measurements on UPd_2Al_3 .** As UPd_2Al_3 is a heavy fermion material it has a comparable large effective mass of around $65 m_e$ [Inada *et al.*, 1999]. Its exact value is still under debate and is discussed in [Scheffler, 2004]. However, as in the previous broadband measurements cyclotron resonance dips are not visible, but again the alleged EPR dip. [UPd_2Al_3 ; Strip-Trans-03; 25.01.2018]

The pronounced strength of this dip can clearly be seen in the profile plots (b) and (c).

As a last sample UPd_2Al_3 has also been under discussion of a candidate for measuring cyclotron resonance due to its low scattering rate in the microwave regime. [Scheffler *et al.*, 2005, 2010, 2006, 2013]

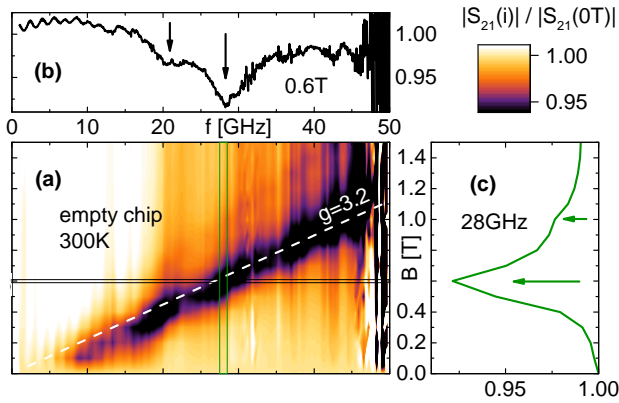


Figure 4.9a: Spectra for an empty stripline chip.

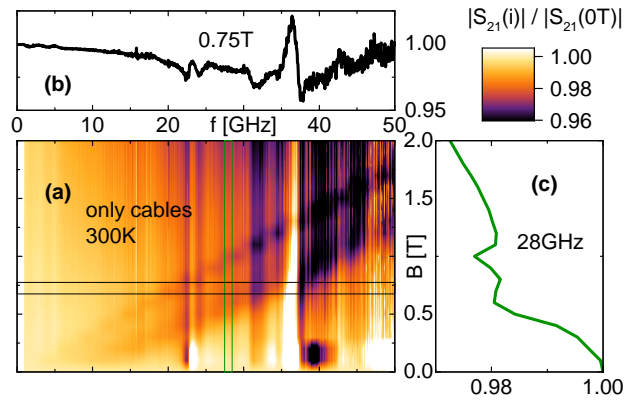


Figure 4.9b: Spectra for shorted coaxial cables.

■ Figure 4.9: Broadband transmission coefficients for an empty waveguide and and without chip.

To prove that the additional line within all broadband spectra has nothing to do with the signal from the sample, several empty waveguides are measured and the dips for a g value of 3.2 are not affected at all. Additionally the chip has been completely removed. The dips are still weakly present and also a second line is detectable above the 3.2 line.

[Strip-Trans-03; 16.03.2018 and 10.04.2018]

One remarkable difficult to handle challenge in this heavy fermion material is the large effective mass, which lies in the order of 50 to 70. [Dalichaouch *et al.*, 1992; Inada *et al.*, 1999; Geibel *et al.*, 1991] This demands extremely high magnetic fields for comparably low frequencies, which in turn comes into conflicts with the scattering rate.

However, UPd_2Al_3 possesses of several lower effective masses. [Tonegawa *et al.*, 2012, 2013] The transmission spectra of a frequency- and field-dependent sweep on a broadband stripline waveguide are plotted in Figure 4.8. As in the previous two samples, cyclotron resonance is not visible by any feature in this measurement, while the additional line on the bottom is still present. Parasitic horizontal steps in the color plot probably arise from a touching of the flexible coaxial cables during the measurement.

This sample is a 60 nm thin film sample, which might come in conflict with the scale of the cyclotron radius.

In summary it can be said that none of the three probed samples shows any evidence for cyclotron resonance in a broadband approach. This might be due to a too low signal strength, which is caused for Nb-STO and copper by to low values of $\omega\tau$ and for UPd_2Al_3 by a large effective mass requiring a too high static magnetic field.

4.2.2 Parasitic Dips

Since it is estimated to be unlikely to detect cyclotron resonance within a broadband approach, previously mentioned $g = 3.2$ dip will be the focus for the rest of this chapter. It was present in every broadband measurement, no matter if in coplanar or stripline design, perpendicular or parallel meander, Mylar foil or sapphire and independent of the sample. Therefore measurements without any sample from cryogenic temperatures up to room temperature have been performed. In Figure 4.9a

spectra, using a stripline waveguide at 300 K, are plotted. Clear distinct dips in (a) in the region of the white dashed line are unmistakable, which also are pronounced in the profile plots in (b) and (c). Moreover, it seems like this line has an offset, which is not taken into account by the guide to the eye. Since this line is also visible at room temperature, a cyclotron resonance signal from the chip itself or anywhere else is eliminated as possible origin of these dips due to the typical high scattering rates at room temperature.

As it is assumed that the signal might come from EPR, a piece of the copper waveguide was probed in a *X-band* setup at 300 K. Though, there was no signal detectable within this measurement, leaving the question of the origin of this line open.

A small note at this point shall be that exactly the same behavior of a linearly increasing line is observed in gold transmission lines for the same g factor, even though it is not that distinct as in copper.

By precisely looking above the distinct line in (a) another signal line can be detected, although this one is really weak. Plot (b) shows this dip at 20 GHz and plot (c) at 1 T.

This was also the motivation to directly connect both connectors, which normally are placed at the end of the microwave box. Transmission spectra for this arrangement are shown in [Figure 4.9 b](#). For better identifying the weak lines, all auxiliary lines are left out in this plot. Nevertheless, two parallel, linear increasing dips can be detected and show up nicely in the profile plot in (c) at 1 T and 0.6 T. The lower one corresponds to the heavy pronounced lines in all previous plots. In the other spectra only hardly visible is the upper line, which goes along with a $g = 2.0$ EPR signal.

To summarize this paragraph, it is obvious that the parasitic, linear increasing dips do not come from any contribution of the samples since the signal is there for all of the probed three samples and moreover, for empty microwave transmission lines. The main contribution to this line lies probably in the waveguide out of copper itself and almost vanishes by replacing it and shorting the coaxial cables. By doing so, another linear increasing line is revealed, which matches a $g = 2$ EPR signal.

4.3 Resonant Cyclotron Resonance Experiments

As mentioned in the summary of the last chapter, the signal strength of a possible cyclotron resonance signal is too small to be detected in a broadband sweep. Hence, a more sensitive, resonant approach will be used for further investigations. In fact, a resonant probing method does not amplify the cyclotron signal at all, but it improves the sensitivity of the measurement, which is why weaker signal strengths can be revealed, even though the sample itself was not improved.

To detect a cyclotron resonance signal, one should know that applying the resonance magnetic field maximizes the microwave absorption in the sample and hence, minimizes the transmission at the resonant mode. This, however, broadens the mode and increases the FWHM $2f_B$, which can be detected as a peak in f_B as a function of magnetic field.

4.3.1 Copper

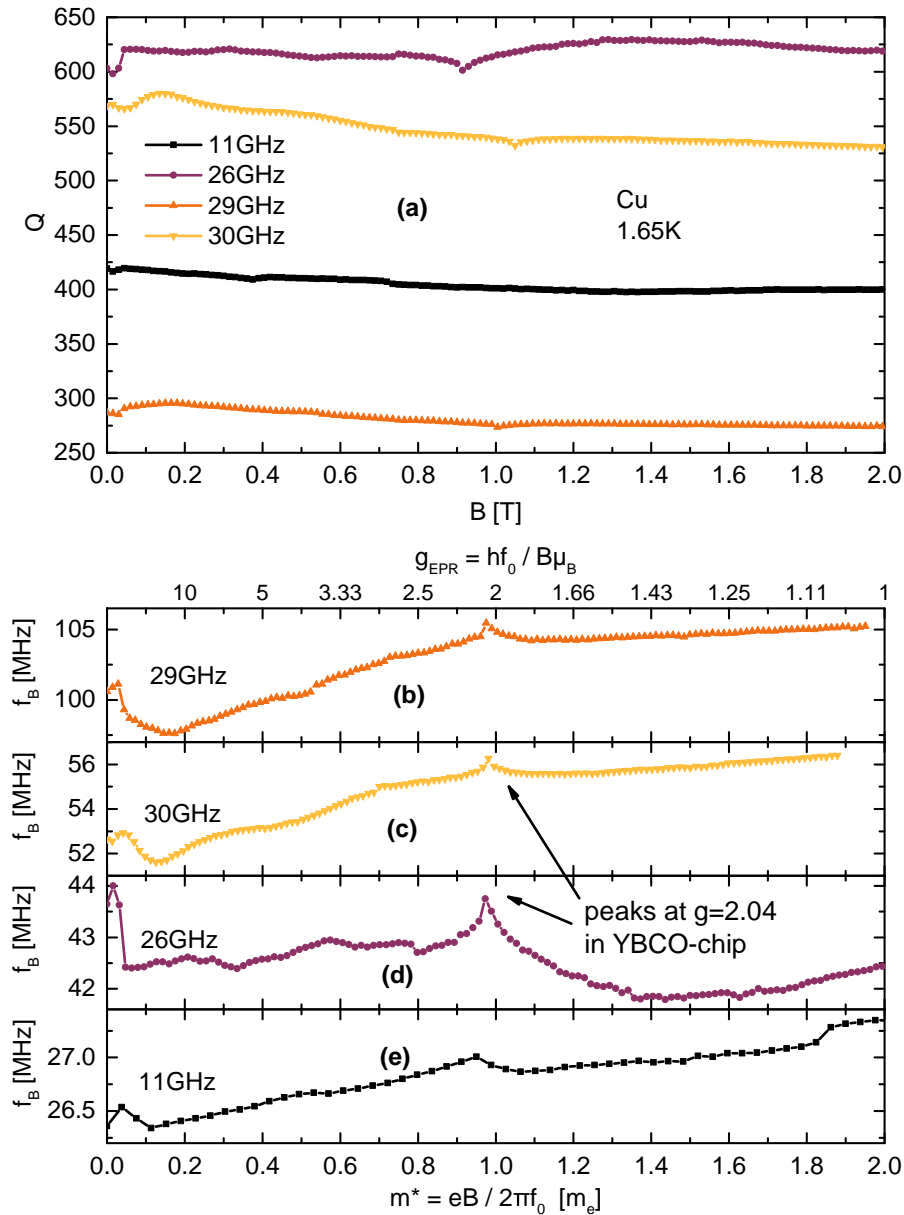
Data of the the already cut $4 \times 4 \times 0.59$ mm large copper single crystal, which were measured on an YBCO coplanar resonator with a fundamental resonance frequency of around 1 GHz are shown in [Figure 4.10](#). In (a) the quality factors $Q = \frac{f_0}{f_B}$ of four different resonance modes are plotted over the magnetic field. In the plots below the bandwidths f_B are given as a function of the magnetic field over the resonance frequency $\frac{B}{f_0}$ with a prefactor of $\frac{e}{2\pi}$, such that the x-axis basically represents the effective mass as a variable parameter. Simultaneously, the g factor of a possible EPR signal is marked as a variable on the top grid. One should note that the bandwidth does not actually depend on the effective mass or the g factor. These two quantities are just an auxiliary variable to quickly get the message of the plot.

Since all four modes are normalized to their resonance frequencies in the lower plots, they can differ in the absolute value of f_B , but should all yield the same trends, which is mostly the case for all presented modes.

Effective masses from cyclotron resonance in copper is expected to be in the range of $1.25 m_e$ to $1.40 m_e$ [Kip *et al.*, 1961; Häussler and Welles, 1966; Koch *et al.*, 1964] for belly orbits depending on the orientation relative to the magnetic field. Due to multiple, theoretical subharmonic resonances the cyclotron peak in f_B should be rather broad. Such a feature is not observed for copper, neither in this measurement nor in any other configuration within this thesis, such as different resonator materials or *small angle tipping* [Koch *et al.*, 1964] relative to the static magnetic field.

Another approach to gain data out of this kind of measurements is a *Fourier Transformation* of $Q(\frac{1}{B})$ since a theoretical predicted Q has equidistant dips due to its $\frac{1}{B}$ -periodicity in equation (2.28). This Fourier Transformation \mathcal{F} depends on the reciprocal value of $\frac{1}{B}$, i.e. on B itself, and has a pronounced peak at the resonance magnetic field B_c . This method of evaluation is introduced and enhanced in its functionality within this work for the theoretical predictions in section 2.4.2. However, this Fourier method failed to spot any signal in the experimental data as well.

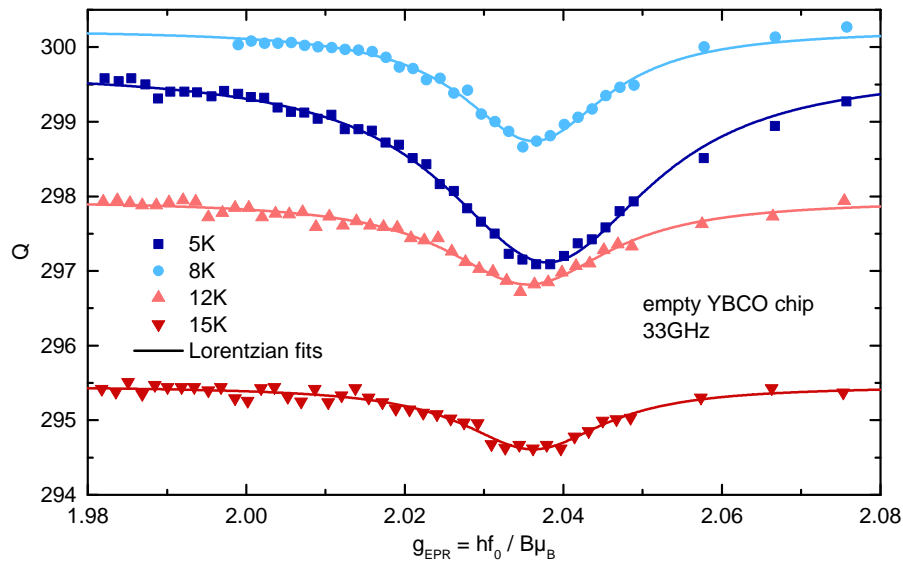
Besides, a rather distinct feature in [Figure 4.10](#) throughout every mode is an absorption dip at a g factor of around 2.04, which is also seen in all other measurements on a YBCO waveguide. Its origin is YBCO itself and will be discussed in the following chapter.



■ **Figure 4.10: Resonant cyclotron resonance measurements on copper.** The bandwidths and quality factors of four different modes are plotted over the magnetic field. In (a) the field-dependent raw data is shown. The x-axis of the lower plots have prefactors in a way that it directly represents the effective electron mass as a variable, which should not be understood as the physical property of the material. Simultaneously on top of the grid the g factor for EPR measurements is marked in the same way, except it is reciprocally dependent on B . The magnetic field for this plot was along the [110]-direction. A cyclotron resonance signal can actually not be revealed, however, EPR peaks are visible at a g factor of 2.04. [Cu (100); CoP-10; 27.04.2018]

4.3.2 Parasitic Dips

As the same absorption peaks arise in every measurement on YBCO chips, these waveguides are probed without any sample. The quality factor Q of this measurement can be seen for different temperatures



■ **Figure 4.11: EPR investigation on empty complanar YBCO resonator.** In this plot a narrow range of the spectrum of the quality factor is plotted over the variable g factor for different temperatures. Weak, but resolvable dips are distributed around a g factor of 2.037 and reduce in size for an increasing temperature. It shall be said that the magnetic field for this plot is taken from the magnet power supply without any correction, which could contain error in the order of a few percent. [CoP-10; 04.05.2018]

in Figure 4.11 as a function of the g factor, which is again used as a variable in this context and basically the inverse of the magnetic field. All temperatures show the same peak, which gets weaker for higher temperatures. By fitting the dips with a Lorentzian shape the g factor can be pinned down to 2.037 as a mean value for the distribution of all resonance dips. It is worth saying that for this plot - and for all other plots in this thesis - the actual magnetic field at the sample is considered as displayed field of the *magnet power supply*, which is probably off by a few percent. Hence, all deduced quantities of the field - especially the mentioned g factor - should be seen with an corresponding error bar.

It is, in fact, not the first time that these kind of resonances have been seen in YBCO. Also other groups have reported about them and claim this to be an EPR resonance at $g = 2.05 \pm 0.02$ in the $3d^9$ orbitals of Cu^{2+} ions in YBCO located in the superconducting phase. [Rettori *et al.*, 1987; Mehran *et al.*, 1987] The precise origin of these EPR-shaped dips is controversially discussed a lot among literature [Vier *et al.*, 1987; Bowden *et al.*, 1987] until the cause of the resonances was attributed to residual copper compounds, which are present in every YBCO sample in the per mill range, even in samples of highest purity. [de Mesquita *et al.*, 1989]

Thus, the observed absorption dips can be explained by an ESR signature of the probing microwave waveguide itself and are actually not caused by the probed sample.

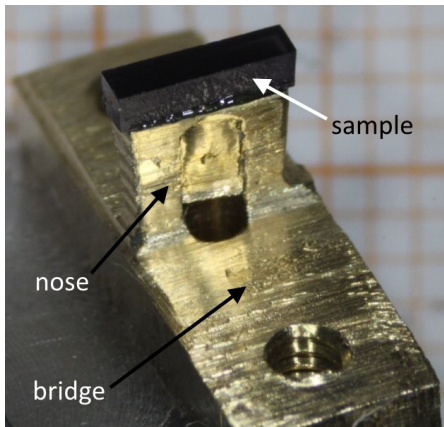


Figure 4.12 a: Sample on the bridge out of brass with vacuum grease as fixing layer in between.

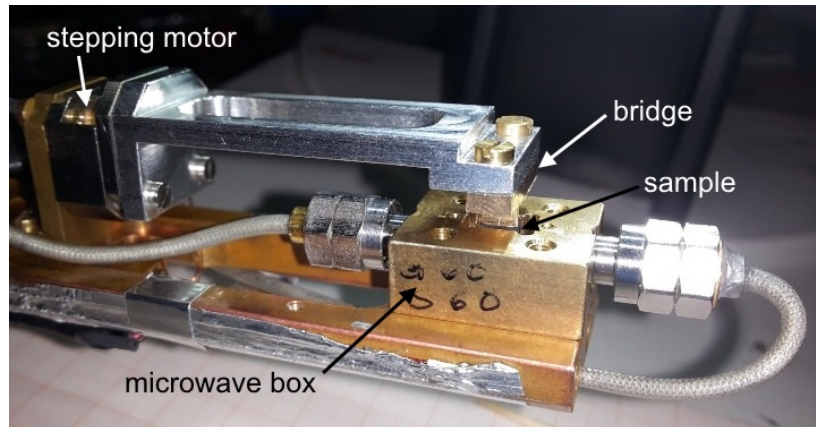


Figure 4.12 b: Positioner with the stepping motor on the left and the bridge extending the sample into the microwave box directly over the coplanar waveguide.

■ **Figure 4.12: Sample and positioner.** By using the stepping motor the distance between the sample surface and the waveguide can be adjusted in the micrometer range.

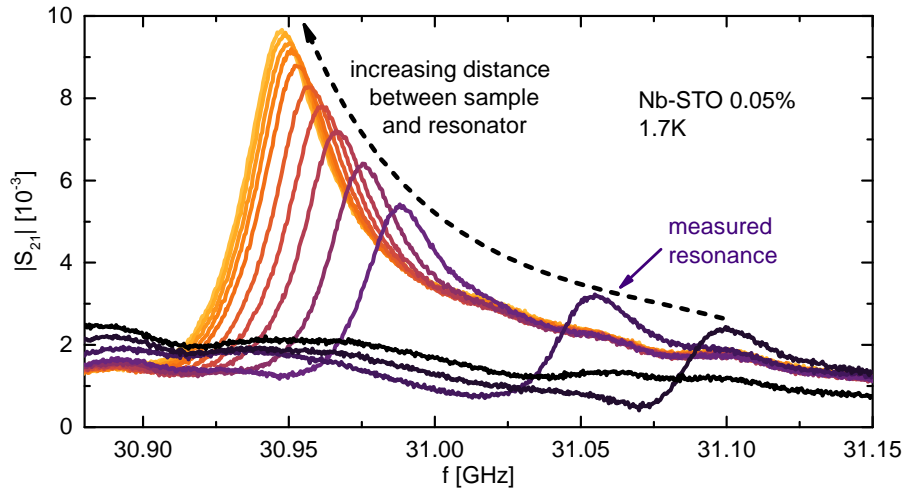
4.3.3 Nb doped STO

For resonant measurements there is always one critical aspect, viz. the distance between the sample and the resonant waveguide itself. Putting the sample too far away decreases the influence of the sample on the probing signal and hence, since the sample is no more a component of the measurement signal. A too short distance, however, damps the probing signal so much that the resonant mode might be gone and a measurement cannot be performed at all. This is especially the case for good conducting and hence, damping materials, such as they were used in this work. Therefore a resonant measurement of this kind is always a tradeoff between not destroying the mode and a sufficient large influence of the sample on the measurement signal. Within this work the ideal compromise has been considered to suppress the mode as much as possible, but it should be clearly identifiable as such.

In the beginning of this work pieces of sapphire of several thicknesses, or Mylar foils are used. However, setting the distance with such a static method goes along with several disadvantages. Firstly, it takes quite a long time, to check if the resonant mode is suppressed or not influenced at all by the sample since the whole setup needs to be cooled and warmed up again for a variation in distance. Secondly for every cooldown the background signal is different, making it hard to compare several measurements and hence, several tried distances. In other words, the direct influence of varying the distance from the sample to the waveguide by this method is experimentally challenging.

Thus, in the end of this thesis a positioner as shown in [Figure 4.12](#) has been used. In [Figure 4.12 a](#) a golden colored bridge out of brass is displayed. The upper surface is filed down, leaving a nose on top, where the sample (black) is placed on to. It sticks there due to the vacuum grease, even when turning the whole gadget by 180 degrees. As seen in [Figure 4.12 b](#), the bridge is then attached to a stainless steel bar, which is mounted on a stepping motor. The latter is able to control the height of the bridge including the sample and hence, regulate the distance between the sample and the waveguide.

Using such a device allows an in situ adjustment of the sample height and its impact on the quality of the mode can directly be observed on the network analyzer. A variation of this kind is performed for Nb-STO 0.05% and its effect on the modification of the resonance plotted in [Figure 4.13](#). Rather



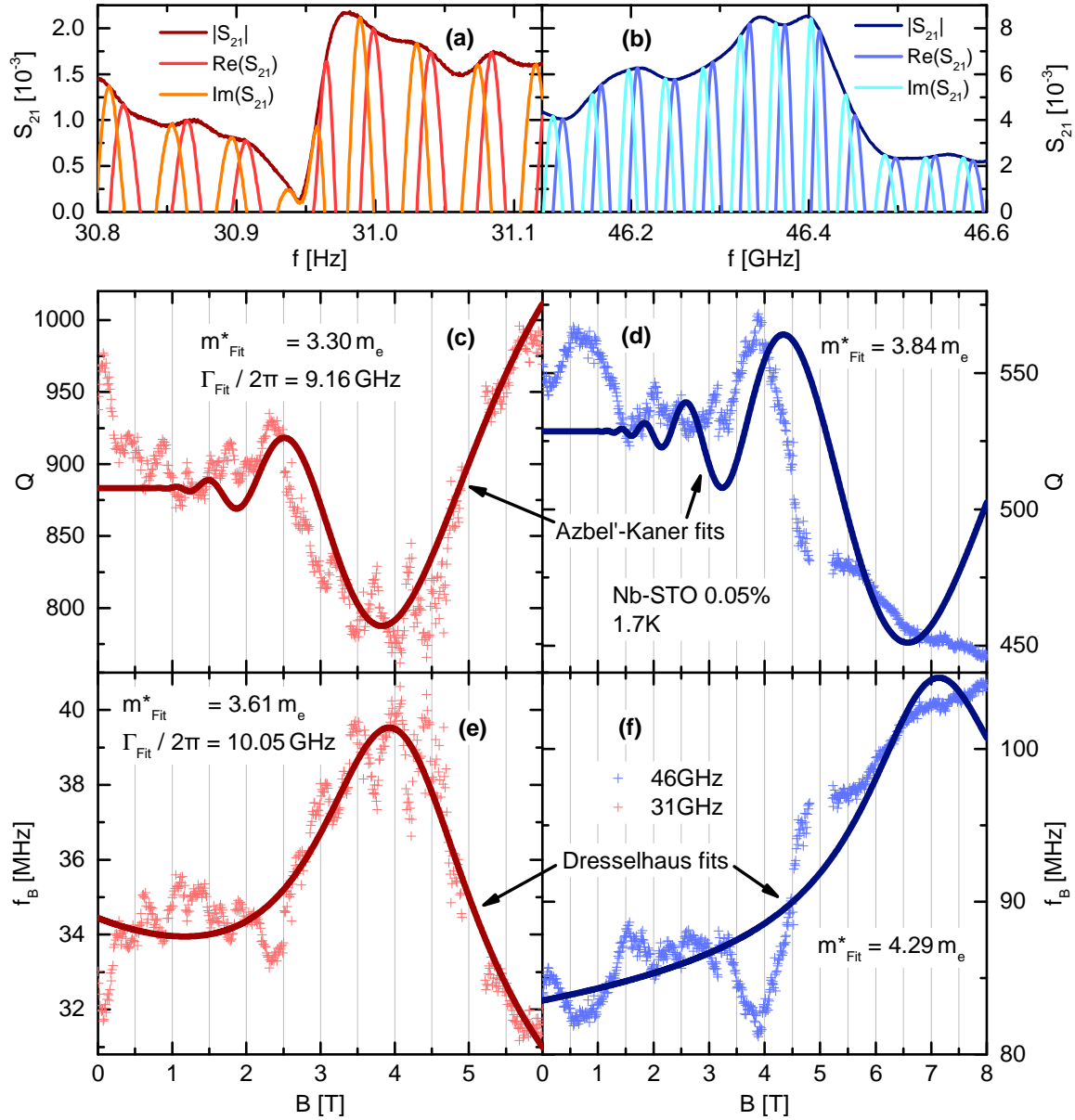
■ **Figure 4.13: Mode suppressing due to increasing distance between sample and waveguide.** Several spectra are plotted with the distance as parameter, while from yellow to black the distance was reduced linearly. The final measurement configuration for cyclotron resonance is marked. [Nb-STO 0.05% (Strip-2); CoP-11; 22.08.2018]

undisturbed modes can be seen in yellow on the left side. The quality factor of such a mode is comparably high, but the sample is actually not part of the measurement in the first place. By lowering the sample towards the waveguide, the mode gets exponentially more damped, which is coincident with the theoretical approach of *conformal mapping* of coplanar waveguides [Ghione and Naldi, 1987; Gevorgian *et al.*, 1995]. This results in a smaller quality factor, making the probing signal less sensitive. However, only for the partially suppressed modes, the sample gains influence on the signal. The picked setting for the cyclotron measurement is marked with a purple arrow and lies on the damped end of the measurement series.

Using these preferences a cyclotron resonance measurement at 1.7 K was performed for two individual modes at 31 GHz (second harmonic resonance) and 46.5 GHz (third harmonic) on a YBCO resonator with a fundamental mode of around 15.5 GHz. As it can be seen in subplot (a) of [Figure 4.14](#) the resonance at zero-field is damped, but still distinguishable from the background signal. This is not as clearly the case for the third harmonic in blue in subplot (b). Hence, this mode is probably not as reliable as the second harmonic in red.

Subplots (c) to (f) show the results in Q and f_B of the field sweep for the two probed modes. By looking at them one can detect a lot of fluctuating and oscillation noise features. Some of them might be caused by a broad resonance in (a), which is even broader than the oscillation period of the background. This makes it hard to approximate the background with a first order Taylor polynomial. Furthermore, it should be mentioned that a few datapoints around 5 T have been removed from all plots due to their unproportional large deviation to the rest of the measurement. This error might be caused by a touching of the cables or a slight movement of the network analyzer.

Nevertheless, a rather large peak of nearly 15% in height at around 4 T can be observed in $f_B(B)$ of the red 31 GHz mode, resulting in a comparably strong dip in $Q(B)$. Considering this feature as a cyclotron resonance signal, the skin depth and the cyclotron radius need to be figured out to decide about the correct way of fitting, either multiple or single dip. While the skin depth is given by several micrometers via equation (2.9), the cyclotron radius from equation (2.25) is in the order of several



■ **Figure 4.14: Resonant cyclotron resonance measurements on Nb-STO 0.05%.** Datapoints around 5 T have been excluded for both modes due to a large deviation, which was probably caused by a mechanical touching of the cables or any other movement of the setup, for instance the network analyzer. (a) and (b) show zero-field spectra. While the second harmonic (red) of the coplanar YBCO chip with a fundamental mode of 15.5 GHz shows a distinct resonance, the third harmonic (blue) is not a sharp mode. (c) to (f) show measurement results for a magnetic field sweep with pronounced features looking as a cyclotron resonance signal. Both approaches for good and bad conducting materials have been applied and fitted here since Nb-STO is in between those two limits due to its low charge carrier density.

[Nb-STO 0.05% (Strip-2); CoP-11; 22.08.2018]

hundreds of nanometers by using Fermi velocities from the following chapter. Since the ratio between those two is not clear enough to be in one or the other regime, both theoretical approaches have been fitted to the experimental data.

While f_B represents a measure of the absorption due to equation (3.4), Q is the reciprocal value of it since f_0 is commonly rather constant throughout a measurement. Hence, the single peak, which is given in terms of absorption, is fitted to the bandwidth. The multiple dip signal is given in terms of surface impedance. By hand-waving arguments a dip in the surface impedance means a peak in the conductivity and hence, a large absorption and bandwidth and consequently, a dip in Q . This is why the multi-dip resonances are fitted to the quality factor. Therefore, the experimental fit-version of the theoretical predictions in the equations (2.28) and (2.29) are

$$Q = A \cdot \left(\sqrt[6]{e^{-\frac{4\pi^2\Gamma m^*}{eB}} \sin^2\left(\frac{4\pi^2 f m^*}{eB}\right) + \left(1 - e^{-\frac{2\pi\Gamma m^*}{eB}} \cos\left(\frac{4\pi^2 f m^*}{eB}\right)\right)^2} - 1 \right) + Q_0 \quad (4.3)$$

with the fit parameters A , Γ , m^* and Q_0 for the multi dip and

$$f_B = A \cdot \left(\frac{1 + \left(\frac{2\pi f}{\Gamma}\right)^2 + \left(\frac{eB}{m^*\Gamma}\right)^2}{\left(1 - \left(\frac{2\pi f}{\Gamma}\right)^2 + \left(\frac{eB}{m^*\Gamma}\right)^2\right)^2 + 4\left(\frac{2\pi f}{\Gamma}\right)^2} - \frac{1}{1 + \left(\frac{2\pi f}{\Gamma}\right)^2} \right) + f_{B,0} + c \cdot B \quad (4.4)$$

with the fit parameters A , Γ , m^* , $f_{B,0}$ and c for the single peak. In both cases A is the amplitude of the cyclotron signal followed by the actual signal shape itself, Γ the scattering rate, m^* the effective electron mass and Q_0 , $f_{B,0}$ and c are fit parameters for a zeroth and first order Taylor approximation for the background, respectively.

By applying the fits to the 31 GHz mode, one can observe a rather appropriate accordance of the experimental data to the theoretical fit function in both the single and multiple resonance case. The fitted electron masses are $3.30 m_e$ and $3.61 m_e$, being slightly below the ones recently reported for the upper band of Nb-STO [Lin *et al.*, 2014a]. However, the scattering rates with 9.16 GHz and 10.05 GHz match the 9.46 GHz of Table 2.1 with a remarkable accuracy.

For the 46 GHz mode the effective masses are more in the range of literature data, but since the experimental data has lots of fluctuations and does not follow the fit smoothly, the reliability of this mode is doubtful. Moreover, scattering rates for fits of this mode were fixed because of too much background signal, which drives the fit to scattering rates of one order in magnitude higher.

In the end, the physical nature of the signal is questionable, especially because such a measurement could not be reproduced after warming up the setup and remounting the sample. At least a temperature fluctuation can be excluded as a reason for the signal since temperature stayed constant within a range of 9 mK during the occurrence of the dip. With respect to an absolute value of 1.7 K this is in the order of half a percent in precision.

4.4 Experiments on Superconducting Nb-STO

Beyond cyclotron resonance measurements, experiments on superconductive Nb-STO has been performed. Since cyclotron resonance measurements do not reveal a clear and reproducible signal, another way of investigating the effective electron mass in Nb doped STO. In a nutshell, while increasing the magnetic field superconductivity breaks down at a certain magnetic field B_{c2} . As Nb-STO is a type II superconductor it lets the magnetic field penetrate in single flux quanta within vortices in the *Abrikosov lattice*. Their dimension is the *coherence length*, which is related to the Fermi velocity of the electrons. By knowing the Fermi level the effective mass can be worked out in principle.

Since the Fermi energy is not directly measured within this work and still under debate among theoretical and experimental literature, one is at least able to compute the ratio of both present electron masses. Moreover, the field dependent measurement of the complex conductivity reveals a wide range of other interesting quantities, such as the *mean free path* and the *superfluid density*. On top of that, an alternative explanation for the decrease of the conductivity via two kinks can be given.

All experiments within this section have been performed in the dilution refrigerator using a superconducting stripline resonator with meander lines being parallel to the magnetic field. This arrangement is responsible for the nonappearance of any contributions of the vortex dynamics on the complex conductivity due to a vanishing Lorentz force acting on the vortices. Consequently, the main contribution to the measurement signal comes from the superfluid condensate. This will be important for the interpretation of the results.

4.4.1 Process of Measuring

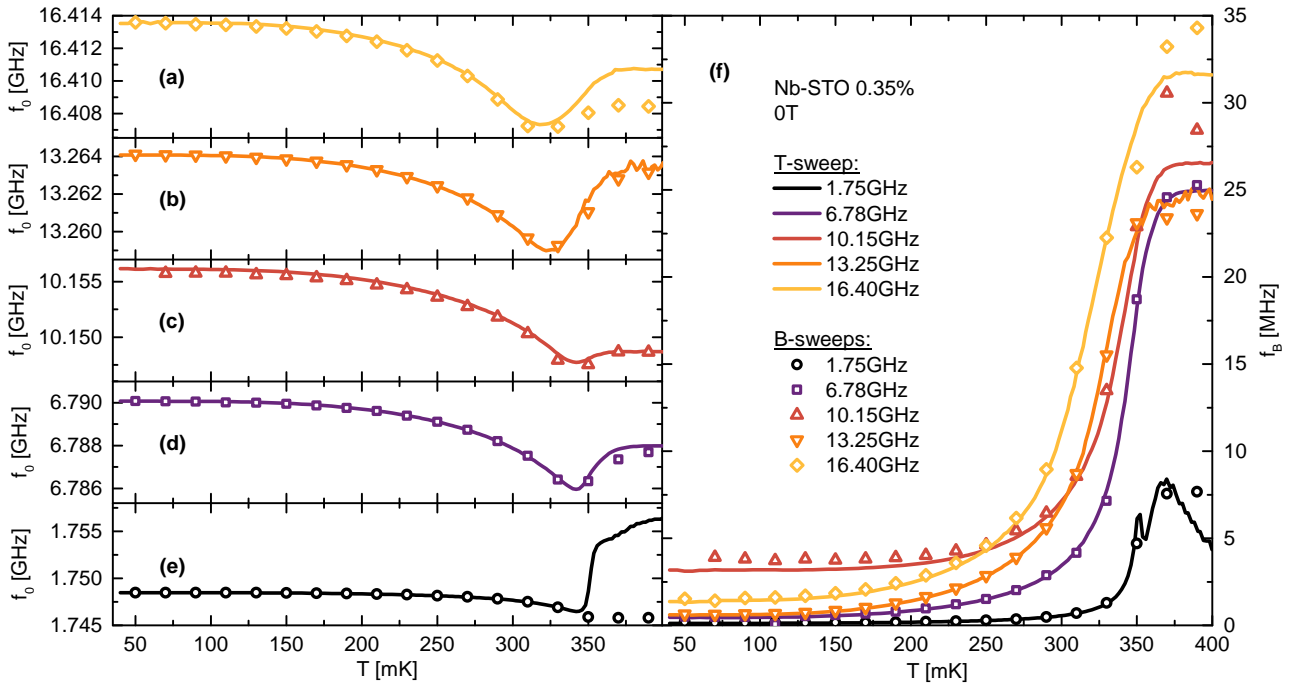
For Nb-STO of the doping level of 0.35% the complex conductivity shall be measured temperature- and field-dependent. Therefore, the sample is placed on a resonant stripline microwave waveguide with a fundamental mode of 1.75 GHz and the resonance frequencies and bandwidths of several modes are recorded.

This is performed in two similar experiments. The first one are field sweeps for constant temperatures. In this case the sample is cooled down in zero field and afterwards the magnetic field sweeps are executed. These go up to 65 mT, which is at the limit of the critical field of the lead resonator [Ebensperger *et al.*, 2016]. To not suffer of any hysteresis effects of the sample it is warmed up after each field sweep above its critical temperature.

The other type of experiment are temperature sweeps for fixed magnetic fields. The sample was cooled in zero field and a temperature sweep up to T_c was performed. Afterwards the sample is cooled in zero field again. A certain field is applied and the next temperature sweep is started.

The resonance frequencies and bandwidths of both experiments can be seen in [Figure 4.15](#) for five modes as a function of temperature. Temperature sweeps in zero-field are plotted in solid lines and match all measurement points at 0 T for all field sweeps, plotted in open symbols. For the lowest and highest mode the bandwidth are not in accordance, which is ascribed to fitting errors due to the low visibility of the resonance in the non superconducting state.

As seen in the inset (b) of [Figure 4.16](#) for field sweeps all modes possess an increasing bandwidth, which is the expected behavior due to an increasing number of vortices within the *Shubnikov phase*. Under a closer look, it can be noticed that all bandwidths do not increase smoothly, but have two certain kinks, which are for all modes at the same magnetic fields and are marked in black in (a). As already said in

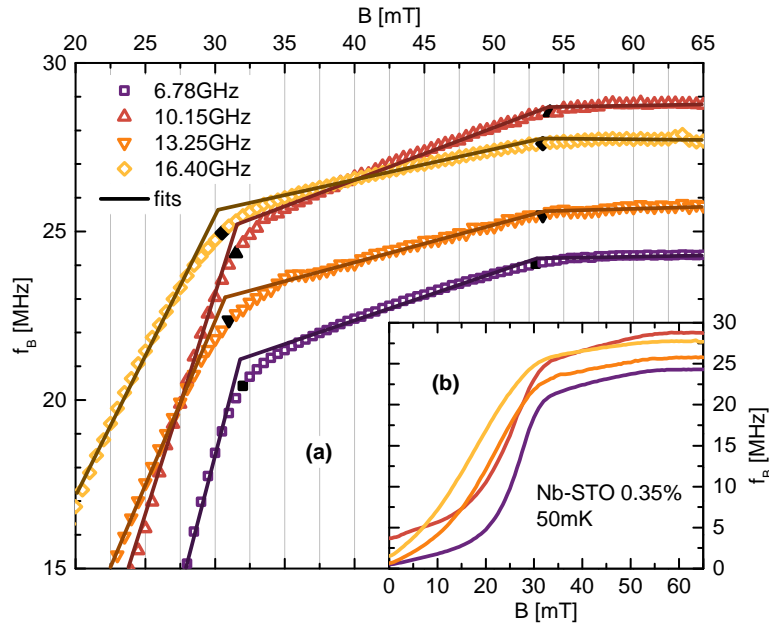


■ **Figure 4.15: Temperature-dependent measurement of resonance frequency and bandwidth.** Within this plot the temperature sweeps are compared to the field sweeps. Solid lines contribute each to one measurement in zero field, whereas open symbols are the datapoints at 0T for different measurements within field sweeps for different temperatures. Both f_0 and f_B match each other nicely, indicating an absence of any hysteresis effects. For the highest and lowest mode a deviation can be observed, but this can be attributed to fitting problems due to a hardly recognizable resonance. [Nb-STO 0.35%; Strip-01; 31.07.2018 and 06.-10.08.2018]

the introduction of this chapter only the superfluid itself has an influence on the response function and hence, these two kinks can be attributed to two exceptional magnetic field within the superconductor, which will be discussed later in the text. The exact position of the kinks is determined by fitting the three segments individually and considering their intersections as is it shown for four modes in (a).

4.4.2 Complex Conductivity and Interpretation of Kinks

As described in the chapters 3.3 and 3.4 the complex conductivity can be worked out from the measured resonance frequency and bandwidth. The temperature for the R_S - X_S matching is set to be the highest measured temperature, viz. 390 mK, which is just high enough to escape the superconducting phase. The resulting imaginary parts of the complex optical conductivity σ_2 is plotted over the applied magnetic field in [Figure 4.17](#). First of all, it should be said that the shapes of all frequency-dependences mostly look the same and is characterized by three different regions, all having a different linear slope. The border of these segments are the two exceptional fields, which are present in the bandwidth as well. The first one might be hard to detect and is shown in detail in the inset (f) in [Figure 4.17](#). Within this zoom the three ranges become clear. The first one is separated from the second one by the first kink and the third one begins at the point, where σ_2 reaches the value 0. These kinks are also visible in the real part of the optical conductivity in [Figure 4.18](#). The first one is



■ **Figure 4.16: Kinks within the field dependent bandwidth.** As expected the bandwidth increases in the superconducting state with an increasing magnetic field as seen in (b). Taking a closer look to the data in (a) reveals two distinct kinks for every mode. These two exceptional fields are later on called B^* and B_{c2} and are marked with black symbols. The determination of these fields is done by fitting linear curves to each segment as shown by the solid lines.

[Nb-STO 0.35%; Strip-01; 06.-10.08.2018]

for most modes at the maximum value of the overshooting over σ_n and the second one is at the field, where σ_2 reached σ_n .

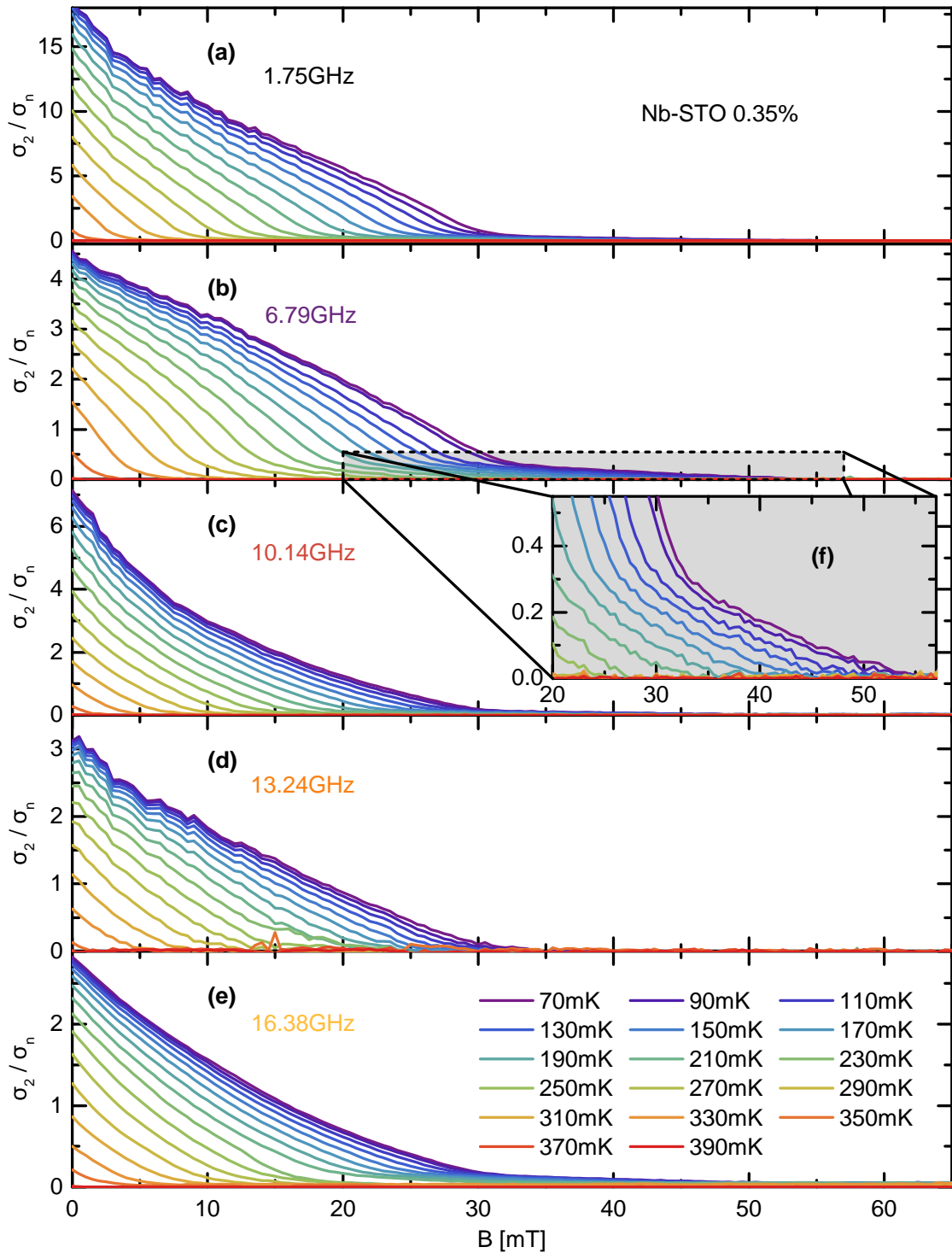
Both characteristic features in the imaginary part of the optical conductivity (the linear decreasing and the two remarkable kinks) are discussed and interpreted later in the text.

Figure 4.19 shows the fitting procedure for the 6.79 GHz mode at 70 mK. The intersection with the y-axis of both fits are in the following named $\sigma_2(0\text{ T})$ for the upper fit and σ_2^* for the lower fit. Using these conductivities it is possible to determine absolute values for the Cooper pair density within the superconducting condensate. This can be done via the *two fluid model* with the complex conductivity [Tinkham, 1996]

$$\sigma = \frac{\pi n_s e^2}{2m^*} \delta(\omega) + \frac{n_n e^2 \tau_n}{m^*} + i \frac{n_s e^2}{m^* \omega}, \quad (4.5)$$

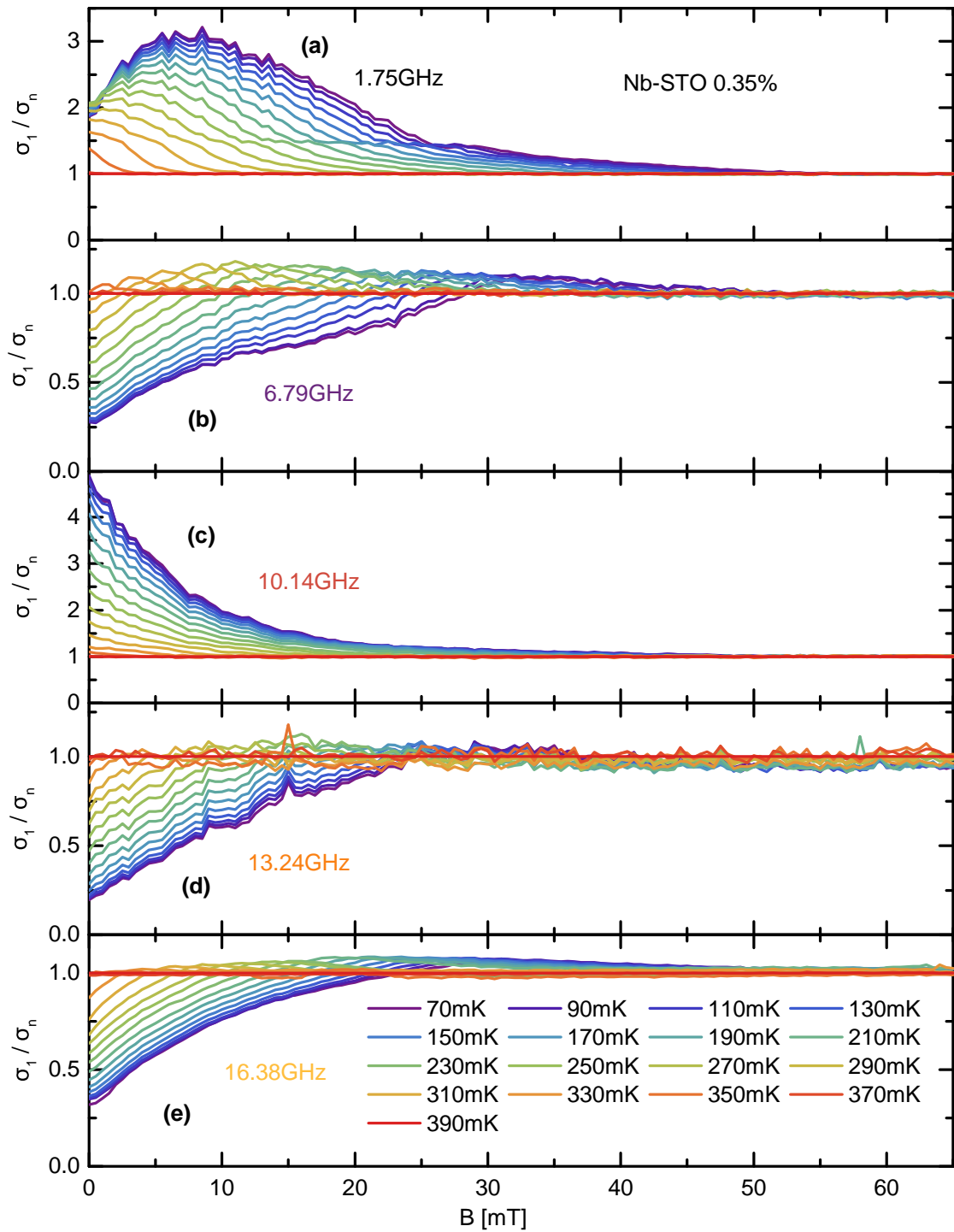
where n_s is the density of superconducting electrons and n_n the one of normal conducting electrons. As both the frequency and the effective mass are known, the Cooper pair density can be calculated. In a first step, $\sigma_2^* \cdot f$ and $\sigma_2(0\text{ T}) \cdot f$ are calculated and plotted in Figure 4.20. Both bands contribute, weighted by the inverse of their effective mass, to $\sigma_2(0\text{ T})$. The consequent Cooper pair densities are in the same order of magnitude as data taken from literature [Lin *et al.*, 2014a].

As already mentioned Nb doped STO is a *multi-band superconductor* of type-II. Thus, two vortices of different bands share their position within an Abrikosov structure [Abrikosov, 1957a] within the Shubnikov phase as it can be seen in Figure 4.21 a in sketch ①. Each vortex dimension corresponds to

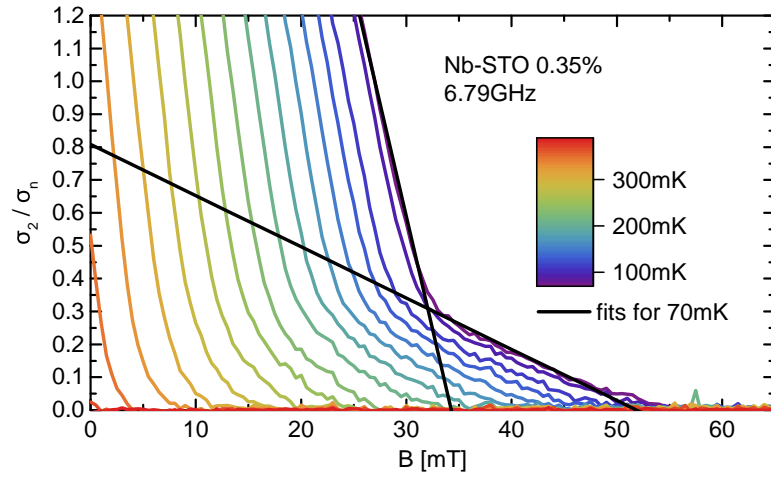


■ **Figure 4.17: Field-dependent imaginary part of the optical conductivity.** The plots (a) to (e) show σ_2 for five different frequencies. All share two characteristic features: A linear slope and two kinks as a function of magnetic field. Minor deviations in the linearity might be due to a matching point of R_S and X_S at too low temperatures, which is not deep in the Hagen-Rubens regime. The inset (f) presents both kinks, one within the superconducting state, the other one where σ_2 reaches 0. The explanation of both effects is given in [Figure 4.21](#).

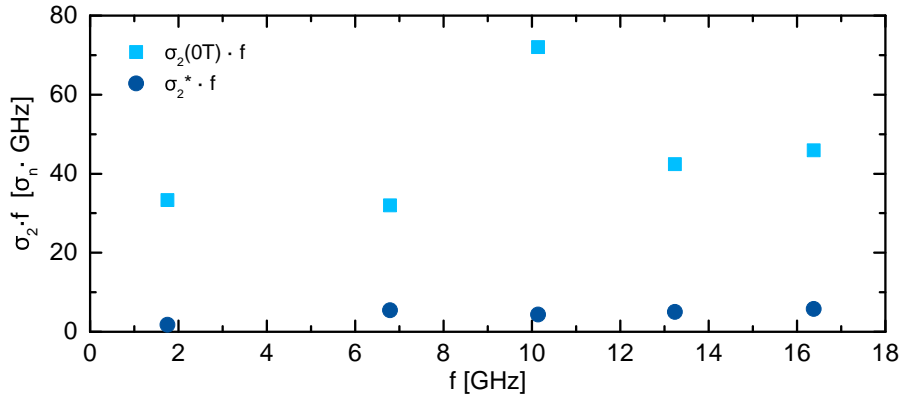
[Nb-STO 0.35%; Strip-01; 06.-10.08.2018]



■ **Figure 4.18: Field-dependent real part of the optical conductivity.** The real part of the conductivity looks way more messy than the imaginary part. Excluding the mode at 10 GHz, the frequency behavior shown an decreasing effect of overshooting over σ_n with an increasing frequency.



■ **Figure 4.19: Fits for field-dependent imaginary part of the optical conductivity.** The imaginary part of the optical conductivity was fitted via two linear functions revealing both the two exceptional magnetic fields and the conductivity at zero field $\sigma_2(0\text{ T})$ and the extrapolated conductivity σ_2^* at the intersection of the lower fit with the y-axis (in this case $4.7\sigma_n$ and $0.8\sigma_n$).
 [Nb-STO 0.35%; Strip-01; 06.-10.08.2018]



■ **Figure 4.20: Frequency-dependent filling of both bands at 70mK.** $\sigma_2(0\text{ T})$ and the extrapolated σ_2^* are determined via fits of the optical conductivity. The plotted values can be used to determine the Cooper pair density via the effective masses.
 [Nb-STO 0.35%; Strip-01; 06.-10.08.2018]

an electronic band i with its characteristic coherence length, which is given via [Buckel and Kleiner, 2013]

$$\xi_i = \sqrt{\xi_{i,0}\Lambda_i}. \quad (4.6)$$

in the dirty limit. Here

$$\Lambda_i = v_{F,i} \cdot \tau_i = \frac{v_{F,i}}{\Gamma_i} \quad (4.7)$$

is the *mean free path* with the Fermi velocity $v_{F,i}$ and the scattering rate Γ_i and

$$\xi_{i,0} = \frac{\hbar v_{F,i}}{\pi \Delta_i} \quad (4.8)$$

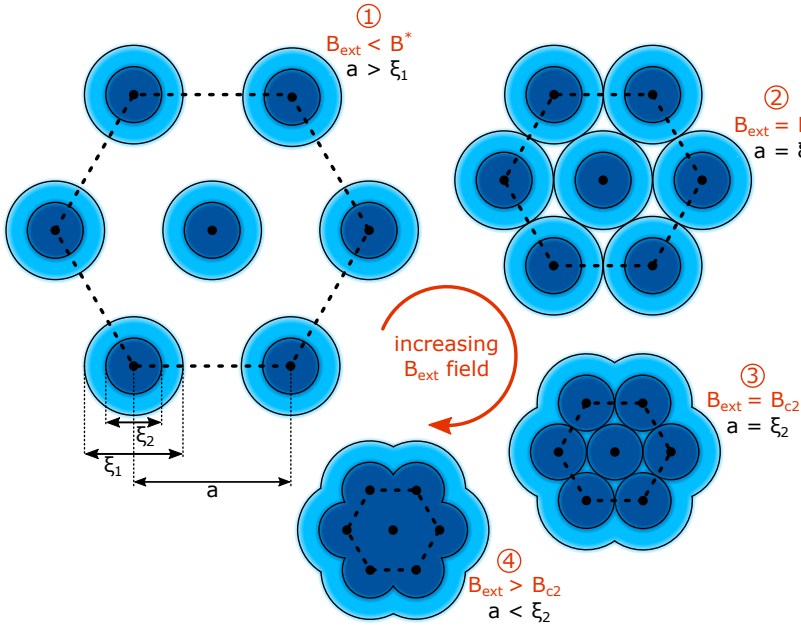


Figure 4.21 a: Abrikosov structure for four clockwise increasing external magnetic fields starting on the top left including the exceptional cases $B_{\text{ext}} = B^*$ and $B_{\text{ext}} = B_{c2}$.

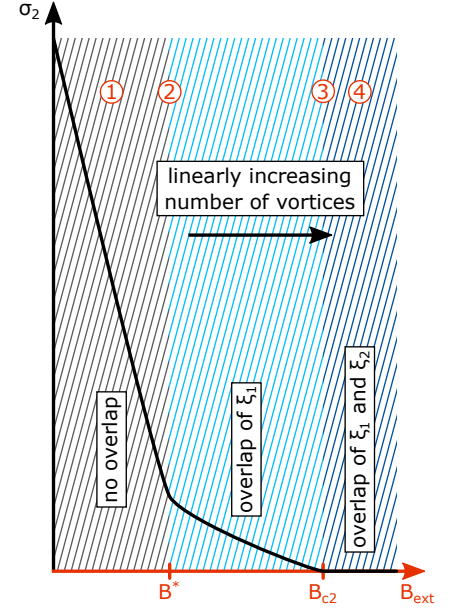


Figure 4.21 b: Field-dependent imaginary part of the conductivity with its two characteristic kinks.

■ **Figure 4.21: Shrinking Abrikosov structure [Abrikosov, 1957a] as a function of an increasing external magnetic field B_{ext} .** As B_{ext} increases, the distance between two adjacent vortices shrinks while the two coherence lengths ξ_1 and ξ_2 of the two superconducting bands are not effected. In this first sector the imaginary part of the electrical conductivity σ_2 decreases linearly due to a linearly increasing amount of vortices within the sample and is the weighted sum of the two bands. When the distance $a(B)$ between two vortices equals the coherence length ξ_1 of the first band, this band is no longer superconducting since the specific second critical field for this band is reached. Following [Thiemann *et al.*, 2018] this field is called B^* . For higher fields superconductivity is only present in one band. This results in a smaller slope of σ_2 in the middle sector of Figure 4.21 b. At the field where even the inner coherence length ξ_2 overlaps, superconductivity is suppressed completely as is it known for type-II superconductors for fields at B_{c2} and higher.

the corresponding coherence length for a pure superconductor [Bardeen *et al.*, 1957] with the *reduced Planck constant* \hbar and the *superconducting gap* Δ_i . For low magnetic fields all bands contribute to the superconductivity since the distance between two vortices [Tinkham, 1996]

$$a(B) = A \sqrt{\frac{\hbar}{2eB}} \quad (4.9)$$

with the geometry factor A - which will be neglected in the following - is larger than both coherence lengths ξ_1 and ξ_2 . At this point one should note the reciprocal B -dependence of a , whereas the coherence lengths stay constant under the influence of magnetic field.

As the influence of the vortex dynamics on the conductivity vanishes for the chosen measurement geometry, σ_2 directly reflects linearly the superfluid contribution. This is can be understood in terms of the two fluid model in equation (4.5). The imaginary part is only affected by the superfluid contribution and for frequencies well below the superconducting gap and the scattering rate the superfluid density

ρ_s can be calculated.

$$\begin{aligned}\sigma_2 &= \frac{1}{m^*\omega} \underbrace{n_s e^2 \frac{\mu_0}{m^*}}_{=\lambda_L^2} \frac{m^*}{\mu_0} \\ \Leftrightarrow \rho_s &:= \frac{1}{\lambda_L^2} = \mu_0 \omega \sigma_2(T, B)\end{aligned}\quad (4.10)$$

Here λ_L is the London penetration depth [London and London, 1935].

With an increasing field the number of vortices becomes linearly bigger since every vortex contains only one flux quantum. This causes ρ_s to shrink linearly forcing σ_2 to decrease linearly as well, which can be seen in [Figure 4.21 b](#). At the field B^* , where $a(B^*)$ exactly equals the larger coherence length ξ_2 , superconductivity is no longer present within this band due to overlapping vortices. In sketch ② of [Figure 4.21 a](#) that situation is shown. For an even more increasing magnetic field, σ_2 shrinks furthermore with another linear slope since the amount of vortices in the remaining superconducting band is still increasing. This linear decrease continues until $a(B) = \xi_2$ at ③, where superconductivity has been suppressed in all bands. That field is called B_{c2} as known in common single-band superconductivity and for a multi-band superconductor given in each band by [Buckel and Kleiner, 2013]

$$B_{c2,i} = \frac{\Phi_0}{2\pi\xi_i^2}. \quad (4.11)$$

The fact that there are only two exceptional critical fields visible, although three electronic bands contribute to the superconductivity [van der Marel *et al.*, 2011] is due to the same effective mass in the upper two bands. [Lin *et al.*, 2014a]

4.4.3 Temperature-dependent Critical Fields and Effective Electron Masses

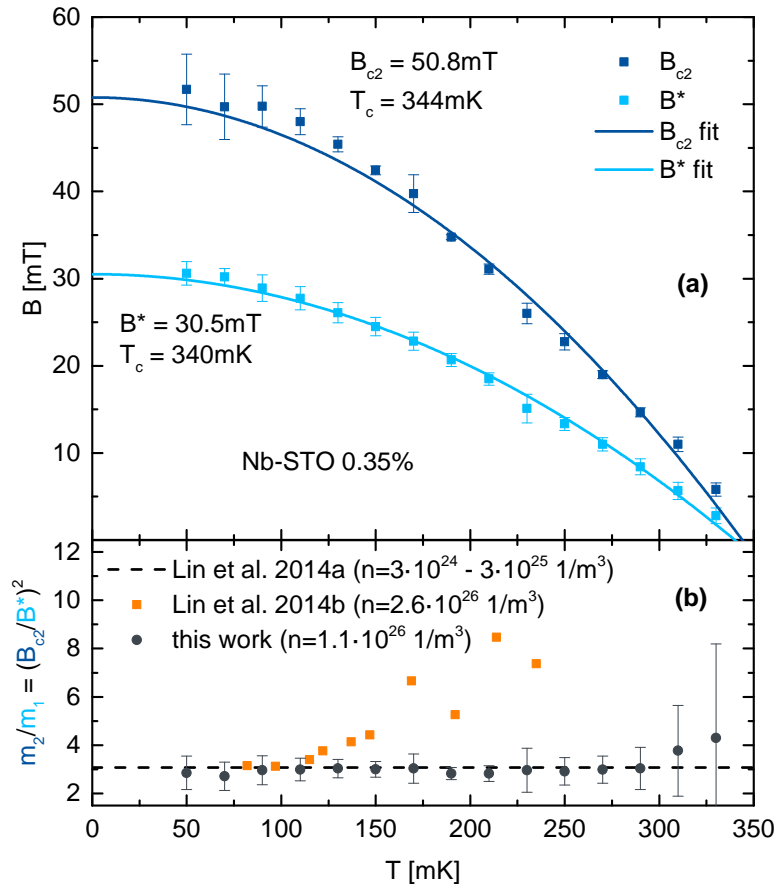
From the field dependence of σ_2 or the bandwidth f_B both two kinks can be read out for every mode. The mean value of those values is plotted over the corresponding temperature in plot (a) in [Figure 4.22](#). The error bars find their origin in the standard deviations of the different modes 1, 4, 6, 7, 8 and 10. Both the lower critical field B^* - which should explicitly not be mixed up with the first critical field B_{c1} in type II superconductors - and the upper critical field B_{c2} are fitted with a common empirical function. [Tinkham, 1996]

$$B_c(T) = B_{c,0} \left(1 - \left(\frac{T}{T_c} \right)^2 \right) \quad (4.12)$$

Here $B_{c,0}$ is the critical field at zero temperature and T_c the critical temperature. The fitted critical temperatures of 340 mK and 344 mK are in good accordance with other groups [Pfeiffer and Schooley, 1969; Binnig *et al.*, 1980; Lin *et al.*, 2014a] since the sample with this doping is near the maximum value of the superconducting dome.

By plugging in equations (4.6) and (4.8) into (4.11) the dependences $B_c^2 \sim \frac{1}{\xi^2} \sim \frac{1}{v_F^2} \sim m^*$ are obtained and the ratio of the effective masses can be worked out via

$$\left(\frac{B_{c2}}{B^*} \right)^2 = \frac{m_2^*}{m_1^*}, \quad (4.13)$$



■ **Figure 4.22: Critical fields and effective mass ratio as a function of temperature.** In subplot (a) all exceptional magnetic fields B^* and B_{c2} are shown and fitted with common empirical functions as given in the main text. The error bars emerge from the evaluation of the different modes. The squared ratio of the two fields is plotted in (b), which is simultaneously the ratio of the effective masses as explained in the main text. Equivalent data based on other publications [Lin *et al.*, 2014a,b] is also included and in good accordance with the results of this work.

[Nb-STO 0.35%; Strip-01; 06.-10.08.2018]

where indices 1 and 2 denote the different bands. Within this calculation an equal scattering rate Γ is assumed for both bands, which can be justified by a predominant scattering at crystal impurities, which are not dependent on the wave vector \vec{k} . Furthermore, a global Fermi level over all bands is assumed to conclude from v_F to m^* . Contemplating the optical response function of Nb-STO [Thiemann *et al.*, 2018], the superconducting gap is equal for both bands as well. This is due to the high scattering rate in the dirty limit and is discussed in the theory section of this work.

Following this procedure for every measured temperature results in the plot (b) of Figure 4.22, where the ratio is plotted as a function of temperature. The received values match other measurements in literature, which are obtained by kinks in the thermal conductivity [Lin *et al.*, 2014b] and by Shubnikov-de Haas oscillations [Lin *et al.*, 2014a].

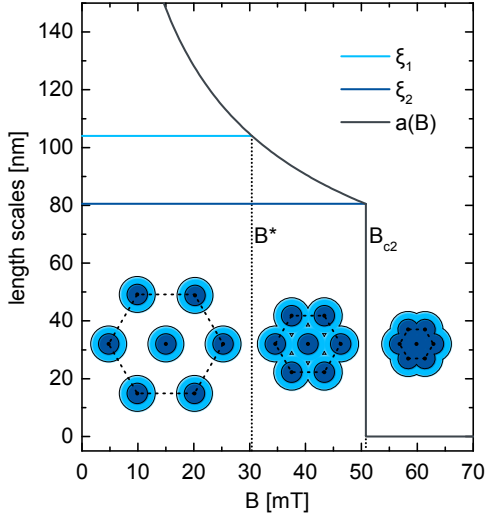


Figure 4.23 a: The inter vortex distance $a(B)$ is plotted over B . At the two critical fields a equals ξ_1 and ξ_2 respectively.

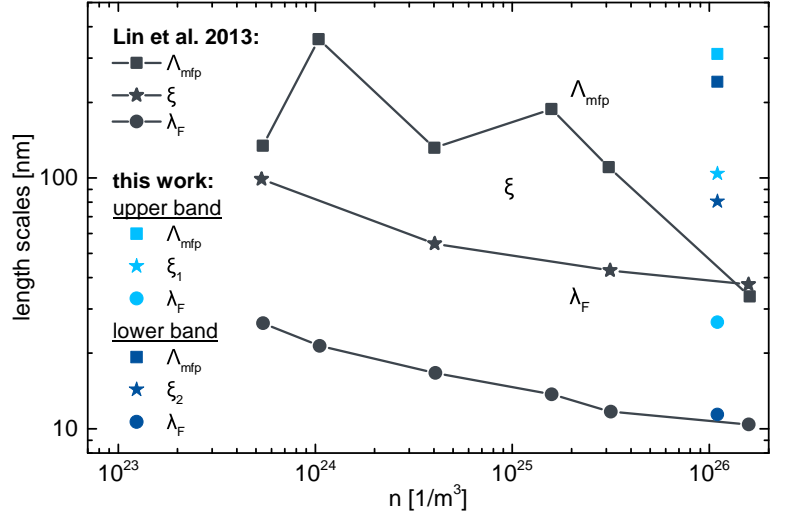


Figure 4.23 b: All derived length scales ξ , Λ_{mfp} and λ_F are shown for both bands as described in the main text. The compare well to data literature. [Lin *et al.*, 2013]

■ **Figure 4.23: Comparison of different length scales.** A smaller mean free path than π^2 times the coherence length suggests that Nb-STO is within the regime of dirty limit superconductivity. This justifies the appearance of only one superconducting gap. Moreover, a smaller λ_F than ξ forces Nb-STO to be at the BCS side of the BCS-BEC crossover since the wave functions of the Cooper pairs overlap each other.

4.4.4 Comparison of Length Scales

Considering both critical magnetic fields for the two bands of $B^* = 30.5 \text{ mT}$ and $B_{c2} = 50.8 \text{ mT}$ and equation (4.11) the superconductive coherence lengths can be determined and appear to be $\xi_1 = 104 \text{ nm}$ for the upper band and $\xi_2 = 80.5 \text{ nm}$ for the lower band. These calculated values are in the same order of magnitude as recently published data. [Lin *et al.*, 2013]

Plotting the field independent coherence lengths and the distance between two vortices $a(B)$ of equation (4.9) over the magnetic field reflects the explanation of overlapping vortices of the previous chapter. This plot is given in Figure 4.23 a, in which the two critical fields are exactly at the position, where $a(B)$ undercuts both ξ_1 and ξ_2 . Moreover, for the three phases a sketch of the corresponding hexagonal Abrikosov structure is drawn.

To classify the calculated coherence lengths a comparison with other length scales is needed. Therefore, first of all, the Fermi velocities for both bands need to be determined, which is achieved via the previous mentioned equations (4.6), (4.8) and (4.11). The measured critical field is expressed as a function of the Fermi velocity v_F , the superconducting gap Δ_0 and the scattering rate Γ_{sf} . Both Δ_0 and Γ_{sf} have been taken from [Thiemann *et al.*, 2018], where the gap is measured by the optical response function and the scattering rate determined via the temperature dependence of the superfluid density as it will be shown in the paragraph below. In an impurity dominated scattering regime the mean free path is in a first approach equal for all bands. Implying different Fermi velocities the global mean free path yields different scattering rates for each band, but as explained previously Γ is a experimentally hard accessible quantity [Dressel and Scheffler, 2006], which justifies a first approximation of a global scattering rate. As an anticipation, this approximation will also justify different Fermi energies among different bands. However, these calculations yield Fermi velocities of $v_{F,1} = 21000 \frac{\text{m}}{\text{s}}$ for the upper

band and $v_{F,2} = 16000 \frac{\text{m}}{\text{s}}$ for the lower band. These velocities are once more in the same range as data taken from literature measured with quantum oscillations. [Lin *et al.*, 2013]

Via the Fermi momentum p_F and the effective mass the Fermi wave vector k_F can be worked out, yielding to the Fermi wavelength $\lambda_F = \frac{2\pi}{k_F}$. Using the Fermi velocities and the electron masses of both bands [Lin *et al.*, 2014a] they are given by $\lambda_{F,1} = 26.6 \text{ nm}$ for the upper band and $\lambda_{F,2} = 11.4 \text{ nm}$ for the lower band.

As another comparable length scale the mean free path can be calculated via [Hunklinger, 2011]

$$\Lambda_{\text{mfp}} = \frac{v_F}{\Gamma_{\text{sf}}} \quad (4.14)$$

and yields $\Lambda_{\text{mfp},1} = 124.3 \text{ nm}$ and $\Lambda_{\text{mfp},2} = 94.7 \text{ nm}$ for the two different bands respectively.

All three length scales are compared to each other and to the mentioned determinations in literature in [Figure 4.23 b](#).

As the dirty limit of superconductivity is defined via $2\Delta_0 < \hbar\Gamma_{\text{sf}}$, the same condition can be worked out in terms of length scales: $\pi^2\xi > \Lambda_{\text{mfp}}$. Since π^2 times the coherence lengths are larger than the corresponding mean free paths for both bands, the justification of the dirty limit is given.

Furthermore, the Fermi wavelengths - which are basically the distance between the electrons - are smaller for both bands than their coherence lengths. This pushes Nb-STO on the BCS side of the BCS-BEC crossover (*Bose-Einstein condensate*) due to a sufficiently long range of the coherence within superconductivity, exceeding the Fermi wavelengths. This goes along with literature as well. [van der Marel *et al.*, 2011; Lin *et al.*, 2013]

4.4.5 Superfluid Density and Homes' Law

Another interesting and instructive quantity is the superfluid density ρ_s , which is defined via equation (4.10). It is calculated for the lowest measured frequency to stay well below Δ_0 , since the approximation is only valid for a $\frac{1}{\omega}$ behavior of σ_2 . The field- and temperature-dependence is shown in [Figure 4.24 a](#). By using a logarithmic color map this can be interpreted as a *phase diagram* with the superfluid density as an *order parameter* to distinguish between the different phases. Whereas blue denotes superconductivity in all bands and white only one superconducting band, red area is in the normal conducting state, where superconductivity is suppressed either by field or temperature or an interaction of both. Both two kinks as also visible in this plot at the transition from blue to white and from white to red.

A profile plot at zero field is shown in [Figure 4.24 b](#) with all measured data points as full dots. The dashed line belongs to fitted data for the weak coupling limit as explained in detail in the supplementary information of [Thiemann *et al.*, 2018] and yields a scattering rate of $\Gamma_{\text{sf}} = 169 \text{ GHz}$, where the index denotes that it has been extracted from the superfluid density. Γ_{sf} is also the scattering rate, which is referred to in the previous chapter and larger than the previous mentioned transport scattering rates. This issue is discussed in [Thiemann *et al.*, 2018].

Within *Ginzburg-Landau theory* [Ginzburg and Landau, 1950] an important quantity is the Ginzburg-Landau parameter κ_{GL} , which is defined as

$$\kappa_{\text{GL}} = \frac{\lambda_L}{\xi}. \quad (4.15)$$

It gives information about the energy scales needed to form vortices under a certain magnetic field within a superconductor of type II or to completely suppress superconductivity for a type I superconductor. For a $\kappa_{\text{GL}} > \frac{1}{\sqrt{2}}$ a type II superconductor is present due to a higher *displacement energy* than

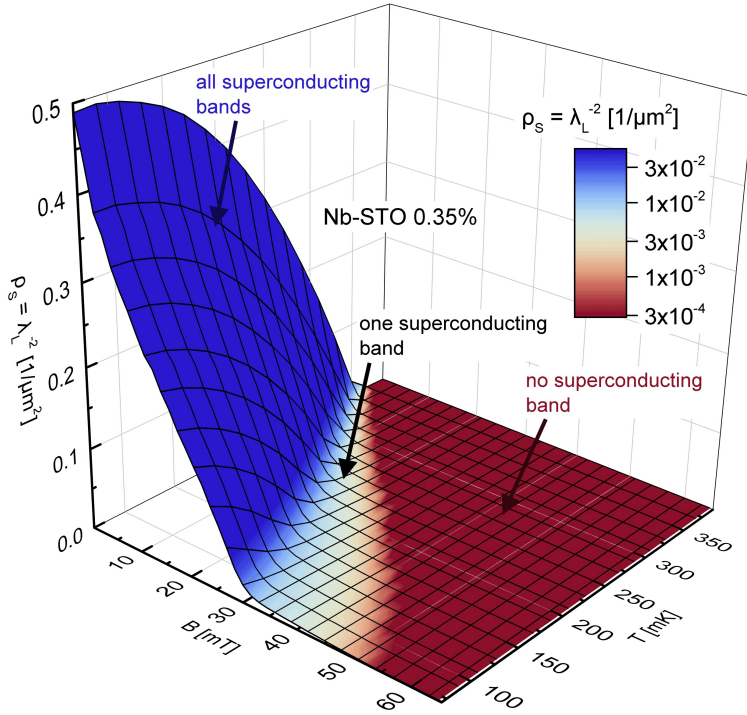


Figure 4.24a: Field- and temperature-dependent superfluid density.

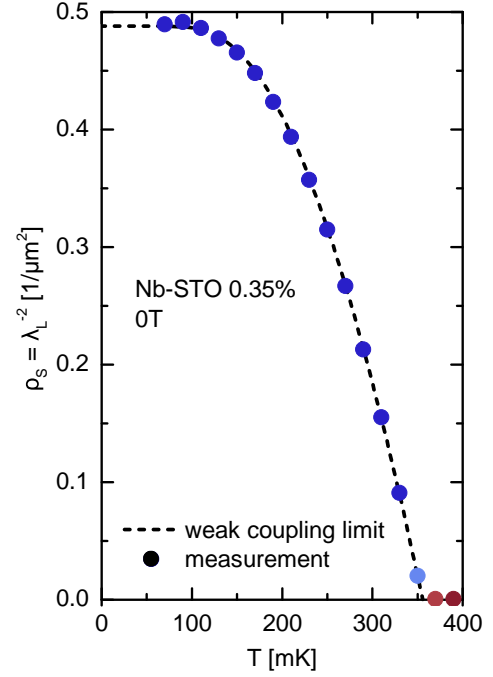


Figure 4.24b: Temperature-dependent superfluid density at zero magnetic field.

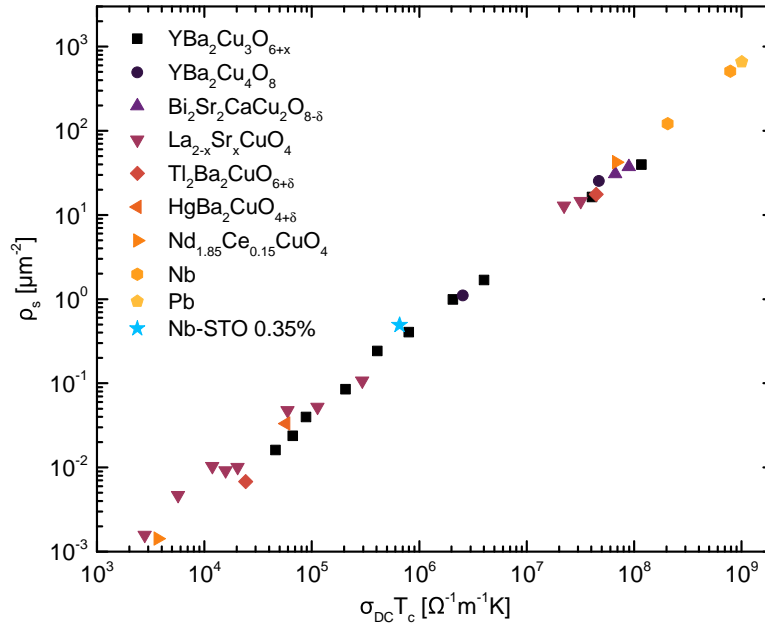
■ **Figure 4.24: Superfluid density as a function of magnetic field and temperature.** The values are calculated by the lower measured frequency to stay under the superconducting gap. The color map is logarithmic and represents the phase diagram of Nb-STO in this regime with ρ_s as an order parameter. While red symbolized no superconductivity, white stands for superconductivity in one band and blue means that all bands contribute to superconductivity.

condensation energy, whereas $\kappa_{GL} < \frac{1}{\sqrt{2}}$ reveals type I.[Abrikosov, 1957b]

For the present study ξ is indirectly measured via the field dependence of the optical conductivity and λ_L as defined in equation (4.10) can be extracted from the fitted superfluid density at zero temperature. The consequent values for κ_{GL} are between 6 and 9 and hence, far beyond the borderline of $\frac{1}{\sqrt{2}}$, confirming Nb-STO to be a type II superconductor.

A hint for superconductors to be in the dirty limit is an empirical relation between the superfluid density ρ_s at zero temperature and the DC resistivity measured just above the critical temperature multiplied by T_c itself. [Homes *et al.*, 2004] Superconductors being in the dirty limit clearly stay on a line within a double logarithmic plot as seen in Figure 4.25 for a variety of superconductors. This regularity is commonly called *Homes' Law*. A recent publication has shown that also superconductors at the edge of clean or dirty fulfill Homes' Law [Kogan, 2013], forcing only materials within the clean limit to not match the line.

In Figure 4.25 the 0.35% doped Nb-STO is shown as well. Since it matches Homes' Law with a remarkable accuracy it can be stated not to be in the clean limit.

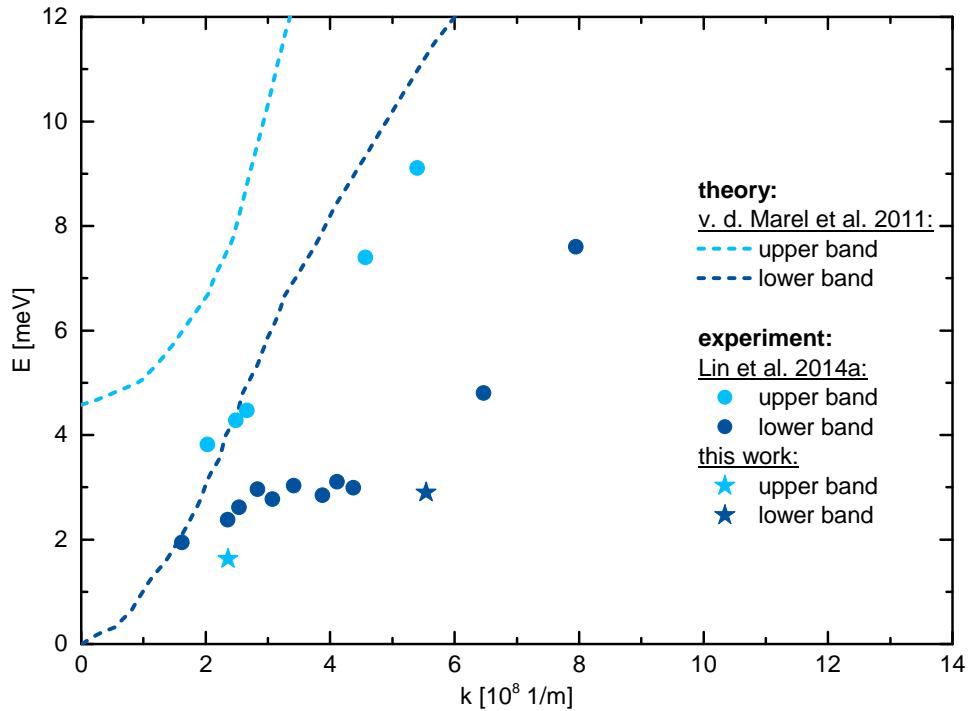


■ **Figure 4.25: Homes' Law for several superconductors including Nb-STO.** As empirically found for superconductors in the dirty limit [Homes *et al.*, 2004] the superfluid density plotted over the DC resistivity just above T_c times the critical temperature follows a straight line within a double logarithmic plot. Recently it was shown that only superconductors far in the clean limit do not stick to this line. [Kogan, 2013] Within this plot the different definition of ρ_s by a factor of $4\pi^2$ in contrast to the original paper needs to be mentioned.

4.4.6 Dispersion Relation

As a last feature the Fermi wave vector will be classified and compared with other publications within a *dispersion relation*. Therefore, the Fermi energy is calculated from the Fermi velocity and plotted as a function of the wave vector k_F as seen in Figure 4.26. Solid dots and dashed lines belong to experimental [Lin *et al.*, 2014a] and theoretical [van der Marel *et al.*, 2011] data, assuming no interaction between the different electrons. As mentioned before, a rough approximation of a global scattering rate, yields only rough Fermi velocities that do not end up in the same Fermi energy for both bands.

Nevertheless, it can be said that the absolute values match the other experimental data, at least for the lower band. Moreover, the shape of the upper band follows the parabolic and the lower band a non-parabolic behavior of the theoretical data. However, the absolute values of both experiments are not in accordance with theoretical predictions and might be due to a mass renormalization and hence, a twice as large effective electron mass as in the theory paper.



■ **Figure 4.26: Dispersion relation for two bands.** Via calculations of the Fermi energy and the Fermi wave vector as outlined in the main text, both bands can be put into relation of other measurements in literature. [van der Marel *et al.*, 2011; Lin *et al.*, 2014a] The experimental values match to the ones of this work, while the theoretical predictions differ in absolute numbers.

4.4.7 Summary and Conclusions

Finally it can be said that Nb-STO is a type II superconductor, matches Homes' Law and can be placed in the limit of a dirty superconductor. Multiple bands contribute to superconductivity as it was supposed in literature before [Binnig *et al.*, 1980], which are identified in this work via two kinks at the exceptional magnetic fields B^* and B_{c2} within the complex optical conductivity. These two different scales in field find their origin in two different coherence lengths. In contrast to recent literature [Lin *et al.*, 2014b] the cause of these two length scales is not founded in two different superconducting gaps Δ_0 as microwave data revealed [Thiemann *et al.*, 2018], but in different Fermi velocities $v_{F,i}$ for the two different bands.

To summarize all measured, calculated and literature data for both bands [Table 4.1](#) shall be used an overview for all these quantities.

Quantity	Upper Band (1)	Lower Band (2)	Measurement / Calculation / Reference
m^*	$1.3 m_e$	$4.0 m_e$	[Lin <i>et al.</i> , 2014a]
B_c	30.5 mT	50.8 mT	kinks in measurement of $\sigma_2(B)$
$\frac{1}{2\pi}\Gamma$	197.1 GHz	64.07 GHz	[Thiemann <i>et al.</i> , 2018]
$\frac{1}{2\pi}\Gamma_{sf}$	169 GHz	169 GHz	[Thiemann <i>et al.</i> , 2018]
Δ_0	$50.66 \mu\text{eV}$	$50.66 \mu\text{eV}$	[Thiemann <i>et al.</i> , 2018]
v_F	$21000 \frac{\text{m}}{\text{s}}$	$16030 \frac{\text{m}}{\text{s}}$	$B_c = \frac{\Phi_0}{2\pi \xi^2} = \frac{\Phi_0}{2\pi \xi_0 \Lambda_{\text{mfp}}} = \frac{\Phi_0}{2\pi \left(\frac{\hbar v_F}{\pi \Delta_0}\right) \left(2\pi \frac{v_F}{\Gamma_{sf}}\right)}$
k_F	$2.72 \cdot 10^8 \frac{1}{\text{m}}$	$5.53 \cdot 10^8 \frac{1}{\text{m}}$	$v_F m^* = p_F = \hbar k_F$
λ_F	26.6 nm	11.4 nm	$\lambda_F = \frac{2\pi}{k_F}$
E_F	1.63 meV	2.9 meV	$E_F = \frac{1}{2} m^* v_F^2$
Λ_{mfp}	124.3 nm	94.7 nm	$v_F = \frac{1}{2\pi} \Gamma_{sf} \cdot \Lambda_{\text{mfp}}$
ξ	104 nm	80.5 nm	$B_c = \frac{\Phi_0}{2\pi \xi^2}$
ξ_0	218.2 nm	168 nm	$\xi = \sqrt{\xi_0 \Lambda_{\text{mfp}}}$

■ **Table 4.1: Summary of quantites for Nb-STO 0.35% ($n_{\text{Hall}} = 1.1 \cdot 10^{20} \text{ cm}^{-3}$).** This chart gives an overview of all determined quantities, such as the effective electron mass m^* , the second critical field B_c , the scattering rates Γ and Γ_{sf} from Hall measurements and superfluid density measurements respectively, the superconducting gap Δ_0 , the Fermi velocity v_F , the Fermi wave vector k_F , the Fermi wave length λ_F the Fermi energy E_F , the mean free path Λ_{mfp} , the actual coherence length ξ and the clean limit coherence length ξ_0 . Within the whole thesis the light blue color corresponds to the upper band, while the lower band is marked in dark blue.

Summary and Outlook

For the semiconductor strontium titanate (STO) a dome-shaped superconducting transition as a function of n -doping can be observed. Due to its remarkably low charge carrier density, the energy scales within this material are comparably small, restricting the possible pairing mechanisms of Cooper pairs. This work shall contribute to the understanding of the electronic properties of Nb-doped STO. The main goal was to check the feasibility of cyclotron resonance measurements on doped STO to characterize the effective electron masses and to indicate the role of the effective masses for the superconducting state of STO.

Summary

To observe cyclotron resonance, a sufficiently low scattering rate within the probed material is a requirement of utmost importance among other possible complications. Consequently, the scattering rate is quantified from transport measurements, revealing frequencies in the order of several tens of GHz for both the copper and the Nb-STO sample, which is in line with data taken from literature [Thompson *et al.*, 1990; Thiemann *et al.*, 2018; Lin *et al.*, 2014a, 2015b]. Improvement of the scattering rate of the copper samples due to annealing was not observed.

Using microwave coplanar and stripline waveguides and an in-situ control of the distance from the sample to the waveguide, several attempts to measure cyclotron resonance have been performed. One of them revealed evidence for a cyclotron resonance signal, yielding effective electron masses in the order of 3 to $4m_e$ and scattering rates of 9 to 10 GHz. The obtained data are in good accordance with data in literature [Lin *et al.*, 2014a; Thiemann *et al.*, 2018], although they should be treated with care, since this measurement could not be reproduced within this study.

Proceeding to the superconducting state of Nb-STO, measurements of the complex *optical conductivity* at GHz frequencies have been performed, which revealed two different *coherence lengths* of different bands. Using the proportionality $\xi^2 \sim v_F^2 \sim \frac{1}{m^*}$, the effective electron masses can be characterized further. It was possible to determine the ratio of masses of both bands to a value of around 3, matching the results of previous measurements via *thermal conductivity* [Lin *et al.*, 2014a] and *quantum oscillations* [Lin *et al.*, 2014b].

Furthermore, information gained from optical conductivity was used to determine several other char-

acteristic quantities, such as the *mean free path*, the *Fermi velocities* of both superconducting bands, and the *superfluid density*. Using the latter, the *London penetration depth* and the *Ginzburg-Landau parameter* are derived, confirming Nb-STO to be a *type II superconductor*. Moreover, the *dirty-limit* behavior of a superconductor is observed and confirmed via *Homes' Law*, and the scale of the mean free path compared to the coherence length.

All these properties are evidence for single-gap superconductivity within multiple bands for Nb-STO, as proposed recently by [Thiemann *et al.*, 2018].

Outlook

Since observation of cyclotron resonance was not yet routinely achieved with the used setup, one has to think about strategies to improve the measurement and to increase the signal strength.

Lowering the scattering rate might be one option for certain test materials, but cannot be applied to the particular material of interest, viz. Nb-doped STO, due to the dominant contribution to scattering of doping itself. The only alternative at this point would be shifting to higher frequencies, which in principle is possible for planar superconducting resonators. [Rausch *et al.*, 2018; Wollandt *et al.*, 2018] These would go along with higher magnetic fields, which will exceed the present limit of 8 T at the used setup and cause several experimental challenges, especially with respect to operation of superconducting resonators [Song *et al.*, 2009; Singh *et al.*, 2014; Bothner *et al.*, 2012].

Furthermore, other methods of probing the electron mass should be considered, for instance quantum oscillations [Landau, 1930], such as the *Shubnikov-de Haas effect* [Schubnikow and de Haas, 1930] and the *de Haas-van Alphen effect* [de Haas and van Alphen, 1930], or DC transport measurements combined with optical Hall effect measurements [Schubert *et al.*, 2003].

Concerning experiments on superconductive Nb-STO, further efforts are needed to fully understand the rich phenomenology of the optical conductivity data obtained in magnetic field, in particular to achieve a quantitative description of the complex conductivity. Additional experiments should explicitly address the role of the field geometry, to confirm that the present experiments are not affected by vortex dynamics or hysteresis. Furthermore, microwave experiments in magnetic field for other doping levels will allow to characterize the role of the multiple superconducting bands throughout the superconducting dome of Nb-STO.

Operation Manual for VTI

This manual shall give a short introduction in the procedure of measuring at the VTI setup for subsequent students.

A.1 Sample mounting and cooling

1. After placing the sample on the microwave waveguide two brass screws are used to fix the microwave box on the *cold finger*. (In case of using a positioner or a rotator the sample is of course not placed on the waveguide.)
2. Both coaxial cable need to be attached to the connectors at the box and the brass cover screwed above the cold finger.
3. The grey valve to the *recovery line* stays open all the time.
4. To insert the *sample bar* into the cryostat, first the pump is disconnected and the red recovery line valve is opened to rise the pressure to 1 bar within the *sample chamber*. Then the silver cap in the middle is removed, replaced by the sample bar and attached with a clamp.
5. Pump and flush the sample chamber for around three times. (Close recovery valve, open pump valve, wait till pressure drops near 0 bar, close pump valve, open recovery valve)
6. Close recovery valve and open the valve to the pump permanently.
7. Now the needle valve can be slowly opened. For cooling down it can be opened as wide as several cycles. (Note that the pressure in the sample chamber should not exceed 0.5 bar!)
8. If the temperature is as low as 2 K, the needle valve has to be carefully adjusted. If it its to wide open, it causes lots of helium wastage and the temperature will not drop to the lowest achievable temperature. A to closed valve is hard to realize as such in the beginning. The temperature will drop to rather low temperatures, but at a certain point all helium will be sucked out and the temperature rises immediately.

9. After finding the right position for the needle valve (at the time of this thesis around $\frac{1}{8}$ open) and letting the temperature drop to the lowest possible value, the heater can be set to the desired temperature setpoint and the measurement can be started.

A.2 Warming and sample removing

1. After the measurement is done the needle valve can be closed completely carefully.
2. To blow out the accumulated helium inside the sample chamber the heater temperature setpoint can be slowly increased. (Empirically to around 10 K) The pressure will increase but still should not extend 0.5 bar (if so, immediately set heater to manually to 0 power)
3. After the pressure reached approximately 0 bar again at the appointed temperature all helium has been blown out into the recovery line and the setpoint can be set to 300 K. The heating procedure will take about 90 min.
4. When the temperature reached 300 K the pump can be disconnected and red recovery valve can be opened to reach atmosphere pressure inside the sample chamber again. Then the sample bar can be removed and replaced by the silver cap again.
5. Pump and flush again for three times.
6. Close recovery valve and open the valve to the pump permanently.

References

- A. A. Abrikosov, *The magnetic properties of superconducting alloys*, Journal of Physics and Chemistry of Solids **2**, 199-208 (1957)
- A. A. Abrikosov, *On the Magnetic Properties of Superconductors of the Second Group*, Journal of Experimental and Theoretical Physics **5**, 1174 (1957)
- Y. Aiura, I. Hase, H. Bando, T. Yasue, T. Saitoh, and D. Dessauc, *Photoemission study of the metallic state of lightly electron-doped SrTiO₃*, Surface Science **515**, 61–74 (2002)
- P. Anderson, *Theory of dirty superconductors*, Journal of Physics and Chemistry of Solids **11**, 26–30 (1959)
- J. Appel, *Soft-Mode Superconductivity in SrTiO₃*, Physical Review **180**, 508 (1969)
- M. Y. Azbel' and E. A. Kaner, *Cyclotron resonance in metals*, Journal of Physics and Chemistry of Solids **6**, 113–135 (1957)
- J. Bardeen, L. N. Cooper, and J. R. Schrieffer, *Theory of Superconductivity*, Physical Review **108**, 1175 (1957)
- J. G. Bednorz and K. A. Müller, *Possible highT_c superconductivity in the Ba-La-Cu-O system*, Zeitschrift für Physik B Condensed Matter **64**, 189–193 (1986)
- G. Binnig, A. Baratoff, H. E. Hoenig, and J. G. Bednorz, *Two-Band Superconductivity in Nb-Doped SrTiO₃*, Physical Review Letters **45**, 1352 (1980)
- J. C. Booth, D. H. Wu, and S. M. Anlage, *A broadband method for the measurement of the surface impedance of thin films at microwave frequencies*, Review of Scientific Instruments **65**, 2082 (1994)
- D. Bothner, C. Clauss, E. Koroknay, M. Kemmler, T. Gaber, M. Jetter, M. Scheffler, P. Michler, M. Dressel, D. Koelle, and R. Kleiner, *Reducing vortex losses in superconducting microwave resonators with microsphere patterned antidot arrays*, Applied Physics Letters **100**, 012601 (2012)
- G. J. Bowden, P. R. Elliston, K. T. Wan, K. E. Easterling, A. Bourdillon, C. C. Sorrell, B. A. Cornell, and F. Separovic, *EPR and NMR measurements on high-temperature superconductors*, Journal of Physics C: Solid State Physics **20**, L545–L552 (1987)
- D. Broun, *The Microwave Electrodynamics of Unconventional Superconductors*, Dissertation, University of Cambridge (2000)
- W. Buckel and R. Kleiner, *Supraleitung - Grundlagen und Anwendungen*, WILEY-VCH Verlag (2013)
- M. Cardona, *Optical Properties and Band Structure of SrTiO₃ and BaTiO₃*, Physical Review **140**, A651 (1965)
- A. D. Caviglia, S. Gariglio, N. Reyren, D. Jaccard, T. Schneider, M. Gabay, S. Thiel, G. Hammerl, J. Mannhart, and J.-M. Triscone, *Electric field control of the LaAlO₃/SrTiO₃ interface ground state*, Nature **456**, 624–627 (2008)

- Y. J. Chang, A. Bostwick, Y. S. Kim, K. Horn, and E. Rotenberg, *Structure and correlation effects in semiconducting SrTiO₃*, Physical Review B **81**, 235109 (2010)
- C. Clauss, D. Bothner, D. Koelle, R. Kleiner, L. Bogani, M. Scheffler, and M. Dressel, *Broadband electron spin resonance from 500 MHz to 40 GHz using superconducting coplanar waveguides*, Applied Physics Letters **102**, 162601 (2013)
- O. M. Corbino, *Azioni Elettromagnetiche Dovute Agli Ioni Dei Metalli Devianti Dalla Traiettorie Normale Per Effetto Di Un Campo*, Nuovo Cimento **1**, 397 (1911)
- R. Courths and S. Hufner, *Photoemission experiments on copper*, Physics Reports **112**, 53–171 (1984)
- Y. Dalichaouch, M. C. de Andrade, and M. B. Maple, *Superconducting and magnetic properties of the heavy-fermion compounds UT₂Al₃ (T=Ni,Pd)*, Physical Review B **46**, 8671(R) (1992)
- P. Das, R. B. de Ouboter, and K. W. Taconis, *A Realization of a London-Clarke-Mendoza Type Refrigerator*, Low Temperature Physics **LT9**, 1253 (1964)
- W. J. de Haas and P. van Alphen, *The dependence of the susceptibility of diamagnetic metals upon the field*, Proceedings of the Academy of Science of Amsterdam **33**, 1106 (1930)
- R. N. de Mesquita, J. H. Castilho, G. E. Barberis, C. Rettori, I. Torriani, O. F. de Lima, S. Gama, R. F. Jardim, M. C. Terrile, H. Basso, and O. R. Nascimento, *ESR experiments and spectra simulations in YBa₂Cu₃O_{7-x}, Y₂BaCuO₅, and BaCuO_{2+x}*, Physical Review B **39**, 6694–6699 (1989)
- W. Demtröder, *Experimentalphysik 3 Atome, Moleküle und Festkörper*, Springer Berlin Heidelberg New York (2005)
- M. Dressel and G. Grüner, *Electrodynamics of Solids: Optical Properties of Electrons in Matter*, Cambridge University Press (2002)
- M. Dressel and M. Scheffler, *Verifying the Drude response*, Annalen der Physik **15**, 535 (2006)
- G. Dresselhaus, A. F. Kip, and C. Kittel, *Cyclotron Resonance of Electrons and Holes in Silicon and Germanium Crystals*, Physical Review **98**, 368 (1955)
- P. Drude, *Zur Elektronentheorie der Metalle*, Annalen der Physik **306**, 566–613 (1900)
- N. G. Ebensperger, M. Thiemann, M. Dressel, and M. Scheffler, *Superconducting Pb stripline resonators in parallel magnetic field and their application for microwave spectroscopy*, Superconductor Science and Technology **29**, 11 (2016)
- J. M. Edge, Y. Kedem, U. Aschauer, N. A. Spaldin, and A. V. Balatsky, *Quantum Critical Origin of the Superconducting Dome in SrTiO₃*, Physical Review Letters **115**, 247002 (2016)
- A. Einstein, *Zur Elektrodynamik bewegter Körper*, Annalen der Physik und Chemie **17**, 891–921 (1905)
- E. Fawcett, *Cyclotron Resonance in Tin and Copper*, Physical Review **103**, 1582 (1956)
- E. Fermi, *Zur Quantelung des idealen einatomigen Gases*, Zeitschrift für Physik **36**, 902–912 (1926)

- C. Geibel, C. Schank, S. Thies, H. Kitazawa, C. D. Breidl, A. Böhm, M. Rau, A. Grauel, R. Caspary, R. Helfrich, U. Ahlheim, G. Weber, and F. Steglich, *Heavy-fermion superconductivity at $T_c=2K$ in the antiferromagnet UPd_2Al_3* , *Zeitschrift für Physik B Condensed Matter* **84**, 1–2 (1991)
- S. Gevorgian, L. J. P. Linner, and E. L. Kollberg, *CAD models for shielded multilayered CPW*, *IEEE Transactions on Microwave Theory and Techniques* **43**, 772–779 (1995)
- G. Ghione and C. U. Naldi, *Coplanar Waveguides for MMIC Applications: Effect of Upper Shielding, Conductor Backing, Finite-Extent Ground Planes, and Line-to-Line Coupling*, *IEEE Transactions on Microwave Theory and Techniques* **35**, 260–267 (1987)
- V. L. Ginzburg and L. D. Landau, *To the Theory of Superconductivity*, *Journal of Experimental and Theoretical Physics* **20**, 1064 (1950)
- O. Heaviside, *On the electromagnetic effects due to the motion of electrification through a dielectric*, *The London, Edinburgh, and Dublin Philosophical Magazine and Journal of Science* **27**, 324–339 (1889)
- C. C. Homes, S. V. Dordevic, M. Strongin, D. A. Bonn, R. Liang, W. N. Hardy, S. Komiya, Y. Ando, G. Yu, N. Kaneko, X. Zhao, M. Greven, D. N. Basov, and T. Timusk, *A universal scaling relation in high-temperature superconductors*, *Nature* **430**, 539–541 (2004)
- S. Hunklinger, *Festkörperphysik, 3. Auflage*, Oldenbourg Wissenschaftsverlag (2011)
- P. Häussler and S. J. Welles, *Determination of Relaxation Times in Cyclotron Resonance in Copper*, *Physical Review* **152**, 675 (1966)
- P. Häussler, *Relaxation times in cyclotron resonance in metals*, *Zeitschrift für Physik* **237**, 21–30 (1970)
- M. Huth, A. Kaldowski, J. Hessert, T. Steinborn, and H. Adrian, *Preparation and characterization of thin films of the heavy fermion superconductor UPd_2Al_3* , *Solid State Communications* **87**, 1133–1136 (1993)
- H. Ibach and H. Lüth, *Solid-State Physics An Introduction to Principles of Materials Science*, Springer-Verlag Berlin Heidelberg (2009)
- Y. Inada, H. Yamagami, Y. Haga, K. Sakurai, Y. Tokiwa, T. Honma, E. Yamamoto, Y. Onuki, and T. Yanagisawa, *Fermi Surface and de Haas-van Alphen Oscillation in both the Normal and Superconducting Mixed States of UPd_2Al_3* , *Journal of the Physical Society of Japan* **68**, 3643–3654 (1999)
- P. B. Johnson and J. A. Rayne, *Temperature Dependence of Carrier Scattering Rate in Copper from Magnetoacoustic Experiments*, *Australian Journal of Physics* **32**, 641–646 (1979)
- M. Jourdan, M. Huth, and H. Adrian, *Superconductivity mediated by spin fluctuations in the heavy-fermion compound UPd_2Al_3* , *Nature* **398**, 47–49 (1999)
- E. Kappler, W. Uelhoff, H. Fehmer, and F. Abbink, *Herstellung von Kupfereinkristallen kleiner Versetzungsdichte*, Springer Fachmedien Wiesbaden GmbH (1971)

- A. F. Kip, D. N. Langenberg, and T. W. Moore, *Cyclotron Resonance in Copper*, *Physical Review* **124**, 359 (1961)
- H. Kitano, T. Ohashi, and A. Maeda, *Broadband method for precise microwave spectroscopy of superconducting thin films near the critical temperature*, *Review of Scientific Instruments* **79**, 074701 (2008)
- O. Klein, S. Donovan, M. Dressel, and G. Grüner, *Microwave cavity perturbation technique: Part 1: Principles*, *International Journal of Infrared and Millimeter Waves* **14**, 2423–2457 (1993)
- J. F. Koch, R. A. Stradling, and A. F. Kip, *Some New Aspects of Cyclotron Resonance in Copper*, *Physical Review* **133**, A240 (1964)
- V. G. Kogan, *Homes scaling and BCS*, *Physical Review B* **87**, 220507(R) (2013)
- C. S. Koonce, M. L. Cohen, J. F. Schooley, W. R. Hosler, and E. R. Pfeiffer, *Superconducting Transition Temperatures of Semiconducting SrTiO₃*, *Physical Review* **163**, 380 (1967)
- L. Landau, *Diamagnetismus der Metalle*, *Zeitschrift für Physik* **64**, 629–637 (1930)
- D. N. Langenberg and S. M. Marcus, *Azbel'-Kaner Cyclotron Resonance in Gold*, *Physical Review* **136**, A1383 (1964)
- X. Lin, Z. Zhu, B. Fauque, , and K. Behnia, *Fermi Surface of the Most Dilute Superconductor*, *Physical Review X* **3**, 021002 (2013)
- X. Lin, G. Bridoux, A. Gourgout, G. Seyfarth, S. Krämer, M. Nardone, B. Fauque, and K. Behnia, *Critical Doping for the Onset of a Two-Band Superconducting Ground State in SrTiO_{3-δ}*, *Physical Review Letters* **112**, 207002 (2014)
- X. Lin, A. Gourgout, G. Bridoux, F. Jomard, A. Pourret, B. Fauque, D. Aoki, and K. Behnia, *Multiple nodeless superconducting gaps in optimally doped SrTi_{1-x}Nb_xO₃*, *Physical Review B* **90**, 140508(R) (2014)
- X. Lin, B. Fauque, and K. Behnia, *Scalable T² resistivity in a small single-component Fermi surface*, *Science* **349**, 945-948 (2015)
- X. Lin, C. W. Rischau, C. J. van der Beek, B. Fauque, and K. Behnia, *s-wave superconductivity in optimally doped SrTi_{1-x}Nb_xO₃ unveiled by electron irradiation*, *Physical Review B* **92**, 174504 (2015)
- W. Liu, L. Pan, and N. P. Armitage, *A broadband microwave Corbino spectrometer at ³He temperatures and high magnetic fields*, *Review of Scientific Instruments* **85**, 093108 (2014)
- F. London and H. London, *The electromagnetic equations of the supraconductor*, *Proceedings of the Royal Society A* **149**, 71–88 (1935)
- H. London, G. R. Clarke, and E. Mendoza, *Osmotic Pressure of He³ in Liquid He⁴, with Proposals for a Refrigerator to Work below 1°K*, *Physical Review* **128**, 1992 (1962)
- J. C. Maxwell, *On Physical Lines of Force*, *Philosophical Magazine* **90**, 11–23 (1861)

- F. Mehran, S. E. Barnes, T. R. McGuire, W. J. Gallagher, R. L. Sandstrom, T. R. Dinger, and D. A. Chance, , *Physical Review B* **36**, 740 (1987)
- W. H. Miller, *A Treatise on Crystallography*, J. & J. J. Deighton (1839)
- B. Mitrovic, *Effect of disorder on the far-infrared conductivity and on the microwave conductivity of two-band superconductors*, *Journal of Physics: Condensed Matter* **20**, 215220 (2008)
- K. A. Müller and H. Burkard, *SrTiO₃: An intrinsic quantum paraelectric below 4 K*, *Physical Review B* **19**, 3593 (1979)
- M. Mondal, A. Kamlapure, S. C. Ganguli, J. Jesudasan, V. Bagwe, L. Benfatto, and P. Raychaudhuri, *Enhancement of the finite-frequency superfluid response in the pseudogap regime of strongly disordered superconducting films*, *Scientific Reports* **3**, 1357 (2013)
- I. Newton, *Philosophiae Naturalis Principia Mathematica*, Jussu Societatis Regiae ac typis Josephi Streater (1687)
- D. E. Oates, A. C. Anderson, and P. M. Mankiewich, *Measurement of the surface resistance of YBa₂Cu₃O_{7-x} thin films using stripline resonators*, *Journal of Superconductivity* **3**, 251–259 (1990)
- G. S. Ohm, *Die galvanische Kette, mathematisch bearbeitet*, T.H. Riemann (1827)
- A. Ohtomo and H. Y. Hwang, *A high-mobility electron gas at the LaAlO₃/SrTiO₃ heterointerface*, *Nature* **427**, 423–426 (2004)
- M. Orlita, C. Faugeras, P. Plochocka, P. Neugebauer, G. Martinez, D. K. Maude, A.-L. Barra, M. Sprinkle, C. Berger, W. A. de Heer, and M. Potemski, *Approaching the Dirac Point in High-Mobility Multilayer Epitaxial Graphene*, *Physical Review Letters* **101**, 267601 (2008)
- A. Y. Ozerin, *Temperature dependence of the cyclotron resonance in graphene*, *JETP Letters* **98**, 839–842 (2014)
- P. J. Petersan and S. M. Anlage, *Measurement of resonant frequency and quality factor of microwave resonators: Comparison of methods*, *Journal of Applied Physics* **84**, 3392 (1998)
- E. R. Pfeiffer and J. F. Schooley, *Superconducting transition temperatures of Nb-doped SrTiO₃*, *Physics Letters* **29**, 589–590 (1969)
- N. C. Plumb and M. Radovic, *Angle-resolved photoemission spectroscopy studies of metallic surface and interface states of oxide insulators*, *Journal of Physics: Condensed Matter* **29**, 433005 (2017)
- D. Pozar, *Microwave Engineering, Second Edition*, John Wiley and Sons, Inc. (1998)
- U. Preppernau, R. Herrmann, L. Rothkirch, and H. Dwelk, *Cyclotron Resonance Investigations of Niobium*, *Physica Status Solidi (b)* **64**, 183 (1974)
- D. Rausch, M. Thiemann, M. Dressel, D. Bothner, D. Koelle, R. Kleiner, and M. Scheffler, *Superconducting coplanar microwave resonators with operating frequencies up to 50 GHz*, *Journal of Physics D: Applied Physics* **51**, 465301 (2018)
- C. Rettori, D. Davidov, I. Belaish, and I. Felner, *Magnetism and critical fields in the high-T_c superconductors YBa₂Cu₃O_{7-x}S_x (x = 0,1): An ESR study*, *Physical Review B* **36**, 4028(R) (1987)

- N. Reyren, S. Thiel, A. D. Caviglia, L. F. Kourkoutis, G. Hammerl, C. Richter, C. W. Schneider, T. Kopp, A.-S. Rüetschi, D. Jaccard, M. Gabay, D. A. Müller, J.-M. Triscone, and J. Mannhart, *Superconducting Interfaces Between Insulating Oxides*, *Science* **317**, 1196-1199 (2007)
- S. E. Rowley, L. J. Spalek, R. P. Smith, M. P. M. Dean, M. Itoh, J. F. Scott, G. G. Lonzarich, and S. S. Saxena, *Ferroelectric quantum criticality*, *Nature Physics* **10**, 367–372 (2014)
- M. Scheffler and M. Dressel, *Broadband microwave spectroscopy in Corbino geometry for temperatures down to 1.7 K*, *Review of Scientific Instruments* **76**, 074702 (2005)
- M. Scheffler, M. Dressel, M. Jourdan, and H. Adrian, *Extremely slow Drude relaxation of correlated electrons*, *Nature* **438**, 1135–1137 (2005)
- M. Scheffler, M. Dressel, M. Jourdan, and H. Adrian, *Dynamics of heavy fermions: Drude response in UPd_2Al_3 and UNi_2Al_3* , *Physica B: Condensed Matter* **378–380**, 993-994 (2006)
- M. Scheffler, M. Dressel, and M. Jourdan, *Microwave conductivity of heavy fermions in UPd_2Al_3* , *The European Physical Journal B* **74**, 331-338 (2010)
- M. Scheffler, C. Fella, and M. Dressel, *Stripline resonators for cryogenic microwave spectroscopy on metals and superconductors*, *Journal of Physics: Conference Series* **400**, 052031 (2012)
- M. Scheffler, K. Schlegel, C. Clauss, D. Hafner, C. Fella, M. Dressel, M. Jourdan, J. Sichelschmidt, C. Krellner, C. Geibel, and F. Steglich, *Microwave spectroscopy on heavy-fermion systems: Probing the dynamics of charges and magnetic moments*, *Physica Status Solidi b* **250**, 439 (2013)
- M. Scheffler, *Broadband Microwave Spectroscopy on Correlated Electrons*, Dissertation, Universität Stuttgart (2004)
- J. F. Schooley, W. R. Hosler, and M. L. Cohen, *Superconductivity in Semiconducting $SrTiO_3$* , *Physical Review Letters* **12**, 474 (1964)
- J. F. Schooley, W. R. Hosler, E. Ambler, J. H. Becker, M. L. Cohen, and C. S. Koonce, *Dependence of the Superconducting Transition Temperature on Carrier Concentration in Semiconducting $SrTiO-3$* , *Physical Review Letters* **14**, 305 (1965)
- M. Schubert, T. Hofmann, and C. M. Herzinger, *Generalized far-infrared magneto-optic ellipsometry for semiconductor layer structures: determination of free-carrier effective-mass, mobility, and concentration parameters in n-type GaAs*, *Journal of the Optical Society of America A* **20**, 347–356 (2003)
- L. Schubnikow and W. J. de Haas, *A New Phenomenon in the Change of Resistance in a Magnetic Field of Single Crystals of Bismuth*, *Nature* **126**, 500 (1930)
- V. Singh, B. H. Schneider, S. J. Bosman, E. P. J. Merckx, and G. A. Steele, *Molybdenum-rhenium alloy based high-Q superconducting microwave resonators*, *Applied Physics Letters* **105**, 222601 (2014)
- G. Singh, A. Jouan, G. Herranz, M. Scigaj, F. Sanchez, L. Benfatto, S. Caprara, M. Grilli, G. Saiz, F. Couedo, C. Feuillet-Palma, J. Lesueur, and N. Bergeal, *Single-band to two-band superconductivity transition in two-dimensional oxide interfaces*, arXiv:1806.02212 [cond-mat.supr-con] (2018)

- C. Song, M. P. DeFeo, K. Yu, and B. L. T. Plourde, *Reducing microwave loss in superconducting resonators due to trapped vortices*, Applied Physics Letters **95**, 232501 (2009)
- A. G. Swartz, H. Inoue, T. A. Merz, Y. Hikita, S. Raghu, T. P. Devereaux, S. Johnston, and H. Y. Hwang, *Polaronic behavior in a weak-coupling superconductor*, Proceedings of the National Academy of Sciences **115**, 1475 (2018)
- Y. Takada, *Theory of Superconductivity in Polar Semiconductors and Its Application to N-Type Semiconducting SrTiO₃*, Journal of the Physical Society of Japan **49**, 1267–1275 (1980)
- M. Takizawa, K. Maekawa, H. Wadati, T. Yoshida, A. Fujimori, H. Kumigashira, and M. Oshima, *Angle-resolved photoemission study of Nb-doped SrTiO₃*, Physical Review B **79**, 113103 (2009)
- M. Thiemann, M. H. Beutel, M. Dressel, N. R. Lee-Hone, D. M. Broun, E. Fillis-Tsirakis, H. Boschker, J. Mannhart, and M. Scheffler, *Single-Gap Superconductivity and Dome of Superfluid Density in Nb-Doped SrTiO₃*, Physical Review Letters **120**, 237002 (2018)
- C. Thompson, W. M. Manganaro, and F. Fickett, *Cryogenic Properties of Copper*, Copper Development Association Inc. (1990)
- M. Tinkham, *Introduction to Superconductivity*, McGraw-Hill Inc. (1996)
- S. Tonegawa, K. Hashimoto, K. Ikada, Y.-H. Lin, H. Shishido, Y. Haga, T. D. Matsuda, E. Yamamoto, Y. Onuki, H. Ikeda, Y. Matsuda, and T. Shibauchi, *Cyclotron Resonance in the Hidden-Order Phase of URu₂Si₂*, Physical Review Letters **109**, 036401 (2012)
- S. Tonegawa, K. Hashimoto, K. Ikada, Y. Tsuruhara, Y.-H. Lin, H. Shishido, Y. Haga, T. D. Matsuda, E. Yamamoto, Y. Onuki, H. Ikeda, Y. Matsuda, and T. Shibauchi, *Cyclotron resonance study of quasiparticle mass and scattering rate in the hidden-order and superconducting phases of URu₂Si₂*, Physical Review B **88**, 245131 (2013)
- D. van der Marel, J. L. M. van Mechelen, and I. I. Mazin, *Common Fermi-liquid origin of T^2 resistivity and superconductivity in n-type SrTiO₃*, Physical Review B **84**, 205111 (2011)
- D. C. Vier, S. B. Oseroff, C. T. Salling, J. F. Smyth, S. Schultz, Y. Dalichaouch, B. W. Lee, M. B. Maple, Z. Fisk, and J. D. Thompson, *Precautions when interpreting EPR and dc magnetization measurements of high- T_c RBa₂Cu₃O_{9-x}-phase superconducting materials*, Physical Review B **36**, 8888(R) (1987)
- A. Weismann, M. Wenderoth, S. Lounis, P. Zahn, N. Quaas, R. G. Ulbrich, P. H. Dederichs, and S. Blügel, *Seeing the Fermi Surface in Real Space by Nanoscale Electron Focusing*, Science **323**, 1190–1193 (2009)
- Y. Wiemann, J. Simmendinger, C. Clauss, L. Bogani, D. Bothner, D. Koelle, R. Kleiner, M. Dressel, and M. Scheffler, *Observing electron spin resonance between 0.1 and 67 GHz at temperatures between 50 mK and 300 K using broadband metallic coplanar waveguides*, applied Physics Letters **106**, 193505 (2015)
- T. Wollandt, M. Thiemann, M. Dressel, and M. Scheffler, *Superconducting stripline resonators at frequencies up to 50 GHz for microwave spectroscopy applications*, Journal of Physics: Conference Series **969**, 012082 (2018)

- E. Zavoisky, *Spin-magnetic resonance in paramagnetics*, Fizicheskii Zhurnal **9**, 211–245 (1945)
- P. Zeeman, *Ueber einen Einfluss der Magnetisirung auf die Natur des von einer Substanz emittirten Lichtes*, Verhandlungen der Physikalischen Gesellschaft zu Berlin **1**, 127 (1896)
- M. Zinßer, K. Schlegel, M. Dressel, and M. Scheffler, *Role of non-linear effects and standing waves in microwave spectroscopy: Corbino measurements on superconductors and VO₂*, arXiv preprint arXiv:1810.07784v1 (2018)
- M. Zinßer, *Frequency- and temperature-dependent microwave properties of superconducting samples in Corbino geometry*, Bachelor thesis, Universität Stuttgart (2016)

Acknowledgements

At the end of my thesis I want to thank all persons who helped and supported me during my work. I would particularly like to thank

- Prof. Dr. Martin Dressel for hosting me at the 1. Physical Institute at the University Stuttgart for my masters project in solid state physics.
- Prof. Dr. Peter Michler for being my second examiner.
- Dr. Marc Scheffler for his helpful and open personality, for answering all my questions immediately and for sending me on a research stay to the Simon Fraser University in Vancouver, BC, Canada.
- Markus Thiemann for your open way to share your major knowledge as well in aspects of physics, technical nature or even far beyond physics and university. Moreover thank you for your great willingness in answering all my questions, your eager support at any time and for the great and pleasant time at SFU and all around Vancouver . I've learned a lot from you!
- Gabriele Untereiner for preparing my samples and discussing a lot about crystallographic topics of copper.
- all my laboratory fellows Alessandro D'Arnese, Nikolaj Ebensperger, Vincent Engl, Carl Fürderer, Guilherme Gorgen Lesseux, Björn Miksch, Desirée Rausch, Markus Thiemann and Lars Wendel for making every single day pleasant and amusing.
- the whole institute for a nice and comfortable atmosphere.
- the low temperature shop for a really good cooperation and mutual support.
- the German Academic Exchange Service for giving me the opportunity to have a research stay at SFU in Vancouver, Canada.
- all people that provided me samples, i.e. the group of Prof. Dr. Jochen Mannhart of the Max Planck Institute of Solid State Research in Stuttgart, Germany, the company MaTecK in Jülich, Germany and Martin Jourdan and coworkers in the group of Prof. Adrian at the Johannes Gutenberg-Universität in Mainz, Germany.
- Maxi Haag for completely and Katharina Becher and Kai Klingler for partially proofreading this Master thesis.